UNIVERSITÀ POLITECNICA DELLE MARCHE

FACOLTÀ DI INGEGNERIA

Master's Degree in Biomedical Engineering

Curriculum: eHealth and Clinical Engineering

Brain Connectivity Analysis on Long-term Electroencephalograms in Pediatric Epileptic Patients with Intractable Seizures

Supervisor:

Dott. Ilaria Marcantoni

Candidate:

Alessia Di Brandimarte

Co-Supervisor:

Prof. Laura Burattini

Dott. Erica Iammarino

Academic Year 2025/2026

ABSTRACT

Epilepsy is one of the most common neurological disorders in children and is characterized by recurrent seizures resulting from abnormal neuronal activity. In particular, in patients with drug-resistant epilepsy, prolonged electroencephalographic (EEG) monitoring provides an important source of information for investigating the electrophysiological dynamics associated with seizure generation. In this context, quantitative EEG analysis, particularly the assessment of functional connectivity and brain network organization, may contribute to the identification of alterations occurring before seizure onset and to a better characterization of the preictal state.

The aim of this thesis was to investigate changes in functional brain connectivity and network organization preceding seizure onset in pediatric patients with drug-resistant epilepsy. Long-term scalp EEG recordings from the CHB-MIT database were analyzed. After preprocessing, EEG signals were divided into non-overlapping 4-s windows and classified according to their temporal relationship with seizures. The preictal state was defined as the 30 min preceding seizure onset, whereas interictal activity was required to occur at least 4 h from any seizure. Artifact-contaminated windows were identified using a Joint Probability approach and excluded from subsequent analyses.

Functional connectivity was characterized using 32 configurations, including broadband and frequency-specific measures based on linear correlation, information theory, phase synchronization, coherence, and amplitude coupling. A subset of 21 non-negative and undirected connectivity configurations was subsequently used to construct weighted functional networks and extract global and nodal graph-theoretical metrics. Preictal and interictal conditions were compared at the subject level using paired statistical analyses with correction for multiple comparisons. Finally, functional-connectivity and global graph-theoretical features were evaluated for preictal–interictal classification using both preliminary five-fold cross-validation and subject-independent leave-one-subject-out (LOSO) validation.

The functional-connectivity analysis did not identify any connections that remained statistically significant after False Discovery Rate correction, and no consistent temporal trend was observed across the 30-min preictal interval. Similarly, none of the global graph-theoretical metrics showed significant preictal–interictal differences after correction. In contrast, three nodal betweenness-centrality comparisons remained significant, indicating localized and frequency-dependent alterations in network organization. In the preliminary five-fold cross-validation, the best-performing functional-connectivity classifier was a Fine Gaussian SVM, achieving an accuracy of 84.0%, whereas a Fine KNN achieved 77.5% accuracy using global graph-theoretical features. However,

performance decreased under subject-independent LOSO validation. Functional-connectivity features achieved a balanced accuracy of 54.22% and a ROC-AUC of 0.533, whereas global graph-theoretical features achieved a balanced accuracy of 51.20% and a ROC-AUC of 0.512.

Taken together, these findings indicate that the preictal state in pediatric drug-resistant epilepsy was not associated with a homogeneous alteration in pairwise functional connectivity or global network organization across subjects. Instead, selected localized changes in network topology were identified, suggesting that preictal network dynamics may be spatially and frequency dependent. The limited subject-independent classification performance further highlights the marked inter-subject variability of pediatric epilepsy and supports the investigation of more individualized approaches for the characterization of preictal EEG dynamics.

Contents

1. Introduction 2

1.1 Overview of the Central Nervous System 2

1.1.1 Electrophysiological Basis of Neuronal Communication 2

1.1.2 Structural and Functional Organization of the Brain 6

1.2 Electroencephalography 8

1.2.1 Acquisition Modalities 9

1.2.2 Electroencephalographic Rhythms and Frequency Bands 13

1.2.3 Artifacts and Noise in Electroencephalographic Recordings 15

1.2.4 Electroencephalographic Signal Analysis and Feature Extraction 16

1.2.5 Electroencephalographic Characteristics in Pediatric Patients 18

1.3 Epilepsy: Neurophysiological and Clinical Aspects 21

1.3.1 Etiology of epilepsy and Seizure Triggers 22

1.3.2 Ictogenesis and Epileptogenesis 23

1.3.3 Seizure Semiology and Classification 24

1.3.4 Epilepsy in pediatric patients 25

1.3.5 Drug-Resistant Epilepsy 27

1.3.6 Diagnostic Evaluation of Epilepsy and the Role of Electroencephalography 27

1.3.7 Role of Prolonged Electroencephalographic Monitoring in Pediatric Patients 30

1.4 Brain Connectivity and Network Analysis 32

1.4.1 Functional Connectivity 33

1.4.2 Electroencephalographic Functional Connectivity Measures 34

1.4.3 Graph Theory in Brain Network Analysis 36

1.5 Long-term EEG Monitoring in Pediatric Drug-Resistant Epilepsy: Evidence from the Literature 38

Rationale of the Thesis 40

2. Materials and Methods 42

2.1 CHB-MIT Scalp Electroencephalographic Database Description 42

2.1.1 Population Description 42

2.1.2 Data Acquisition and Dataset Organization 43

2.2 Data Loading and Pre-processing 45

2.3 Functional Connectivity Feature Extraction 47

2.4 Graph-Theoretical Feature Extraction 53

2.5 Preictal versus Interictal Statistical Analysis 59

2.6 Classification Analysis 63

3. Results 67

3.1 Pre-processing Results 67

3.2 Functional Connectivity Results 70
3.2.1 Temporal evolution of functional connectivity during the preictal period 70
3.2.2 Preictal versus interictal functional connectivity statistics 75
3.3 Graph-Theoretical Results 83
3.3.1 Global Graph Metrics 83
3.3.2 Nodal Graph Metrics 85
3.4 Classification Results 88
3.4.1 Functional Connectivity-Based Classification 89
3.4.2 Graph-Theory-Based Classification 91
4. Discussion 94
Conclusion I
Appendix II
References V

1. Introduction

1.1 Overview of the Central Nervous System

The central nervous system (CNS), consisting of the brain and the spinal cord, is responsible for the processing and integration of neural information. While the spinal cord primarily provides communication between the brain and the rest of the body and contributes to reflex responses, the brain represents the main center for higher-order neural functions. Both structures are composed of nervous tissue, whose main cellular components are neurons and glial cells. Neurons receive, process, and transmit information through electrical and chemical signals, whereas glial cells provide structural and metabolic support and contribute to the maintenance of the neuronal environment [1].

Brain functions, including sensory processing, motor control, cognition, and behavior, depend on the coordinated activity of neurons, which communicate with each other and form highly interconnected networks distributed across different brain regions [1].

The following sections therefore describe the electrophysiological mechanisms underlying neuronal communication and the structural and functional organization of the brain.

1.1.1 Electrophysiological Basis of Neuronal Communication

Neurons are highly specialized excitable cells characterized by three fundamental physiological properties: excitability, conductivity, and secretion. Excitability refers to the ability to respond to external or internal stimuli by generating an electrical impulse; conductivity describes the capacity to propagate this impulse along the cell membrane; secretion involves the release of neurotransmitters, enabling communication with other neurons or target cells [1].

As illustrated in Figure 1, each neuron is composed of three main structural components: the cell body, the axon, and the dendrites. The cell body, or soma, contains the nucleus, where the genetic material (DNA) is stored, and is responsible for maintaining the metabolic functions of the neuron. The dendrites are branched extensions that serve as the primary input structures, receiving signals from other neurons and conveying them toward the cell body. In contrast, the axon is a single, elongated projection that acts as the output pathway, transmitting electrical signals away from the soma to other neurons, muscles, or glands. This structural organization allows neurons to efficiently integrate incoming information and generate appropriate responses within neural networks [1].

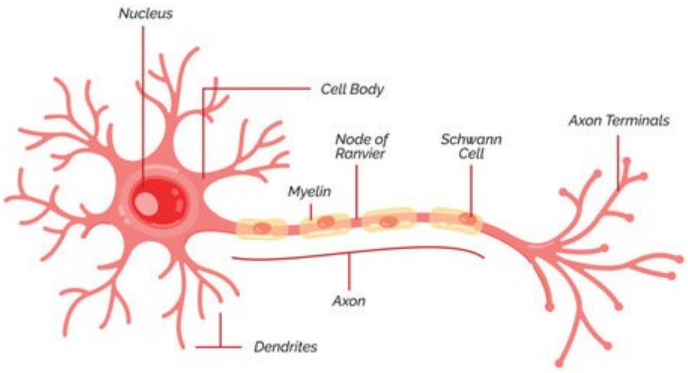


Figure 1. Structure of a neuron.

Neuronal communication is based on electrical activity generated by ionic movements across the cell membrane. The membrane, composed of a phospholipid bilayer with embedded proteins, acts as a selective barrier that separates the intracellular and extracellular environments while allowing controlled ion exchange. Due to its structure, it is largely impermeable to water-soluble substances, including ions, which can cross it only through specific transmembrane proteins such as ion channels and transporters [2]. Ion movement across the membrane occurs through both passive and active transport mechanisms. Passive transport includes diffusion processes driven by electrochemical gradients, resulting from differences in ion concentration and electrical charge across the membrane. These processes do not require cellular energy. In contrast, active transport requires metabolic energy, as ions are moved against their concentration gradient through specialized membrane proteins. A key example is the sodium–potassium pump, which continuously expels sodium ions (Na^+) from the cell while importing potassium ions (K^+) [2].

The electrochemical gradient determines the membrane potential, defined as the difference in electrical charge between the intracellular and extracellular compartments. At rest, the membrane potential typically ranges between −60 mV and −75 mV and reflects a dynamic equilibrium in which passive ionic currents are continuously balanced by active transport mechanisms. Notably, the maintenance of these ionic gradients requires significant metabolic energy, accounting for a substantial portion of total energy consumption [2]. In addition, the membrane exhibits capacitive properties, meaning it can store and separate electrical charges, which influences the temporal dynamics of voltage changes and contributes to the filtering of electrical signals along dendrites and axons [2].

When a neuron is stimulated, small changes in membrane potential, known as graded potentials, may occur. These potentials are variable in amplitude, can be either depolarizing or hyperpolarizing, and

typically decay with distance. If the depolarization reaches a critical threshold, voltage-gated ion channels are activated, generating an action potential, a self-propagating electrical signal along the axon [3]. Typically, an action potential lasts about 1–2 ms and has an amplitude of approximately 100 mV [3]. Once generated, it propagates along the axon through local currents that depolarize adjacent membrane regions in a cascade-like manner. This process follows an all-or-none principle: the action potential is either fully generated once the threshold is reached or not generated at all [2]. This electrical signal is characterized by sequential phases of depolarization, repolarization, and hyperpolarization, as can be seen in Figure 2. During depolarization, voltage-gated sodium channels open, allowing Na^+ ions to enter the cell and causing the membrane potential to become progressively more positive. This process continues until a peak value of approximately +30 mV is reached. Subsequently, sodium channels become inactivated, and voltage-gated potassium channels open, allowing K^+ ions to exit the cell. This leads to repolarization, during which the membrane potential returns toward negative values. Because potassium channels close slowly, a transient hyperpolarization phase occurs, in which the membrane potential becomes more negative than the resting value before stabilizing again [3].

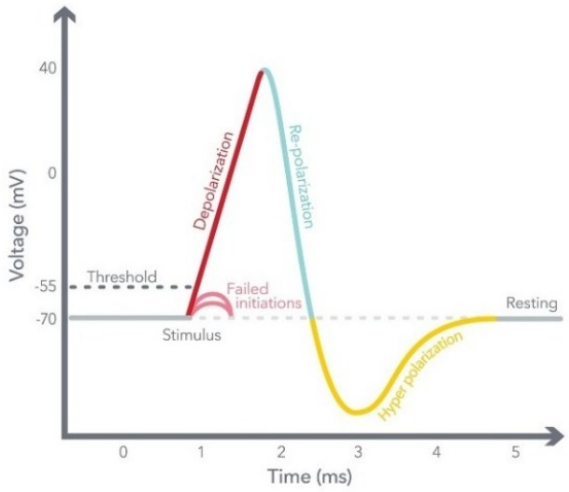


Figure 2. Action potential graph.

During these phases, the neuron enters refractory periods that regulate signal propagation. In the absolute refractory period, sodium channels are inactivated and cannot reopen, preventing the generation of a new action potential regardless of stimulus strength. This ensures unidirectional propagation of the signal. In the subsequent relative refractory period, a stronger-than-normal stimulus is required to initiate another action potential due to the ongoing hyperpolarization of the membrane [3]. Axonal conduction may occur continuously in unmyelinated fibers or through saltatory conduction in myelinated fibers. In myelinated fibers, the myelin sheath electrically

insulates the axon, preventing ion exchange along covered segments, while voltage-gated ion channels are concentrated at the nodes of Ranvier. As a result, the action potential appears to "jump" from node to node, significantly increasing conduction velocity and energy efficiency [3].

Following the propagation of the action potential along the axon, neuronal communication continues at specialized junctions known as synapses, where a neuron establishes a functional connection with another neuron or, in some cases, with non-neuronal cells such as muscle or epithelial cells. At the synaptic level, the neural signal is transmitted from a presynaptic neuron to a postsynaptic neuron. Depending on the site of contact, synapses can involve connections between the axon and the dendrite, the soma, or another axon of the postsynaptic neuron. This structural diversity reflects different functional roles in the modulation and integration of neural signals [3]. Synaptic transmission can occur through two principal mechanisms: electrical and chemical synapses. Electrical synapses, mediated by gap junctions, permit direct ionic flow between adjacent cells, ensuring rapid and sometimes bidirectional communication, though with less capacity for signal integration. Chemical synapses (Figure 3) are the most widespread and allow complex modulation, integration, and plasticity of neural signals, although they involve a slight delay due to neurotransmitter release and receptor activation.

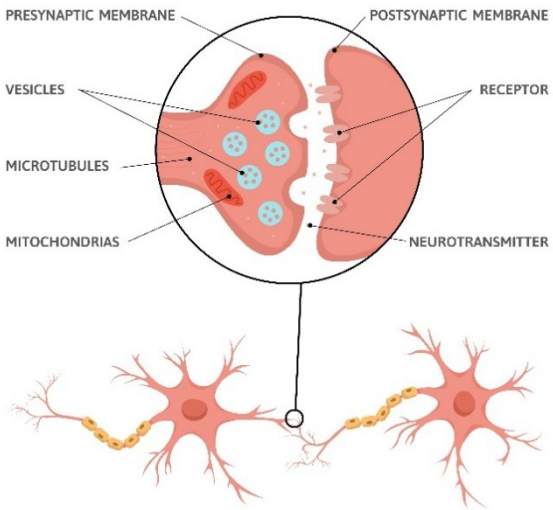


Figure 3. Chemical synapses.

The presynaptic terminal contains synaptic vesicles filled with neurotransmitters, which are released into the synaptic cleft following the arrival of an action potential. These molecules then diffuse across the cleft and bind to specific receptors located on the postsynaptic membrane, leading to a change in the electrical state of the receiving neuron. Neurotransmitters can exert either excitatory or inhibitory

effects on the postsynaptic cell, producing changes in membrane potential known as postsynaptic potentials. These can be classified as excitatory postsynaptic potentials (EPSPs), which increase the likelihood of generating an action potential, or inhibitory postsynaptic potentials (IPSPs), which decrease neuronal excitability and the likelihood of action potential generation.

1.1.2 Structural and Functional Organization of the Brain

The brain represents the most complex structure of the central nervous system. Located inside the skull, in an adult human it weighs approximately 1.3–1.4 kg [4] and contains about 86 billion neurons [1]. From a structural point of view, the brain is organized into gray and white matter. Gray matter consists primarily of neuronal cell bodies, dendrites, and synapses and forms the cerebral cortex as well as deeper nuclei; white matter, in contrast, is composed predominantly of myelinated axons that connect different cortical areas and subcortical structures, enabling communication between distant regions of the brain.

From a broader anatomical perspective, the brain can be described in terms of three major developmental regions: the forebrain, the midbrain, and the hindbrain. The forebrain is the source of intellectual activities and comprises the cerebrum, thalamus, and hypothalamus. The cerebrum constitutes the largest portion of the brain and is composed of two cerebral hemispheres (right and left), separated by the longitudinal fissure and interconnected by a major commissural fiber bundle known as the corpus callosum. The cerebrum has a superficial layer, called the cerebral cortex, which is pure gray matter, and a deeper component, called the subcortical component which includes both gray matter structures and white matter structures. Moreover, the cerebral cortex is convoluted resulting in gyri (elevations) and sulci (grooves), to enable more cerebral cortex matter to fit inside the skull [1]. The cerebrum is anatomically and functionally subdivided into four major lobes (as shown in Figure 4): frontal, parietal, occipital, and temporal. Each one is associated with specific, although partially overlapping, functions [5]. The frontal lobe, which is separated from the parietal lobe by a groove called the central sulcus, is primarily responsible for voluntary motor control, as well as higher-order cognitive processes such as planning, decision-making, and executive functions. Posterior to the central sulcus lies the parietal lobe, which includes the primary somatosensory cortex and is involved in the conscious perception and integration of sensory information, including touch, pressure, pain, and temperature. The occipital lobe, situated at the posterior part of the brain, is mainly dedicated to visual processing, receiving and interpreting visual stimuli. The temporal lobe, located inferior to the lateral sulcus, plays a key role in auditory and olfactory processing and is also involved in memory and language functions.

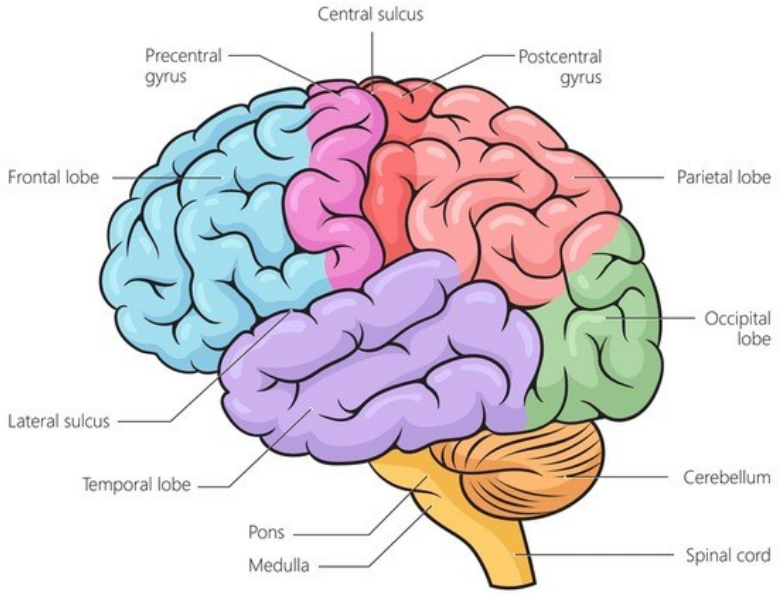


Figure 4. Sagittal section of the brain.

The thalamus, through connections with different areas of the cerebral cortex, is involved in the functioning of all sensory systems, except olfaction. It also plays a fundamental role in voluntary movements, in the regulation of the sleep-wake cycle, in the state of consciousness, in emotions and in some aspects of memory capacity. The hypothalamus is the anatomical element of connection between the nervous system and the endocrine system. It takes part in the regulation of body temperature or the sense of satiety, and in the release of hormones. The hypothalamus is connected to the reticular formation of the brainstem and to the amygdala, a paired nuclear complex, located medially within the temporal lobes which has a fundamental role in decision-making, processing of memory and emotional responses. The hindbrain includes the cerebellum, pons, and medulla oblongata. The cerebellum, located posteriorly and inferiorly to the cerebrum, plays a key role in coordination, balance, and fine motor control. Despite representing a smaller proportion of total brain volume, it contains a substantial number of neurons and contributes significantly to motor integration. The pons act as a bridge between different brain regions, facilitating communication between the cerebrum, cerebellum, and spinal cord. The medulla oblongata, which represents the most caudal portion of the brainstem, regulates vital autonomic functions such as respiration, heart rate, and blood pressure, and contains centers responsible for basic reflexes including swallowing, coughing, and vomiting. The midbrain controls some reflex actions and is part of the circuit involved in the control of eye movements and other voluntary movements. Specifically, the midbrain is composed of the superior and inferior colliculi. The superior colliculi play an important role in the visual pathway, while the inferior colliculi are important in the auditory pathway.

The brain is enveloped by three protective connective tissue membranes known as the meninges: the dura mater, arachnoid mater, and pia mater. The dura mater is the outermost and most robust layer; the arachnoid mater forms a delicate intermediate membrane; and the pia mater closely adheres to the surface of the brain, following its contours and sulci. Between the arachnoid and pia mater lies the subarachnoid space, which contains major cerebral blood vessels and cerebrospinal fluid (CSF). Cerebrospinal fluid is a clear fluid that provides mechanical protection, metabolic support, and the removal of waste products. It is primarily produced by the choroid plexuses within the ventricles, a system of interconnected cavities located inside the brain, including the two lateral ventricles, the third ventricle, and the fourth ventricle. From the ventricles, the fluid circulates into the subarachnoid space, thereby surrounding the central nervous system and contributing to the maintenance of its internal homeostasis [1].

1.2 Electroencephalography

Electroencephalography (EEG) is an electrophysiological technique that enables the direct recording of the brain's electrical activity by measuring the potential generated by neuronal populations, without relying on intermediate physiological processes [6]. EEG can be performed using either invasive or non-invasive approaches. Invasive EEG, known as electrocorticography (ECoG), involves the placement of electrodes directly on the cortical surface, allowing for high spatial resolution recordings. In contrast, non-invasive EEG is obtained through the positioning of electrodes on the scalp, providing a safer and more widely applicable method for monitoring brain activity. In this work, the focus will be on non-invasive scalp electroencephalography, as it represents the most widely used technique in both clinical and research settings.

Electroencephalographic signals consist of low-amplitude voltage fluctuations, generally ranging between 10 μV and 100 μV [6]. These signals arise primarily from the summation of excitatory postsynaptic potentials and inhibitory postsynaptic potentials generated by synchronized neuronal populations [7]. These neurons are characterized by a specific spatial organization: their cell bodies are aligned in parallel and oriented perpendicular to the cortical surface, a configuration that facilitates the generation of measurable electrical fields. Pyramidal cells are the most numerous in the cortex and have a conic shaped soma, a single axon, a large atypical dendrite, multiple basal dendrites and dendritic spines [2]. The electrical activities associated with pyramidal cells are action potentials and post-synaptic potentials. Although action potentials represent the fundamental mechanism of neuronal communication, they have a very short duration and occur asynchronously across neurons.

In addition, axons are typically oriented in different directions, leading to cancellation of the associated electrical fields. Consequently, their contribution to the scalp-recorded EEG signal is negligible. In contrast, postsynaptic potentials have a longer duration, ranging from tens to hundreds of milliseconds, allowing temporal and spatial summation across large populations of neurons. For this reason, the electrical fields detected by EEG originate from the postsynaptic activity of cortical pyramidal neurons. During an EPSP, the influx of positive ions (mainly Na^+) into the dendrites creates a localized extracellular negativity at the site of synaptic activation (current sink) and a corresponding positivity in adjacent regions (current source) due to return currents. Conversely, during an IPSP, the influx of Cl^- ions or the efflux of K^+ ions produces an opposite pattern, with extracellular positivity at the synapse and compensatory negativity in surrounding regions. Excitatory inputs are predominantly located in the distal regions of the dendrites, while inhibitory inputs are typically found closer to the cell body. This spatial separation between excitation and inhibition leads to the formation of electrical dipoles, which constitute the fundamental generators of the EEG signal.

1.2.1 Acquisition Modalities

When large populations of pyramidal neurons are synchronously activated, the individual dipoles summarize to produce a macroscopic electrical field that can be detected by scalp electrodes. Electrodes are conductive sensors applied to the skin using an electrolytic paste that ensures stable electrical contact. They are usually made by silver/silver chloride or gold, chosen for their low polarization and stability properties. Electrodes can be individually attached with wires or embedded within caps or nets, particularly in high-density EEG systems [8]. It has been estimated that the synchronous activity of thousands of neurons within a cortical area of several square centimeters is required to generate a measurable signal at the scalp [7]. When electrical activity generated by cortical neurons reaches the electrode–skin interface, an ionic exchange occurs between the tissue and the electrode through the conductive paste, resulting in the generation of an electrode potential (Figure 5). This potential depends on both the current and the impedance of the electrode–skin interface, according to the following relationship:

$$V = I \cdot Z$$

where V is the measured potential, I is the current flowing through the interface, and Z is the impedance, which accounts for the combined effects of resistance and capacitance. The orientation of the cortical sources plays a crucial role in determining the distribution of electrical potentials on

the scalp, indeed, sources located on the convexity of the cortex generate radial dipoles, producing surface potentials that are more easily detectable, while sources located within cortical sulci generate tangential dipoles, whose associated electrical fields propagate differently and may be less directly represented on the scalp. After their generation at the cortical level, EEG signals propagate through several non-neural layers, including the meninges, skull, and scalp. These tissues behave as volume conductors, causing attenuation and spatial smoothing of the signals before they reach the recording electrodes. As a result, scalp EEG predominantly reflects the activity of superficial cortical neurons, whereas deeper brain structures contribute only indirectly through their influence on cortical dynamics.

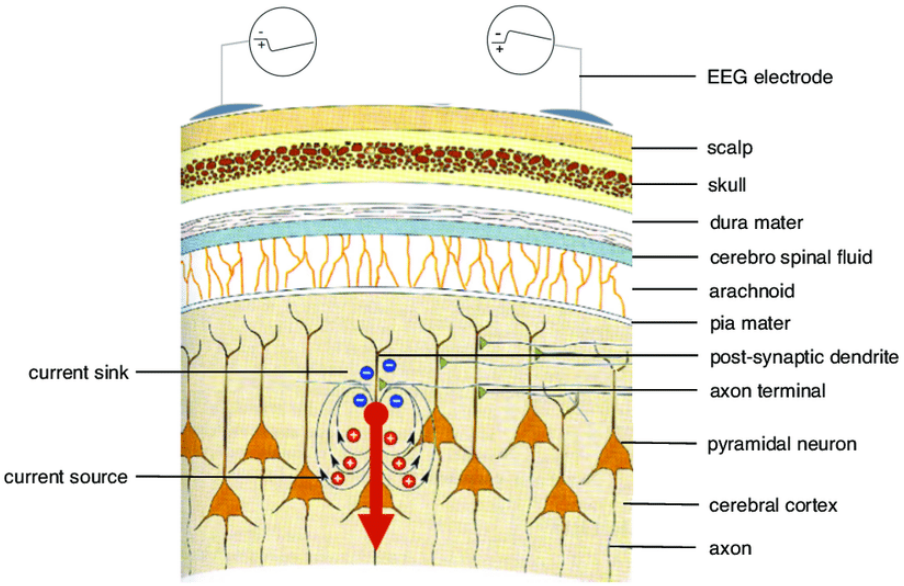


Figure 5. How the electrical signal travels to the scalp electrodes [9].

Each electrode is labeled according to the underlying brain region, providing a spatial framework for interpreting EEG signals: prefrontal (Fp), frontal (F), central (C), parietal (P), temporal (T), and occipital (O). In addition, electrode numbering reflects hemispheric lateralization (left or right hemisphere), with odd numbers indicating the left hemisphere and even numbers the right hemisphere. The letter "Z" denotes electrodes located along the midline sagittal plane. Lower numbers correspond to positions closer to the midline, while higher numbers indicate more lateral locations. In clinical practice, scalp electrodes are positioned according to standardized systems defined by the International Federation of Clinical Neurophysiology (IFCN), the most widely used being the international 10–20 system (Figure 6). The system is based on proportional measurements between anatomical landmarks of the head, including the nasion, the inion, and the preauricular

points. The terms "10" and "20" indicate that the distances between adjacent electrodes correspond to 10% or 20% of the total length of these reference lines, ensuring consistent and reproducible electrode placement across subjects [10].

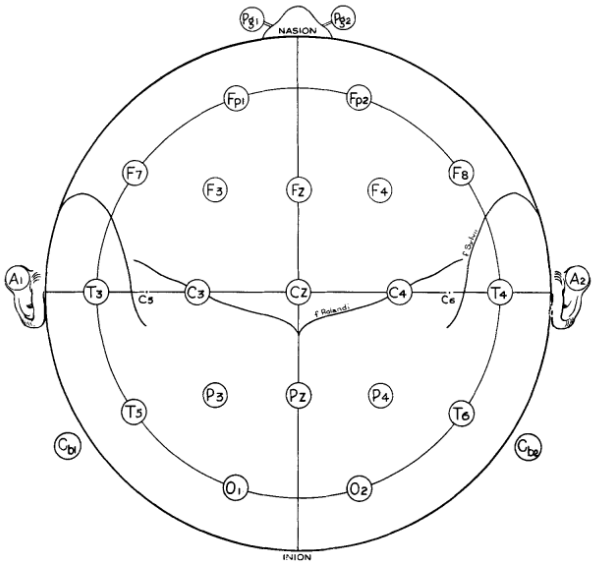


Figure 6. International 10-20 system [10].

However, this system has some limitations in terms of spatial coverage. In particular, the standard 10–20 system does not include electrodes in some strategically relevant regions, such as portions of the inferior temporal chain, and therefore activity originating from or propagating through these areas may be insufficiently sampled. To improve spatial resolution, extensions of the standard 10–20 system have been developed: the 10–10 system (Figure 7) introduces additional electrodes placed at intermediate positions, effectively reducing the spacing between electrodes to approximately 10% of the reference distances. Even higher-density configurations, such as the 5% system, further increase the number of recording sites. Higher electrode density enhances the spatial sampling of EEG signals and improves the accuracy of source localization, particularly when combined with mathematical modeling techniques. However, increased density also requires longer setup times and greater technical complexity. In addition to recording electrodes, EEG systems include one or more ground electrodes, which are connected to the acquisition system to stabilize the electrical circuit and reduce environmental noise. The position of the ground electrode is typically defined by the recording system manufacturer.

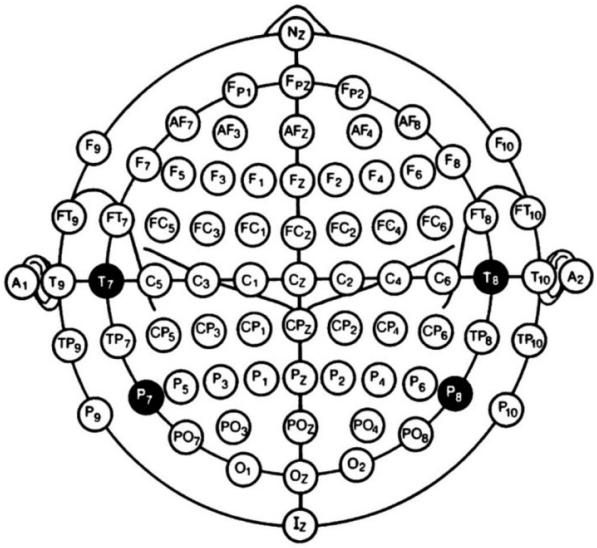


Figure 7. Modified combinatorial nomenclature for the 10-10 system [11].

The recorded waveforms also depend on the way electrical potentials are referenced and combined between electrodes. These recording configurations are known as EEG montages and play a crucial role in signal visualization and clinical interpretation. There are two broad categories: bipolar and referential configurations. In bipolar recordings, the difference between pairs of neighboring electrodes is recorded and series of linked derivations form chains. A standard configuration in this category is the double banana bipolar montage, which includes right and left temporal chains, right and left parasagittal chains, and a central chain. Other bipolar configurations include circumferential bipolar montage, in which linked derivations encircle the head, and transverse bipolar montage, in which the chains run from left to right rather than in the sagittal direction. These alternative montages can be useful in specific situations or combined when interpretation based on a single configuration is not sufficiently clear. In the referential montage instead, the potential recorded at each electrode is compared with a single common reference. The reference may be a physically relatively silent site, such as the auricle of the ear, or a computed value such as the average potential of all electrodes. Referential montages provide a different representation of the same underlying brain activity and are often complementary to bipolar recordings [8].

From the clinical point of view, EEG can be performed using different monitoring modalities depending on the diagnostic objective. Routine EEG monitoring is the standard short-duration recording, usually lasting approximately 20 to 40 minutes, and is mainly used to evaluate whether the brain's electrical activity shows abnormalities suggestive of pathology. However, because of its

limited duration, routine EEG may fail to capture intermittent or infrequent events. To overcome this limitation, ambulatory EEG monitoring allows prolonged recordings in the patient's home environment, typically for 24, 48, or 72 hours. This modality increases the probability of capturing abnormal events during daily activities and sleep. Modern systems may also include simultaneous video recording, giving rise to ambulatory video-EEG monitoring, in which the association between clinical semiology and electrophysiological changes can help distinguish cerebral from extracerebral events. In more complex cases, inpatient video-EEG monitoring is performed in the hospital under medical supervision, generally for three to five days or even longer. This modality is particularly useful when close observation is required or when medications must be reduced or withdrawn under controlled conditions.

In addition to the recording modality and electrode configuration, EEG acquisition is defined by technical parameters such as the sampling frequency and the number of recording channels. The sampling frequency determines the temporal resolution of the signal and should be sufficiently high to capture the frequency components of interest according to the Nyquist criterion. Clinical EEG systems commonly employ sampling frequencies of at least 128 Hz, whereas values of 256 Hz or higher provide improved temporal characterization and are frequently adopted in both clinical practice and research. The number of recording channels determines the spatial coverage of the scalp, with a higher number of electrodes generally providing better spatial resolution and source localization.

1.2.2 Electroencephalographic Rhythms and Frequency Bands

EEG signals are commonly described in terms of their rhythmic activity, which reflects the oscillatory behavior of neuronal populations over time. These oscillations arise from the synchronized activity of large groups of neurons and can be characterized by their frequency, amplitude, and spatial distribution across the scalp. In particular, the frequency of the signal corresponds to the rate at which the electrical potential fluctuates between positive and negative values. EEG activity is commonly characterized in terms of distinct frequency bands, each associated with specific physiological and functional states. Although the exact boundaries between these bands are not rigid and may vary slightly across studies, a standardized classification is widely used in both clinical and research settings. Accordingly, EEG rhythms are typically categorized into delta, theta, alpha, beta, and gamma bands, as illustrated in the following figure [12].

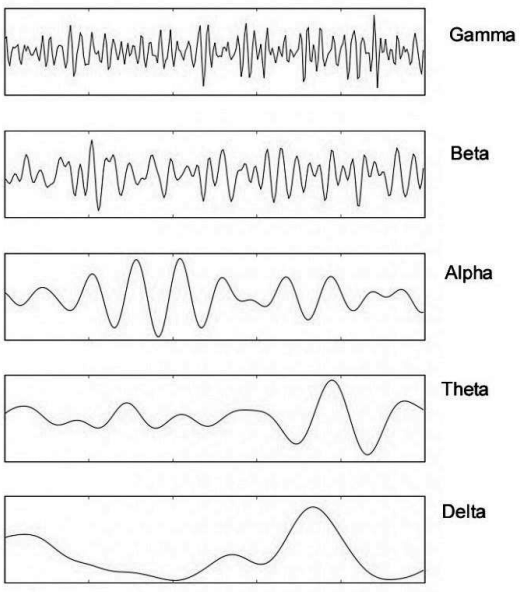


Figure 8. Comparison of EEG Frequency Bands [12].

Delta activity, defined as frequencies between 0.5 Hz and 4 Hz, represent the lowest frequency band and consists of slow, high-amplitude waves. It is typically observed during deep sleep in adults and in normal brain activity in infants. However, its presence in awake adults may indicate pathological conditions such as diffuse brain lesions or metabolic encephalopathies. Theta activity, ranging from 4 to 7 Hz, is commonly seen in children and during drowsiness or early stages of sleep in adults. Although it can be associated with normal physiological states such as relaxation or meditation, excessive theta activity in adults may indicate abnormal brain function. In pediatric populations, theta activity can be more prominent and may represent a normal developmental pattern. However, excessive or persistent theta activity in awake adults may be indicative of neurological abnormalities. Alpha waves, in the range of 8 to 12 Hz, are among the most prominent rhythms in EEG recordings and represent the dominant rhythm in relaxed, awake individuals, particularly with closed eyes. It is most prominent in the posterior regions particularly in the occipital lobe and tends to attenuate with eye opening or mental effort. This phenomenon, known as “alpha blocking” or “desynchronization,” reflects changes in cortical activation. First described by Hans Berger, this rhythm is associated with a state of cortical “idling”, reflecting reduced task-related activity, and is thought to contribute to inhibitory control mechanisms across different brain regions [13]. Beta activity, ranging from approximately 13 to 30 Hz, is typically associated with active thinking, alertness, and motor activity. It is most prominent in frontal regions and is often enhanced during states of concentration or anxiety. These waves are characterized by lower amplitude and higher frequency compared to alpha waves.

The last group of frequencies regards gamma oscillations (>30 Hz) [14]. They are thought to be related to higher-order cognitive functions, including perception, attention, and memory processing, but are more difficult to detect with standard scalp EEG due to their low amplitude and susceptibility to noise [13]. From a physiological perspective, EEG rhythms reflect the balance between excitatory and inhibitory synaptic activity within neuronal networks. The degree of synchronization among neurons plays a crucial role: highly synchronized activity tends to produce slower, higher-amplitude waves, whereas desynchronized activity results in faster, lower-amplitude oscillations. It is important to note that EEG rhythms are not static but dynamically change over time, depending on the behavioral and physiological state of the subject. Transitions between different states, such as wakefulness and sleep, are characterized by corresponding changes in the dominant frequency components of the EEG signal. This dynamic nature makes EEG a powerful tool for monitoring brain function in both physiological and pathological conditions. In clinical practice, the analysis of EEG rhythms plays a fundamental role in the identification of abnormal patterns, particularly in neurological disorders. Alterations in frequency content, the presence of atypical rhythms, or abnormal synchronization patterns can provide important diagnostic information and guide further investigation. The distribution and characteristics of these rhythms vary depending on age, brain region, and physiological or pathological conditions [14].

1.2.3 Artifacts and Noise in Electroencephalographic Recordings

An artifact is defined as any signal component that does not originate from cerebral activity. Since the EEG signals are in the microvolt range, they are particularly vulnerable to disturbances that may significantly affect data interpretation. These disturbances can arise from both technical issues and physiological sources. EEG recordings are susceptible to various sources of noise and artifacts, some of which may not be uniformly distributed across electrodes and can therefore persist in the recorded signals. For this reason, the identification and correct interpretation of artifacts are essential to avoid misdiagnosis and ensure reliable clinical evaluation [15]. Among physiological artifacts (Figure 9), ocular activity represents one of the most significant sources of EEG contamination. Eye movements generate changes in the electric field around the eyes, which propagate to the scalp and distort the recorded signal. The electrooculogram (EOG), which measures voltage changes near the eyes, is commonly used to detect and correct ocular artifacts in EEG recordings. Muscle activity is another major source of artifact, arising from contractions of different muscle groups. These artifacts typically affect multiple electrodes simultaneously and exhibit a broad frequency spectrum that overlaps with standard EEG frequency bands, particularly in the range of 20–300 Hz. This overlap makes them

especially problematic, as they can contaminate higher-frequency EEG components and affect analyses such as sleep studies or epilepsy monitoring [16]. Cardiac activity can also introduce artifacts into EEG recordings through electrocardiographic (ECG) signals. These artifacts can be identified and removed using an ECG reference signal, improving the overall quality of the EEG data [15].

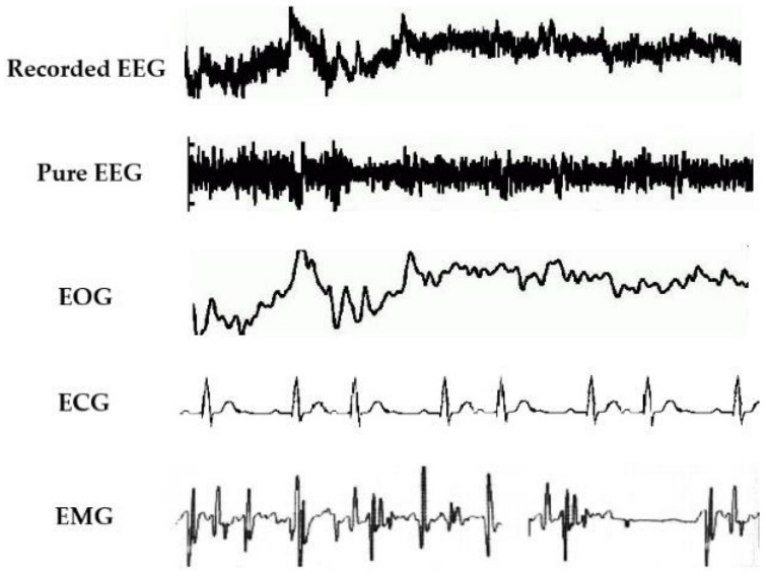


Figure 9. Physiological artifacts present in EEG signals [15].

Non-physiological artifacts arise from external sources, such as electrode impedance issues, poor electrode contact, movement of cables, and electrical interference from the surrounding environment, including power line noise. The impedance depends on the electrical resistance of the skin and the quality of contact between the electrode and the electrolytic paste. Excessively high impedance may introduce noise and artifacts, whereas excessively low impedance may distort the signal. For this reason, proper skin preparation is essential before electrode placement. Cleaning the skin and removing oils or debris helps reduce impedance and ensures a stable and reliable recording but also maintaining good electrode–skin contact throughout the acquisition is equally important.

1.2.4 Electroencephalographic Signal Analysis and Feature Extraction

Electroencephalographic signals are inherently complex, non-stationary, and characterized by a low signal-to-noise ratio, which makes their analysis particularly challenging. For this reason, advanced signal processing techniques are required to extract meaningful information from raw recordings and the EEG analysis pipeline consists of several sequential steps [9].

Preprocessing is a crucial stage that aims to improve signal quality by attenuating noise and artifacts. Artifact removal strategies generally include prevention, rejection, and cancellation techniques, all aiming to eliminate noise without compromising the integrity of the neural signal. Traditional approaches often rely on filtering methods, such as notch filters, to suppress specific frequency components. However, these techniques are limited when artifact frequencies overlap with those of genuine EEG activity. More advanced methods include regression-based techniques and blind source separation (BSS) approaches, such as principal component analysis (PCA) and independent component analysis (ICA), which have proven effective in isolating and removing physiological artifacts. More recent developments have also introduced adaptive and wavelet-based approaches for artifact detection and correction, further improving EEG signal quality in both clinical and research applications [16]. Once the signal has been adequately preprocessed, feature extraction is performed. This process transforms the EEG signal into a set of quantitative descriptors that capture its most relevant characteristics while reducing data dimensionality and preserving essential information for subsequent analysis. EEG features can be broadly categorized according to the domain in which they are extracted [17]. In the time domain, descriptors are computed directly from the signal waveform and include statistical measures such as mean, variance, skewness, and kurtosis, as well as parameters such as Hjorth descriptors, zero-crossing rate, and waveform length. These measures are computationally efficient and are especially useful for detecting transient events, such as epileptiform discharges [17]. In the frequency domain, spectral analysis techniques are used to decompose the signal into its constituent frequency components. Methods such as the Fast Fourier Transform (FFT) and Power Spectral Density (PSD) estimation allow the evaluation of how signal energy is distributed across the standard EEG frequency bands. Spectral descriptors, including band power and spectral entropy, are widely used because of their robustness and physiological interpretability [9]. Given the non-stationary nature of EEG recordings, time–frequency analysis methods are often employed to simultaneously characterize temporal and spectral variations. Techniques such as the Short-Time Fourier Transform (STFT) and the wavelet transform describe how the frequency content evolves over time, making them well suited for analyzing transient phenomena such as epileptic spikes and seizures. Wavelet-based methods, in particular, have demonstrated excellent performance in seizure detection thanks to their ability to capture localized changes in the signal [9]. In addition to temporal and spectral information, spatial features can be extracted from multichannel EEG recordings to exploit the spatial distribution of brain activity. Techniques such as Common Spatial Patterns (CSP) enhance discriminative spatial information by maximizing differences between brain states and improving the signal-to-noise ratio [18]. EEG signals also exhibit nonlinear and complex dynamics that cannot be fully characterized by conventional linear methods. For this reason, nonlinear

descriptors have been introduced to quantify signal complexity and irregularity. Among these, entropy-based measures have attracted considerable attention because they provide quantitative information about the degree of complexity, regularity, and unpredictability of EEG activity. While spectral entropy evaluates the distribution of power across the frequency spectrum, sample entropy quantifies the temporal irregularity of the signal. Together, these measures provide complementary information to conventional spectral descriptors and contribute to a more comprehensive characterization of brain activity. Such features have proven particularly effective in distinguishing pathological from normal brain activity [18]. When quantitative EEG features are used to objectively characterize physiological or pathological brain states, they are commonly referred to as EEG biomarkers. More recently, deep learning approaches have been introduced to automatically learn discriminative features directly from raw EEG recordings. Models such as convolutional neural networks (CNNs) and recurrent neural networks (RNNs) can capture complex spatial and temporal patterns without requiring handcrafted feature extraction, demonstrating promising performance in several EEG analysis tasks [18].

1.2.5 Electroencephalographic Characteristics in Pediatric Patients

In pediatric populations, electroencephalographic activity is strongly influenced by brain maturation, making EEG interpretation more complex than in adults. Normal EEG patterns vary significantly with age and developmental stage, reflecting the progressive organization of neuronal networks and synaptic activity. As a result, features that may appear abnormal in adults can represent physiological findings in children, depending on age and state of consciousness. In early life, EEG activity is often discontinuous and less organized, while with maturation it becomes increasingly continuous, structured, and characterized by well-defined background rhythms and sleep patterns [35]. These developmental changes, together with increased susceptibility to movement and artifacts during recording, require careful acquisition and age-specific interpretation of pediatric EEG.

Neonatal EEG requires careful interpretation within the appropriate clinical context, taking into account the infant's conceptional age, behavioral state, and any ongoing pharmacological treatments. Among these factors, conceptional age, defined as the sum of gestational age at birth and postnatal age, plays a fundamental role because the normal characteristics of the EEG change considerably throughout brain maturation. Unlike the EEG of older children and adults, neonatal EEG is characterized by age-dependent background activity that evolves progressively with neurological development. In preterm infants, the background is physiologically discontinuous and consists of

alternating periods of high-amplitude electrical activity, referred to as bursts, and periods of low-amplitude activity known as interburst intervals (IBIs). As conceptional age increases, the interburst intervals gradually shorten and the EEG becomes progressively more continuous.

This maturational process is reflected by three characteristic background patterns. Tracé discontinu is the typical pattern observed in preterm infants and is characterized by prominent discontinuity with prolonged interburst intervals. As brain maturation progresses, the EEG evolves into tracé alternant, a transitional physiological pattern that is typically observed during quiet sleep in healthy term neonates. Tracé alternant is characterized by a regular alternation between periods of relatively high-voltage activity and periods of lower-voltage activity while maintaining continuous cerebral electrical activity without complete suppression. With further maturation, the background develops into tracé continu, in which the electrical activity becomes predominantly continuous with little or no discontinuity. Therefore, the progression from tracé discontinu to tracé alternant and finally to tracé continu represents the normal maturation of neonatal brain activity and is closely related to conceptional age. An example of tracé alternant recorded during quiet sleep in a healthy term neonate is shown in Figure 11.

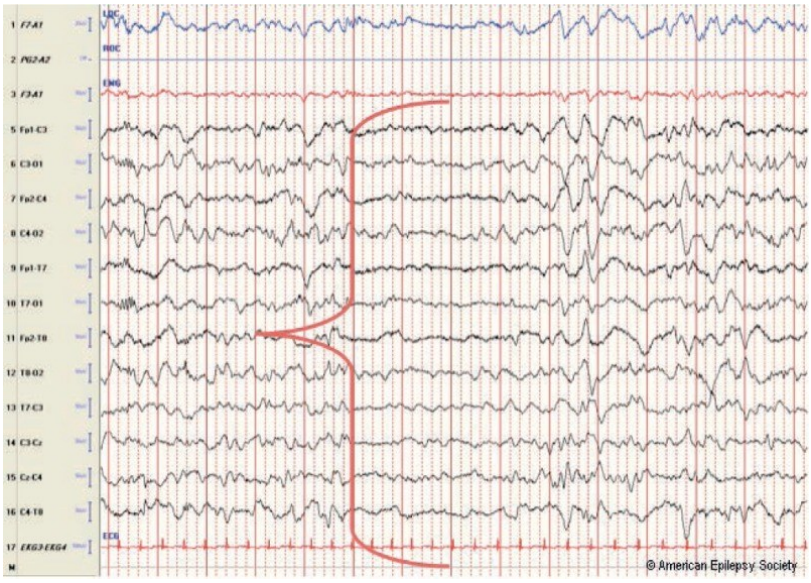


Figure 11. Example of tracé alternant in a neonatal EEG recording during quiet sleep, illustrating discontinuous background activity typical of early brain maturation [35].

EEG background organization in neonates is assessed through several key parameters, including continuity, symmetry, synchrony, amplitude, and reactivity. Continuity increases with maturation, while synchrony evolves from highly synchronous patterns in early preterm stages to more differentiated interhemispheric activity before reaching mature synchronization at term age. Reactivity to external stimuli, absent in very premature infants, progressively develops with brain maturation and represents an important indicator of neurological integrity. Behavioral state also plays a crucial role in neonatal EEG interpretation, as distinct EEG patterns are observed during wakefulness, active sleep, and quiet sleep, with sleep architecture becoming more organized with increasing age. Active sleep is characterized by irregular respiration and eye movements, whereas quiet sleep shows more stable EEG patterns, including characteristic alternating activity. Technical considerations are particularly important in neonatal EEG, with modified electrode montages used to ensure adequate coverage of central and temporal regions, where most neonatal EEG activity is concentrated. An example of electrode placement adapted for neonatal EEG recording is shown in Figure 12.

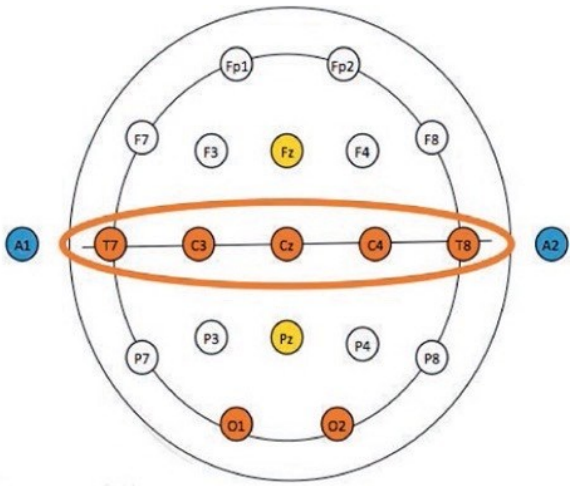


Figure 12. Electrode placement according to the modified 10–20 system for neonatal EEG recordings [35].

Neonatal EEG is also highly susceptible to artifacts arising from environmental factors, medical equipment, or patient handling, which may mimic physiological or pathological EEG patterns and must therefore be carefully recognized during signal interpretation. Beyond the neonatal period, EEG continues to evolve throughout infancy and childhood: during the first year of life, the posterior dominant rhythm (PDR) emerges and progressively increases in frequency, reaching approximately 8 Hz by 3 years of age, while sleep features such as spindles, K-complexes, and V-waves gradually develop and become more organized over time. Throughout childhood and adolescence, EEG patterns

continue to mature, with increasing background frequency, improved organization, and the appearance of age-specific physiological patterns. These developmental changes highlight the importance of age-specific interpretation of EEG findings in pediatric patients, as failure to consider normal maturational patterns may lead to misinterpretation of physiological features as pathological abnormalities [35].

Therefore, a thorough understanding of EEG development is essential for the accurate interpretation of electroencephalographic recordings in pediatric patients. Electroencephalographic recordings in pediatric patients also present specific technical and methodological challenges compared to adult EEG. Children, particularly younger ones, are more prone to movement during recordings, making careful electrode application and continuous monitoring of electrode impedance essential to ensure adequate signal quality. Standard electrode placement generally follows the International 10–20 system, although adaptations may be required in neonates or when full electrode application is not feasible. The recording of different physiological states is especially important in pediatric populations. EEG acquisition should include wakefulness, drowsiness, and sleep whenever possible, as transitions between these states may reveal patterns not evident in a single condition.

1.3 Epilepsy: Neurophysiological and Clinical Aspects

Epilepsy is a chronic neurological disorder characterized by a predisposition to generate recurrent, unprovoked seizures. A seizure is defined as a transient occurrence of signs and/or symptoms due to abnormal, excessive, or synchronous neuronal activity in the brain, which may lead to a wide range of clinical manifestations, from brief lapses of awareness to prolonged convulsions [19]. Epilepsy represents one of the most common neurological disorders worldwide [20], affecting individuals of all ages. The risk of seizure recurrence after a first unprovoked event is significant, with approximately 40% of individuals experiencing a second seizure within two years [21]. The global burden of epilepsy is disproportionately higher in low-income countries, likely due to increased exposure to risk factors and limited access to adequate healthcare [22]. According to the International League Against Epilepsy (ILAE), a diagnosis of epilepsy can be made when any one of the following criteria is met [19]:

1. At least two unprovoked seizures occurring more than 24 hours apart.
2. One unprovoked seizure and a probability of further seizures similar to the general recurrence risk (at least 60%) after two unprovoked seizures, occurring over the next 10 years.

3. Diagnosis of an epilepsy syndrome.

The ILAE also introduced the concept of resolved epilepsy, which applies to individuals who are past the typical age range for an age-dependent syndrome, or who have remained seizure-free for at least 10 years, including the last 5 years without antiseizure medication [19].

In the following sections, the neurophysiological mechanisms underlying epilepsy, the main seizure types, and the clinical role of EEG in epilepsy will be discussed.

1.3.1 Etiology of epilepsy and Seizure Triggers

The ILAE classifies the causes of epilepsy into six broad categories: structural, genetic, infectious, metabolic, immune, and unknown. These categories are not mutually exclusive, and more than one may apply in an individual case [23]. Structural causes of epilepsy refer to abnormalities in the anatomy of the brain that increase the risk of seizures. These may be acquired from stroke, traumatic brain injury, brain tumor, or central nervous system infection, or developmental and genetic in origin, as seen in conditions like focal cortical dysplasia or certain congenital brain malformations. Genetic causes of epilepsy are those in which a person's genes directly contribute to the development of seizures. This includes cases where a specific mutation has been identified, as well as situations where the family history and clinical features strongly suggest a genetic basis, even if no known mutation is found. Genetic factors are believed to contribute to many cases of epilepsy, either directly or by increasing vulnerability to other causes. Some forms are caused by a single gene defect, but most are due to a combination of multiple genes and environmental influences [24]. Infectious etiologies include central nervous system infections that directly involve brain tissue and may result in persistent seizure susceptibility. Notable examples are herpes simplex encephalitis, which is associated with a high risk of subsequent epilepsy, and neurocysticercosis, a leading preventable cause of epilepsy in endemic regions [25]. Immune causes include conditions like autoimmune encephalitis, in which the immune system attacks brain tissue, often presenting with seizures. Certain autoimmune epilepsies are associated with specific autoantibodies, including those against the NMDA receptor, LGI1, and CASPR2. These cases often present rapid-onset, difficult-to-treat seizures [23]. Metabolic causes of epilepsy include metabolic disorders that disrupt the brain's normal function. In rare cases, epilepsy may result from inborn errors of metabolism, such as mitochondrial diseases, urea cycle disorders, or glucose transporter type 1 (GLUT1) deficiency. These often present early in life and may be associated with developmental delays, movement disorders, or other neurological symptoms [23].

Seizures may also occur in the context of transient metabolic disturbances, such as hypoglycemia, hyponatremia, or hypocalcemia. However, these events are classified as acute symptomatic seizures and do not represent epilepsy, as they are triggered by a temporary underlying condition rather than a chronic predisposition [26]. Unknown causes of epilepsy refer to cases where no clear structural, genetic, infectious, immune, or metabolic origin can be identified despite thorough evaluation. A substantial proportion of epilepsy cases still fall into this group, particularly in regions with limited access to advanced testing [23]. This category acknowledges the limits of current diagnostic techniques and scientific understanding.

While the etiology of epilepsy explains the underlying causes of the disorder, seizure occurrence is often influenced by additional factors that can trigger epileptic events. Seizures are not entirely random and may be precipitated by conditions such as stress, sleep deprivation, excessive alcohol consumption, or exposure to flickering light. The concept of seizure threshold is used to describe the level of neuronal excitability required for a seizure to occur, which is typically reduced in individuals with epilepsy [27].

1.3.2 Ictogenesis and Epileptogenesis

The pathophysiology of epilepsy can be conceptualized through two distinct but closely related processes: ictogenesis, which is the mechanisms responsible for the generation of individual seizures, and epileptogenesis, which describes the long-term process through which the brain acquires a persistent predisposition to generate spontaneous seizures [28].

The process of ictogenesis begins with a disruption of the balance between excitatory and inhibitory mechanisms that regulate neuronal network activity. In the healthy brain, neuronal communication occurs through electrical activity that is typically asynchronous and tightly regulated. From a neurophysiological perspective, epilepsy arises from a disruption of the balance between excitatory and inhibitory mechanisms that control neuronal network activity. Under physiological conditions, excitatory neurotransmission is primarily mediated by glutamate, which induces depolarization of the postsynaptic membrane, whereas inhibitory neurotransmission is mainly mediated by gamma-aminobutyric acid (GABA), which reduces neuronal excitability through hyperpolarization [5]. In epileptic conditions, this balance is altered, resulting in a state of neuronal hyperexcitability and hypersynchronization that facilitates the generation of abnormal electrical discharges across neuronal networks. At the cellular level, epileptic activity is characterized by paroxysmal depolarization shifts, consisting of prolonged depolarizations followed by bursts of action potentials, reflecting an

increased tendency of neurons to fire repetitively [29]. At the network level, the synchronization of neuronal populations involves both local circuits and long-range connections between cortical and subcortical regions, promoting the emergence and spread of epileptic discharges. Neuronal excitability is further modulated by intracellular factors, including ion channel expression, receptor function, and gene regulation, as well as extracellular factors such as ionic concentrations, synaptic plasticity, and glial regulation of neurotransmitter clearance [30].

While ictogenesis explains the mechanisms underlying individual seizures, epileptogenesis refers to the long-term process through which the brain acquires a persistent predisposition to generate spontaneous seizures. This process may follow various brain insults, including traumatic brain injury, stroke, central nervous system infections, brain tumors, or prolonged seizures, although in many cases no clear cause can be identified. Epileptogenesis involves a complex cascade of biological changes, among which are neuronal loss, synaptic reorganization, gliosis, neuroinflammation, and disruption of the blood–brain barrier, ultimately leading to the formation of hyperexcitable and abnormally synchronized neural networks centered around a seizure focus [28].

1.3.3 Seizure Semiology and Classification

The clinical manifestations of seizures, collectively referred to as seizure semiology, vary depending on the brain regions involved and the type of seizure. Seizures may affect multiple functional domains, including motor, sensory, autonomic, and cognitive or emotional processes. Motor manifestations include muscle stiffening, rhythmic jerking, myoclonic movements, or loss of muscle tone, while sensory symptoms may involve paresthesias, visual phenomena, or auditory hallucinations. Autonomic alterations can affect functions such as heart rate, respiration, or gastrointestinal activity, and cognitive or emotional symptoms may include confusion, fear, or altered perception. Seizures can therefore present with a wide spectrum of clinical features, ranging from subtle alterations in awareness to generalized convulsions with loss of consciousness.

Seizures can be provoked or unprovoked. Provoked seizures occur in response to identifiable causes, such as fever, trauma, or metabolic disturbances, whereas unprovoked seizures occur in the absence of an immediate precipitating factor. The occurrence of recurrent unprovoked seizures defines epilepsy [19].

According to the International League Against Epilepsy, seizures are classified into four main categories: focal, generalized, unknown onset, and unclassified seizures. Focal seizures originate within a network limited to one hemisphere of the brain and may arise from cortical or subcortical

structures. For a given seizure type, seizures usually begin in the same region, although the abnormal activity may subsequently spread to adjacent areas or to the contralateral hemisphere. Focal seizures are further classified based on the level of awareness and responsiveness during the event into focal aware seizures, focal impaired awareness seizures, and focal-to-bilateral tonic–clonic seizures. Generalized seizures originate within, and rapidly engage, bilaterally distributed networks involving both hemispheres from onset [31]. They are broadly classified into absence seizures, characterized by brief lapses of awareness, and generalized tonic–clonic seizures, which involve an initial tonic phase followed by clonic movements, along with other less common generalized seizure types. When insufficient information is available to determine the onset, seizures are classified as unknown. In cases where a seizure is clearly epileptic but cannot be assigned to a specific category, it is designated as unclassified, typically as a temporary label pending further evaluation. In addition to seizure classification, epilepsy itself can be categorized into focal epilepsy, generalized epilepsy, combined generalized and focal epilepsy, and unknown epilepsy. This distinction is clinically relevant, as it guides treatment strategies, prognosis, and interpretation of electroencephalographic findings [23].

1.3.4 Epilepsy in pediatric patients

Epilepsy is one of the most common neurological disorders in the pediatric population, with an estimated incidence ranging from 40 to 100 cases per 100,000 children per year. The incidence is highest during the first year of life, reflecting the increased susceptibility of the developing brain to epileptogenic processes [35]. The etiology of pediatric epilepsy is highly heterogeneous and varies according to age. In infants and young children, epilepsy is frequently associated with genetic disorders, congenital brain malformations, metabolic diseases, and perinatal brain injuries. In older children, structural lesions, infections, and genetic epilepsy syndromes become more prominent causes [35]. This etiological diversity contributes to the wide variability of clinical presentations observed in pediatric patients. The clinical manifestations of seizures in children often differ from those observed in adults. Seizures may present with subtle or atypical features, including behavioral arrest, automatisms, staring episodes, or brief motor phenomena, which can complicate recognition and diagnosis. Furthermore, several epilepsy syndromes are age-dependent and occur predominantly during childhood, such as childhood absence epilepsy and self-limited epilepsy with centrotemporal spikes (SeLECTS), formerly known as benign epilepsy with centrotemporal spikes [36]. Compared with adult epilepsy, pediatric epilepsy is strongly influenced by the ongoing processes of brain maturation. As a result, epilepsy in children exhibits distinct clinical, etiological, and prognostic

characteristics. In addition to seizure occurrence, epilepsy may significantly affect neurodevelopment, cognition, behavior, and psychosocial functioning. Frequent seizures, underlying neurological abnormalities, and prolonged epileptic activity can interfere with normal brain development, potentially leading to learning difficulties, cognitive impairment, and behavioral disturbances [35]. The diagnosis of pediatric epilepsy requires the integration of clinical history, neurological examination, electroencephalography, and, when indicated, neuroimaging studies. Differential diagnosis is particularly important in children, as several physiological and non-epileptic conditions may mimic epileptic seizures. Common pediatric epilepsy syndromes include self limited epilepsy with centrotemporal spikes, childhood absence epilepsy, West syndrome, Lennox Gastaut syndrome, and Dravet syndrome, each presenting distinct clinical and electroencephalographic characteristics. In contrast, febrile seizures, although representing the most common seizure disorder in childhood, are not classified as epilepsy because they occur in association with fever and do not result from an enduring predisposition to generate unprovoked seizures. Nevertheless, complex febrile seizures may be associated with a slightly increased risk of developing epilepsy later in life. Among the neurological emergencies encountered in pediatric epilepsy, status epilepticus is one of the most severe conditions. According to the International League Against Epilepsy, it is defined as prolonged seizure activity or recurrent seizures without complete recovery of consciousness between episodes, requiring prompt medical intervention to minimize the risk of permanent neuronal injury and long term neurological sequelae. In children, status epilepticus may occur in association with acute symptomatic conditions, such as central nervous system infections or metabolic disturbances, as well as in patients with an established diagnosis of epilepsy. The clinical outcome of pediatric epilepsy is highly variable and depends on several factors, including the underlying etiology, epilepsy syndrome, seizure type, age at onset, and response to antiseizure medication. Many children, particularly those with self limited epilepsy syndromes and no significant structural or developmental abnormalities, achieve long term seizure remission and may eventually discontinue treatment. Conversely, children with developmental and epileptic encephalopathies or drug resistant epilepsy frequently experience persistent seizures accompanied by cognitive, behavioral, and developmental impairments that significantly affect quality of life. Although mortality in pediatric epilepsy remains relatively low, it is higher than in the general pediatric population, particularly among children with severe neurological disorders. Sudden unexpected death in epilepsy (SUDEP), although rare in childhood, represents the most important cause of epilepsy related mortality and should be considered in the long term management of affected patients.

1.3.5 Drug-Resistant Epilepsy

The management of epilepsy is based on a range of therapeutic strategies, including antiseizure medications, surgical interventions, neuromodulation techniques, and dietary approaches, aimed at achieving seizure control and improving quality of life. Antiseizure medications represent the first-line treatment for epilepsy and are effective in achieving seizure control in the majority of patients. However, a significant proportion of individuals continue to experience seizures despite appropriate pharmacological therapy. Drug-resistant epilepsy, also referred to as intractable epilepsy, represents one of the most difficult conditions in clinical neurology, as it is characterized by the persistence of seizures despite appropriate pharmacological treatment. Although the majority of patients achieve seizure control with antiseizure medications, a significant proportion continues to experience recurrent seizures even after multiple therapeutic attempts. According to the International League Against Epilepsy, drug-resistant epilepsy is defined as the failure to achieve sustained seizure freedom after adequate trials of two appropriately chosen and tolerated antiseizure medications, whether used as monotherapy or in combination. This definition emphasizes the importance of both treatment adequacy and accurate seizure classification in determining true pharmacoresistance. The refractory nature of epilepsy may be associated with underlying structural, genetic, or metabolic etiologies. However, apparent treatment resistance may also result from misdiagnosis, incorrect classification of seizure type, or inappropriate selection of antiseizure medication, highlighting the need for accurate diagnostic evaluation. Drug-resistant epilepsy has significant clinical implications, as persistent seizures can negatively affect cognitive function, behavior, and overall quality of life. The likelihood of achieving seizure control decreases with each unsuccessful treatment, making early identification of pharmacoresistance crucial. In such cases, referral to specialized epilepsy centers is recommended, where a multidisciplinary approach can be adopted. Alternative therapeutic strategies may include epilepsy surgery, neuromodulation techniques such as vagus nerve stimulation, and dietary therapies such as the ketogenic diet [37].

1.3.6 Diagnostic Evaluation of Epilepsy and the Role of Electroencephalography

The diagnostic evaluation of epilepsy begins with confirming whether the reported event was in fact a seizure. The initial assessment aims to distinguish epileptic seizures from common mimics such as syncope, psychogenic non-epileptic seizures, or transient ischemic attacks [27]. Following clinical evaluation, selected investigations are performed to exclude acute causes and conditions that may mimic epileptic seizures. A 12-lead electrocardiogram is recommended in all individuals presenting with a first seizure to identify potential cardiac arrhythmias or other cardiovascular disorders that may

resemble epilepsy. Laboratory tests may also be conducted to detect metabolic disturbances, including hypoglycemia, electrolyte imbalances, or renal and hepatic dysfunction, particularly in acute settings.

Once an epileptic seizure is suspected, further diagnostic evaluation aims both to support the diagnosis and identify its underlying cause. Electroencephalography plays a central role in this process, as it provides information on abnormal electrical activity, supports seizure classification, and may help identify specific epilepsy syndromes. EEG findings are commonly classified into interictal and ictal activity, depending on whether the recording is obtained between seizures or during a seizure. Interictal activity includes epileptiform discharges such as spikes, sharp waves, and spike-and-wave complexes, whereas ictal activity consists of rhythmic and evolving EEG patterns reflecting the onset and propagation of abnormal neuronal discharges [31]. These complementary findings contribute to the identification, localization, and classification of epileptic disorders.

EEG activity can also be investigated during the pre-ictal period, the interval immediately preceding seizure onset, during which gradual changes in neuronal dynamics may occur. Although no universally accepted temporal definition exists, the identification of pre-ictal EEG alterations has attracted considerable interest because it may provide insights into seizure generation mechanisms and support the identification of biomarkers associated with seizure onset. Most seizures last less than two minutes and are followed by a postictal phase characterized by confusion, fatigue, or other neurological symptoms, whereas seizures lasting longer than five minutes, or occurring without complete recovery between episodes, are classified as status epilepticus, a neurological emergency associated with significant morbidity and mortality.

In parallel, neuroimaging is performed to identify potential structural abnormalities underlying epilepsy. The main structural neuroimaging techniques used in this context are magnetic resonance imaging (MRI) and computed tomography (CT). MRI is generally preferred because of its superior sensitivity in detecting lesions such as cortical malformations, tumors, or hippocampal sclerosis, whereas CT may be used when MRI is unavailable or contraindicated. EEG and neuroimaging therefore provide complementary information and are often both required for a comprehensive diagnostic assessment [32].

From an electroencephalographic perspective, interictal epileptiform discharges (IEDs) represent one of the most important EEG biomarkers of epilepsy. These transient waveforms reflect the hypersynchronous firing of neuronal populations and include spikes, sharp waves, and spike-and-

wave complexes. Although they are highly specific for epilepsy when present, they may not be observed in every patient. An example of a typical spike-and-wave pattern is shown in Figure 10.

Video-EEG monitoring is considered the gold standard for differentiating epileptic seizures from non-epileptic events because it enables simultaneous recording of clinical behavior and brain electrical activity, allowing accurate electroclinical correlation [31]. However, the diagnostic yield of routine EEG remains limited, with a sensitivity ranging from 29% to 55% for detecting interictal epileptiform discharges [33]. Consequently, a normal routine EEG does not exclude epilepsy. When routine EEG findings are inconclusive and clinical suspicion remains high, further investigations such as sleep-deprived EEG, ambulatory EEG, or prolonged recordings in an epilepsy monitoring unit (EMU) may be required. Activation procedures, including hyperventilation, photic stimulation, and sleep deprivation, can further increase the likelihood of detecting epileptiform abnormalities [33].

EEG also plays an important role in the follow-up and management of epilepsy, particularly during the presurgical evaluation of focal epilepsy, where it contributes to the localization of the epileptogenic zone and supports clinical decision-making. Nevertheless, EEG findings should always be interpreted in conjunction with the patient's clinical history and other diagnostic investigations.

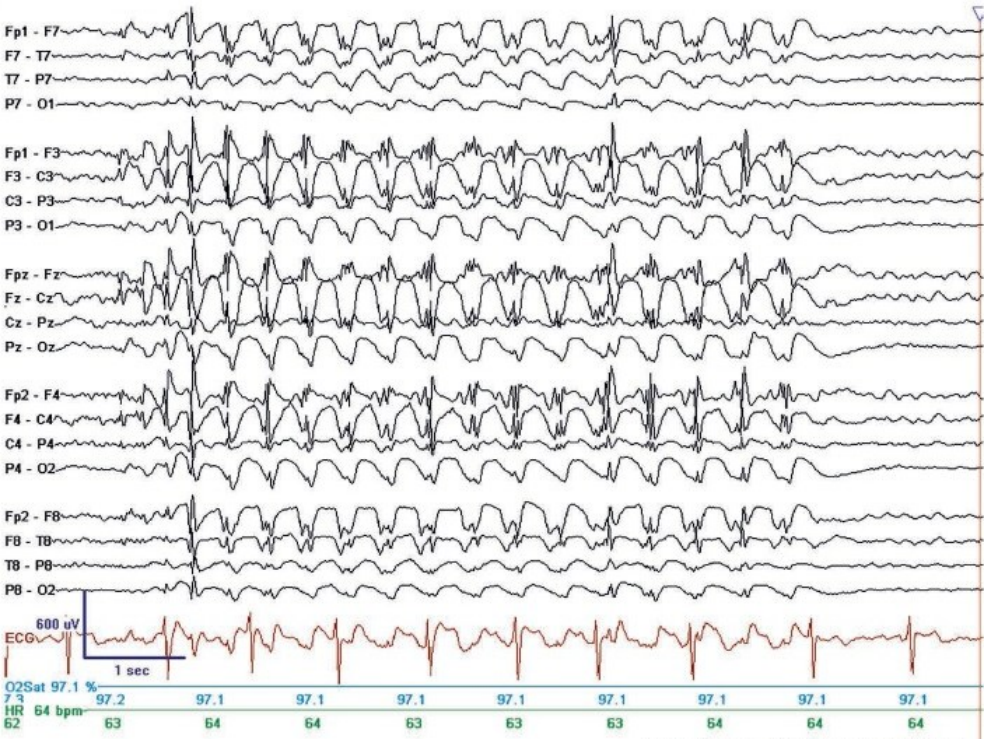


Figure 10. Example of a 3-Hz generalized spike-and-wave interictal epileptiform discharge (IED), typically observed in childhood absence epilepsy (CAE) [35].

1.3.7 Role of Prolonged Electroencephalographic Monitoring in Pediatric Patients

Routine electroencephalographic recordings have limited sensitivity, as interictal epileptiform abnormalities may not be present during a short recording session. This limitation is particularly relevant in pediatric epilepsy, where seizures may be infrequent, occur predominantly during sleep, or present with subtle clinical manifestations. Consequently, a single routine recording may fail to capture epileptiform activity, reducing its diagnostic yield [27]. To overcome these limitations, prolonged electroencephalographic monitoring is frequently employed in pediatric patients. By extending the recording duration from several hours to 24 hours or longer, prolonged electroencephalographic monitoring increases the likelihood of capturing both ictal events and transient interictal abnormalities. Continuous monitoring also provides a more comprehensive representation of brain activity across different physiological states, including wakefulness, drowsiness, and sleep, thereby improving diagnostic accuracy [38]. Long-term monitoring is particularly valuable when routine recordings are inconclusive or when clinical events remain difficult to classify. Common indications include suspected epilepsy with normal standard electroencephalographic findings, unclassified seizure types, and paroxysmal events of uncertain origin requiring differentiation between epileptic and non-epileptic phenomena. In addition, prolonged monitoring contributes to the identification and characterization of epilepsy syndromes, especially in early-onset epilepsies where clinical manifestations may be subtle or atypical. A major advantage of prolonged electroencephalographic monitoring is the possibility of establishing electroclinical correlations. This capability is greatly enhanced when electroencephalography is combined with synchronized video recording. Long-term video-electroencephalographic monitoring allows simultaneous observation of the patient's behavior and brain electrical activity, making it possible to correlate clinical manifestations with specific electroencephalographic changes. For this reason, video-electroencephalographic monitoring is considered the gold standard for differentiating epileptic seizures from non-epileptic events and for accurately classifying seizure types [31].

Prolonged electroencephalographic monitoring also plays a crucial role in the management of drug-resistant epilepsy. In these patients, long-term video-electroencephalographic monitoring is an essential component of the pre-surgical evaluation process. Continuous recording enables the capture of multiple seizure events and facilitates detailed analysis of seizure onset and propagation patterns. The resulting electroclinical information is used to localize the seizure onset zone and to formulate

hypotheses regarding the epileptogenic region, thereby supporting surgical planning and patient selection [36].

The duration of long-term electroencephalographic monitoring depends largely on the frequency of seizures or paroxysmal events. In many cases, recordings lasting approximately 24 hours are sufficient, whereas longer monitoring periods may be required when events occur infrequently. Night-time recordings are particularly important because sleep promotes the occurrence of epileptiform activity and may reveal abnormalities not observed during wakefulness. From a technical perspective, prolonged electroencephalographic monitoring in children requires adaptation to the pediatric setting. Recordings are commonly performed in specialized units with continuous supervision by trained personnel. Parents or caregivers are often involved in monitoring the child and reporting clinical events. Electrode placement must be secure and adapted to the patient's age to ensure signal quality throughout the recording period, frequently requiring reinforced fixation methods. Long-term monitoring may also incorporate additional physiological signals, including electrocardiography, electromyography, respiratory monitoring, and electrooculography. Together with synchronized video recording, these modalities provide a multimodal assessment that improves interpretation and reduces the risk of misclassifying physiological or behavioral events as epileptic phenomena. In selected cases, prolonged electroencephalographic monitoring can also be performed in ambulatory settings, allowing recordings to be acquired in the patient's home environment. Although ambulatory monitoring may not provide continuous supervision and may lack synchronized video recording, it remains a useful alternative for capturing infrequent events and sleep-related abnormalities under more natural conditions.

Despite its significant clinical value, the interpretation of prolonged electroencephalographic recordings requires careful consideration of the patient's age, developmental stage, and clinical context. Electroclinical correlations may be particularly challenging in pediatric populations due to the evolving nature of brain networks and the wide variability of seizure manifestations. Nevertheless, prolonged electroencephalographic monitoring remains one of the most valuable tools for the diagnosis, classification, and follow-up of pediatric epilepsy. Furthermore, it enables objective assessment of treatment response by providing accurate information on seizure occurrence and electrographic activity, an important advantage when clinical reporting is incomplete or unreliable [37].

1.4 Brain Connectivity and Network Analysis

Beyond the identification of epileptiform abnormalities, EEG recordings provide the opportunity to investigate how neuronal activity is coordinated across different brain regions and how these interactions evolve over time. This aspect is particularly relevant in epilepsy, where seizure generation and propagation involve alterations in the interactions among distributed neuronal populations. Therefore, the quantitative analysis of relationships among EEG signals can provide complementary information to the analysis of individual channels and conventional EEG patterns. Within this context, brain connectivity and network analysis provide a framework for characterizing the organization of neuronal interactions and their alterations associated with epileptic activity.

The human brain operates as a complex network in which anatomically distributed regions continuously exchange information to support both physiological and cognitive functions. Brain connectivity is commonly classified into structural, functional, and effective connectivity. Structural connectivity refers to the anatomical pathways linking different brain regions, functional connectivity describes the statistical relationships between spatially separated neuronal activities, whereas effective connectivity characterizes the directed influence that one brain region exerts on another [39]. Rather than functioning as isolated structures, cortical and subcortical areas communicate through dynamic interactions that continuously change according to behavioral state, cognitive processes, and neurological condition. This network-oriented perspective has shifted the study of brain function from the investigation of individual brain regions toward the analysis of interactions within distributed neural networks. Consequently, many neurological disorders, including epilepsy, are increasingly investigated from a network perspective [40].

Within this framework, electroencephalography represents a particularly suitable technique for investigating brain connectivity because of its excellent temporal resolution. Although its spatial resolution is lower than that of other neuroimaging techniques, such as functional magnetic resonance imaging, EEG enables the investigation of neuronal interactions occurring on the millisecond timescale, making it particularly suitable for studying highly dynamic brain processes such as epileptic activity. Furthermore, EEG is non-invasive, relatively inexpensive, and widely available in clinical practice. Unlike conventional visual EEG inspection, which primarily focuses on waveform morphology and epileptiform abnormalities, quantitative connectivity analysis characterizes interactions between different EEG signals by measuring their synchronization or statistical dependence. These quantitative approaches enable the investigation of large-scale brain organization and provide reproducible measures that complement traditional visual EEG analysis [39].

This network perspective has become increasingly important for understanding seizure generation, seizure propagation, and the organization of epileptogenic networks. Functional connectivity analysis can be further extended through graph theory, which represents the brain as a mathematical network composed of nodes and edges, allowing local and global topological properties of brain organization to be quantitatively characterized. Network measures derived from graph theory provide complementary information to pairwise connectivity analyses by describing how information is integrated and segregated across the entire brain network [42]. Together, functional connectivity analysis and graph-theoretical methods provide complementary approaches for investigating brain network organization in both physiological and pathological conditions, including epilepsy [41].

1.4.1 Functional Connectivity

Functional connectivity (FC) refers to the statistical dependence between the activity recorded from different brain regions, reflecting the degree to which neuronal populations exhibit coordinated temporal dynamics. Unlike structural connectivity, which describes the anatomical white-matter pathways connecting different brain regions, functional connectivity quantifies the temporal relationships between signals without requiring direct anatomical connections. Consequently, it provides information about the functional integration of distributed brain regions during both physiological and pathological brain activity. A distinction should also be made between functional connectivity and effective connectivity. While functional connectivity measures statistical associations or synchronization between signals, effective connectivity attempts to determine the direction and causal influence that one brain region exerts on another. Because functional connectivity does not assume causal interactions, it can be estimated using a wide variety of statistical and signal-processing techniques, making it one of the most widely adopted approaches for studying large-scale brain networks [39].

FC analysis can be performed in both the time and frequency domains using linear or nonlinear measures, depending on the characteristics of the neuronal interactions under investigation. Furthermore, connectivity can be estimated either as a static property over an entire recording segment or as dynamic functional connectivity (dFC), which characterizes temporal fluctuations in network organization through the analysis of consecutive or overlapping time windows [40].

This dynamic approach is particularly relevant for EEG analysis because brain connectivity continuously evolves over time, reflecting changes in cognitive state, physiological conditions, or neurological disorders. In epilepsy, abnormal neuronal synchronization represents one of the

principal neurophysiological mechanisms underlying seizure generation and propagation. Consequently, functional connectivity has become an important quantitative approach for investigating alterations in brain networks during interictal, pre-ictal, ictal, and post-ictal periods. Rather than identifying only the seizure onset zone, connectivity analysis allows the characterization of the broader epileptic network, which may involve multiple distributed cortical and subcortical regions. This network-based perspective has contributed to the growing recognition of epilepsy as a disorder involving large-scale functional brain networks rather than a purely focal pathology [40].

The availability of long-term EEG recordings has further expanded the potential of connectivity analysis by enabling the investigation of temporal variations in network organization before, during, and after epileptic events. Long-duration recordings also provide the opportunity to evaluate the stability and evolution of functional interactions across different physiological states, including wakefulness and sleep, thereby offering a more comprehensive characterization of epileptic brain dynamics [39].

1.4.2 Electroencephalographic Functional Connectivity Measures

Several quantitative measures have been proposed to estimate functional connectivity from EEG recordings. Although all aim to describe the statistical relationship between pairs of EEG signals, each measure captures different aspects of neuronal interactions and relies on different mathematical principles [39]. Because neuronal communication is a complex phenomenon involving multiple temporal and spectral characteristics, no single connectivity measure is able to completely describe all aspects of functional interactions within the brain [40]. Connectivity measures can be broadly classified according to the type of dependency they evaluate. They may quantify linear or nonlinear relationships, phase synchronization, shared information, or directed interactions, and can be computed in either the time or frequency domain. Furthermore, some measures estimate undirected statistical associations, whereas others infer the direction of information flow between brain regions [41]. Consequently, the choice of a specific metric depends on the physiological phenomenon under investigation, the characteristics of the EEG recordings, and the scientific question being addressed [39].

Among the most widely used measures are Pearson correlation, cosine similarity, cross-correlation, and the Linear Cross-Correlation Coefficient (LCCC), which quantify the similarity between pairs of EEG signals in the time domain. Pearson correlation evaluates linear dependence between signals, cosine similarity measures the similarity of their waveform orientation independently of signal

magnitude, whereas cross-correlation and LCCC additionally account for possible temporal delays between signals. In the frequency domain, coherence estimates the consistency of oscillatory activity at specific frequencies and is widely employed to characterize frequency-specific synchronization. Although these methods are computationally efficient and extensively used, they are sensitive to volume conduction, the passive spread of electrical activity through the tissues of the head, which can cause the same neural source to be detected by multiple scalp electrodes, as well as to common reference effects. These factors may lead to an overestimation of functional interactions [43]. Phase-based measures provide an alternative approach for assessing synchronization between EEG signals. The Phase Locking Value (PLV) quantifies the consistency of phase differences between EEG signals over time; however, it remains sensitive to zero-lag synchronization that may arise from volume conduction. In contrast, the Phase Lag Index (PLI) and the Weighted Phase Lag Index (wPLI) reduce the contribution of zero-lag interactions and are therefore less sensitive to the effects of volume conduction and field spread [43]. Consequently, PLI and especially wPLI are generally considered more robust estimators of genuine functional interactions in scalp EEG recordings [43]. Connectivity can also be assessed through information-theoretic and nonlinear approaches. Mutual Information (MI) quantifies the amount of information shared between two EEG signals and is capable of detecting both linear and nonlinear statistical dependencies. Similarly, the Nonlinear Correlation Coefficient (H^2) estimates nonlinear relationships that cannot be captured by conventional linear measures. Another complementary approach is the Amplitude Envelope Correlation (AEC), which evaluates the correlation between the amplitude envelopes of band-pass filtered EEG signals and is particularly useful for characterizing slow fluctuations in oscillatory activity across different brain regions [41]. Multivariate approaches attempt to identify direct interactions while reducing the influence of indirect connections. The Sparse Precision Matrix estimates the inverse covariance matrix under sparsity constraints, allowing the identification of direct statistical relationships between EEG channels. Partial Correlation, derived from the precision matrix, further quantifies the direct linear association between two signals after removing the influence of all remaining channels in the network [41]. Finally, directed connectivity methods aim to estimate the direction of information flow within functional brain networks. In this context, Temporal Granger Causality (GC) evaluates whether the past activity of one EEG signal improves the prediction of another signal beyond its own history. Partial Directed Coherence (PDC) extends this concept to the frequency domain using multivariate autoregressive modeling, whereas the Adaptive Directed Transfer Function (ADTF) allows the estimation of time-varying directed interactions in non-stationary EEG recordings, making it particularly suitable for studying the temporal evolution of brain networks [39].

Since each connectivity measure is sensitive to different characteristics of the EEG signal and may be affected differently by factors such as noise, signal non-stationarity, reference selection, and volume conduction, no single metric can be considered universally optimal. Instead, each technique presents specific advantages and limitations that should be carefully considered according to the experimental design and the neurophysiological processes under investigation [40]. For this reason, several studies recommend combining complementary connectivity measures to obtain a more comprehensive characterization of functional brain networks rather than relying on a single estimator [41]. Recent studies have demonstrated the usefulness of these measures for identifying epileptogenic networks, characterizing seizure propagation, evaluating treatment response, predicting surgical outcome, and investigating alterations in functional brain organization associated with epilepsy. Nevertheless, considerable heterogeneity remains regarding the selection of connectivity metrics, preprocessing strategies, frequency bands, and network construction methods. This methodological variability is particularly evident in pediatric drug-resistant epilepsy, where relatively few studies have systematically compared multiple connectivity measures under standardized analysis protocols [40].

1.4.3 Graph Theory in Brain Network Analysis

Graph theory provides a mathematical framework for representing and analyzing complex networks and has become one of the most widely adopted approaches for studying the topological organization of functional brain networks. Within the broader field of network science, graph theory enables the characterization of complex systems by describing both their structural organization and their information exchange patterns through quantitative topological measures [42]. In the context of EEG connectivity analysis, the brain can be modeled as a graph in which nodes represent EEG channels or reconstructed cortical regions, while edges correspond to functional connections estimated using a selected connectivity measure [39]. The resulting graph provides a simplified mathematical representation of the brain network that facilitates the investigation of both local interactions between neighboring regions and the global organization of the entire network [42].

Once the connectivity matrix has been computed, graph theoretical analysis allows the quantitative characterization of the organization of the resulting network. Graphs may be weighted or binary, depending on whether the strength of the connections is preserved or thresholded, and directed or undirected, according to whether the connectivity measure provides information about the direction of information flow. Consequently, the properties of the resulting graph depend not only on the

selected connectivity estimator but also on network construction procedures, including threshold selection and graph density, which can substantially influence the derived topological measures [41].

Graph theoretical metrics can be broadly divided into global and local measures. Global metrics describe the efficiency and overall organization of information transfer across the entire network, whereas local metrics characterize the connectivity patterns and relative importance of individual nodes or subnetworks. Together, these complementary measures provide insight into two fundamental principles of brain organization: functional integration, which reflects the capacity of distant brain regions to exchange information efficiently, and functional segregation, which describes the specialization of local neuronal processing within highly interconnected groups of regions [42].

Several graph metrics have been widely applied in epilepsy research. Global efficiency quantifies the ability of the network to exchange information efficiently across distant regions, whereas characteristic path length measures the average shortest communication pathway between nodes. The clustering coefficient evaluates the tendency of neighboring nodes to form interconnected groups, while modularity measures the extent to which the network can be divided into distinct functional communities. Node strength represents the overall connectivity of individual nodes, whereas centrality measures, including betweenness centrality and eigenvector centrality, identify highly influential regions that may play a critical role in information transfer and network communication [42].

Graph theoretical analysis complements conventional connectivity measures by providing a higher-level description of brain network topology rather than focusing exclusively on pairwise relationships between EEG signals. This systems-level perspective enables the investigation of how functional interactions are organized across the entire brain network and has contributed substantially to the understanding of normal and pathological brain function [40]. In epilepsy, graph theoretical approaches have revealed alterations in both local and global network organization and have contributed to the identification of quantitative biomarkers associated with epileptogenic regions, seizure propagation, treatment response, and surgical outcome. As a consequence, the combined use of functional connectivity and graph theory has emerged as one of the most promising approaches for the quantitative characterization of epileptic brain networks, providing complementary information that cannot be obtained through conventional EEG analysis alone [39].

1.5 Long-term EEG Monitoring in Pediatric Drug-Resistant Epilepsy: Evidence from the Literature

Long-term electroencephalographic monitoring plays a central role in the management of pediatric drug-resistant epilepsy, supporting diagnosis, seizure characterization, presurgical evaluation, treatment optimization, and the development of advanced signal analysis techniques. Several studies have investigated different applications of prolonged EEG monitoring in children with refractory epilepsy, highlighting its clinical and research value. The literature search strategy, study selection procedure, and detailed characteristics of the included studies are reported in the Appendix.

A first group of studies focused on the clinical utility of long-term video-EEG monitoring during diagnostic and therapeutic decision-making. Ghazavi et al. [44] demonstrated that long-term video-EEG monitoring provides valuable information for seizure classification, localization of epileptogenic regions, and treatment planning in children and adolescents with intractable epilepsy. Similarly, Wang et al. [45] evaluated the safety of rapid antiseizure medication withdrawal during long-term video-EEG monitoring, showing that this strategy can facilitate seizure capture while maintaining an acceptable safety profile. Wiegand et al. [46] used prolonged EEG recordings to investigate the electrophysiological effects of everolimus treatment in children with tuberous sclerosis complex and therapy-resistant epilepsy, highlighting the usefulness of EEG monitoring for longitudinal treatment assessment.

Several studies investigated the role of long-term EEG monitoring in presurgical evaluation. Sierra-Marcos et al. [47] analyzed electro-clinical findings and surgical outcomes in pediatric patients with posterior cortex epilepsy, demonstrating the importance of prolonged EEG recordings for identifying epileptogenic regions. Menderes et al. [48] examined the localization and lateralization value of ictal hand postures recorded during video-EEG monitoring, showing that seizure semiology can provide additional information regarding seizure onset zones. Likewise, Liu et al. [49] reported surgical outcomes in 152 children with peri-Rolandic epilepsy, where video-EEG monitoring represented a key component of the presurgical workup. Erdemir et al. [50] demonstrated that children with drug-resistant epileptic spasms can achieve favorable surgical outcomes without intracranial EEG monitoring when non-invasive evaluations, including video-EEG, provide sufficient localization information. Benifla et al. [51] further emphasized the role of prolonged EEG and invasive monitoring in determining whether the hippocampus should be included within the surgical resection in pediatric temporal lobe epilepsy. More recently, Tsai et al. [52] investigated predictors of seizure

recurrence after temporal lobe epilepsy surgery and analyzed the contribution of preoperative and postoperative EEG findings to long-term outcomes.

Long-term EEG monitoring is also fundamental for identifying and characterizing complex electro-clinical manifestations. Di Micco et al. [53] described a pediatric patient with CACNA1E developmental and epileptic encephalopathy in whom prolonged video-EEG monitoring was essential for distinguishing epileptic seizures from movement disorders. This work highlighted the diagnostic value of continuous EEG-video correlation in patients presenting with atypical clinical manifestations.

In parallel with clinical applications, several studies have explored advanced EEG signal analysis techniques using long-term recordings. Zavala-Yoe et al. [54] employed entropy-based measures to investigate the long-term evolution of EEG dynamics in children with Doose and Lennox-Gastaut syndromes, demonstrating the potential of nonlinear signal analysis for characterizing epileptic activity. Rukhsar et al. [55] proposed a patient-specific seizure prediction framework based on long-term scalp EEG recordings from pediatric patients, using multivariate statistical process control and principal component analysis to identify pre-ictal changes and predict seizures before onset.

Recent research has also focused on improving the localization of epileptogenic regions through advanced computational approaches. Irandoost et al. [56] applied Electrical Source Imaging (ESI) to long-term EEG recordings of children with focal epilepsy, demonstrating that source localization techniques can provide complementary information for identifying seizure onset zones and supporting presurgical evaluation. These findings suggest that advanced EEG processing methods may enhance the diagnostic value of conventional long-term monitoring.

Finally, long-term EEG monitoring remains essential even in emerging neuromodulation therapies. Hartnett et al. [57] evaluated responsive neurostimulation (RNS) therapy in pediatric patients with complex medically refractory epilepsy. In this study, prolonged invasive EEG monitoring was used to identify epileptogenic networks and guide electrode implantation, highlighting the continuing importance of long-term electrophysiological monitoring in modern epilepsy management.

Taken together, the literature confirms that long-term EEG monitoring represents a cornerstone in the management of pediatric drug-resistant epilepsy, providing continuous electrophysiological recordings that support both clinical decision-making and the application of advanced quantitative EEG analysis techniques. The growing availability of prolonged EEG recordings has consequently stimulated the search for objective biomarkers capable of extracting clinically relevant information from these complex signals.

Rationale of the Thesis

The systematic literature review conducted in this thesis highlighted the central role of long-term EEG monitoring in the management of pediatric drug-resistant epilepsy. The reviewed studies demonstrated that prolonged EEG recordings represent an essential tool for clinical diagnosis, seizure characterization, presurgical evaluation, treatment assessment, and seizure prediction [44].

However, the reviewed literature also indicated that long-term EEG recordings are predominantly exploited for clinical assessment, whereas the quantitative information contained in prolonged electrophysiological recordings remains comparatively underexplored. Since epilepsy is increasingly understood as a network disorder involving alterations in the interactions among distributed neuronal populations, the analysis of functional relationships between EEG signals represents a relevant approach for investigating changes in brain organization associated with epileptic activity. For this reason, an additional literature search was conducted focusing specifically on functional connectivity and network analysis in EEG studies of epilepsy, with the aim of identifying quantitative methodologies potentially applicable to long-term pediatric EEG recordings.

The reviewed literature showed that functional connectivity can reveal alterations in the interactions among brain regions associated with epileptic activity and has been investigated using a wide range of methodological approaches. Considerable heterogeneity emerged across studies, including measures of linear similarity and correlation, nonlinear and information-theoretic dependence, frequency-domain coupling, phase synchronization, and amplitude coupling. Based on this methodological literature, a complementary set of functional connectivity measures was selected for the present study. These included the Pearson correlation coefficient and magnitude-squared coherence [58], cosine similarity [59], Mutual Information and linear cross-correlation [63], the H^2 coefficient [64], sparse precision matrices [65], partial correlation [60], Phase Locking Value, Phase Lag Index and weighted Phase Lag Index [58], and Amplitude Envelope Correlation [66]. Together, these measures were selected to characterize complementary aspects of functional interactions between EEG signals, as described in Section 2.3.1.

While functional connectivity measures characterize statistical relationships between pairs of EEG signals, graph-theoretical analysis provides a complementary framework for investigating the organization of these interactions at the network level. Accordingly, graph theory has been applied to functional connectivity networks in epilepsy to quantify local and global properties of network

topology. Based on the methodological literature, the graph-theoretical measures selected for the present study included node and mean strength [72], weighted and average weighted clustering coefficients [63], characteristic path length [73], global, local and mean local efficiency [58], closeness centrality and algebraic connectivity [59], betweenness centrality [72], and link density, S-metric and graph energy [59]. These measures allowed the functional connectivity networks to be characterized from complementary local and global perspectives, as described in Section 2.4.1.

Particularly relevant to the present work, several studies have demonstrated the applicability of functional connectivity and graph-theoretical analysis to pediatric scalp EEG. Studies in infants with West syndrome investigated correlation-, coherence-, and phase-based connectivity together with measures of network segregation and integration [58]. Other pediatric studies characterized scalp-EEG functional connectivity networks using both connectivity and topological measures [59]. Functional connectivity has also been investigated in relation to treatment response in pediatric drug-resistant epilepsy [60], while alterations in network organization preceding epileptic spasms have been reported in infants using Mutual Information-based connectivity and graph-theoretical measures [61].

Despite these findings, the literature search conducted in the present thesis indicated that the application of comprehensive functional connectivity and graph-theoretical analyses to long-term scalp EEG recordings in pediatric patients with drug-resistant epilepsy remains limited. Existing studies generally investigate a restricted subset of connectivity measures or address specific clinical objectives, such as epileptogenic-zone localization, treatment response, or seizure prediction, rather than providing a broad and time-resolved characterization of network dynamics throughout prolonged EEG monitoring.

Therefore, the aim of this thesis is to investigate functional brain connectivity in long-term scalp EEG recordings from pediatric patients with drug-resistant epilepsy by integrating complementary functional connectivity and graph-theoretical measures. In particular, the analysis focuses on the comparison between interictal activity and the period preceding seizure onset, with the objective of characterizing changes in network organization associated with the transition toward the ictal state and evaluating whether these quantitative features can distinguish different brain states. By extending the range of connectivity and network measures jointly investigated in long-term pediatric scalp EEG, this work aims to contribute to the identification of potential quantitative biomarkers and to provide a more comprehensive characterization of epileptic network dynamics.

2. Materials and Methods

2.1 CHB-MIT Scalp Electroencephalographic Database Description

The CHB-MIT Scalp EEG Database is a publicly available dataset containing long-term scalp EEG recordings from pediatric patients with intractable epilepsy. The dataset was collected during routine clinical monitoring and is widely used for the analysis of seizure activity and the development of automated detection methods. The main characteristics of the dataset, including population, acquisition protocol, and data structure, are described in the following sections.

2.1.1 Population Description

The CHB-MIT database contains EEG recordings from 23 pediatric patients with intractable seizures. Demographic information is available for 22 patients, including 5 males aged between 3 and 22 years and 17 females aged between 1.5 and 19 years. No age or sex information is available for the remaining patient. The demographic characteristics of the study population are summarized in Table 1. Because the recordings originate from real clinical practice, the demographic information has been anonymized. Moreover, the original acquisition dates were replaced with surrogate dates to protect patient privacy. Therefore, the exact year of recording is not specified in the data files, while the temporal relationships between individual files belonging to each case have been preserved.

Table 1. Age and gender distribution of the pediatric subjects included in the database.

Subject	Gender	Age (years old)
1	Female	11
2	Male	11
3	Female	14
4	Male	22
5	Female	7
6	Female	1.5
7	Female	14.5
8	Male	3.5
9	Female	10
10	Male	3
11	Female	12
12	Female	2
13	Female	3
14	Female	9
15	Male	16
16	Female	7
17	Female	12
18	Female	18
19	Female	19
20	Female	6
21	Female	9
22	Female	6
23	-	-
Overall (n = 23)	5 M / 17 F / 1 N.A.	Mean: 9.84 (n = 22)

2.1.2 Data Acquisition and Dataset Organization

All recordings were collected at the Children's Hospital Boston (CHB) in collaboration with the Massachusetts Institute of Technology (MIT). They were obtained during routine clinical monitoring sessions in which patients were continuously observed for several days for seizure characterization and evaluation for possible surgical treatment. As part of the clinical protocol, antiseizure medications were withdrawn under controlled conditions to increase the likelihood of capturing spontaneous seizure events.

Scalp EEG was recorded according to the international 10–20 system of electrode placement and nomenclature, with a sampling frequency of 256 Hz and 16-bit resolution. The recordings predominantly consist of bipolar EEG derivations, although some sessions include additional auxiliary signals, such as electrocardiographic (ECG) and vagal nerve stimulation (VNS) channels, as well as placeholder or reference channels.

The dataset is organized into 24 case folders, named from *chb01* to *chb24*, corresponding to 23 independent subjects, since two case folders contain recordings from the same patient acquired approximately 1.5 years apart. Across the dataset, differences in derivation configuration are present between subjects and recording sessions. Ten cases show a stable longitudinal bipolar montage consisting of 23 EEG derivations, whereas the remaining cases present variations in derivation configuration, including additional auxiliary or reference channels, placeholder channels, and, in some recordings, changes between bipolar and referential derivations. Despite these variations, electrode placement remains consistent with the international 10–20 system; the heterogeneity primarily concerns the derivation scheme and the presence of additional channels.

Each case folder contains a summary file describing the recording parameters, derivation configuration, recording start and end times, and the number and timing of annotated seizures. EEG recordings are stored in European Data Format (EDF), while seizure annotations provide seizure onset and end times relative to the beginning of the corresponding recording.

Recording duration varies across the dataset. Most EDF recordings are approximately one hour long, whereas recordings from some cases have durations of approximately two or four hours. Most recordings contain 23 simultaneous EEG derivations, although the exact derivation configuration may vary as described above. The recordings within each case folder are not always temporally continuous because some portions of the original monitoring were not captured due to hardware limitations. These interruptions are generally short, although longer gaps may occasionally occur.

The local copy of the CHB-MIT database used in the present study contained 686 EDF recordings distributed across the 24 case folders. The number of recordings retained after standardized derivation selection and preprocessing is reported in Section 3.1.

In addition to the EEG recordings and patient-specific summary files, the database provides supporting documentation containing information on seizure annotations, the complete list of available recordings, the recordings containing annotated seizures, file-integrity checksums, and demographic information. Demographic information is available for 22 of the 23 independent

subjects. The dataset also includes the methodological document by Shoeb and Guttag describing a patient-specific machine-learning approach for seizure detection using the CHB-MIT recordings.

2.2 Data Loading and Pre-processing

The EEG recordings were processed using MATLAB R2026a (MathWorks, Natick, MA, USA), together with EEGLAB 2026.0.0 and the BIOSIG interface. All preprocessing steps were implemented through a custom MATLAB script. Each EDF recording was imported into EEGLAB through the BIOSIG interface without directly importing event annotations, since seizure-related temporal information was subsequently retrieved from the subject-specific summary files. To retain only electrophysiological channels relevant to the present analysis, auxiliary and non-EEG channels were identified according to their labels and removed. These included electrocardiographic channels labelled as ECG or EKG, vagus nerve stimulation channels, electrooculographic channels labelled as LOC, ROC, or EOG, chin- and limb-related auxiliary channels, and channels characterized by empty or non-informative labels. Since some recordings contained channels sharing the same label, duplicated channels were additionally compared sample-by-sample, and a duplicate was removed only when its signal was numerically identical to that of the corresponding channel.

Because the derivation configuration of the CHB-MIT database is not fully homogeneous across recordings, a standardized set of 22 bipolar EEG derivations was defined to obtain an identical network configuration for the subsequent functional connectivity analysis. The retained derivations were FP1-F7, F7-T7, T7-P7, P7-O1, FP1-F3, F3-C3, C3-P3, P3-O1, FP2-F4, F4-C4, C4-P4, P4-O2, FP2-F8, F8-T8, T8-P8, P8-O2, FZ-CZ, CZ-PZ, P7-T7, T7-FT9, FT9-FT10, and FT10-T8. These derivations were selected directly from the channels available in the original EDF recordings and reordered consistently across all retained files; therefore, no additional re-referencing or reconstruction of bipolar derivations was performed. Recordings missing one or more of the required derivations were excluded from subsequent processing to ensure an identical number, identity, and ordering of derivations across recordings.

EEG signals were filtered using finite impulse response (FIR) filters. Specifically, a 1-Hz high-pass filter was first applied to attenuate slow baseline fluctuations. Power-line interference was attenuated using a narrow 59–61 Hz band-stop filter centered at 60 Hz, consistent with the 60-Hz mains frequency used in the United States, where the CHB-MIT recordings were acquired. Finally, a 60-Hz low-pass filter was applied to attenuate higher-frequency components outside the frequency range considered in the subsequent analyses. The resulting EEG signals therefore had a final frequency

range of approximately 1–60 Hz, with additional suppression of power-line interference around 60 Hz. No channel interpolation, automated bad-channel removal, independent component analysis, or wavelet-thresholding procedure was applied, in order to preserve the original inter-derivation relationships and the fixed 22-derivation configuration required for functional connectivity analysis.

Following filtering, each continuous EEG recording was segmented into consecutive, non-overlapping 4-s windows. At the CHB-MIT sampling frequency of 256 Hz, each window contained 1,024 samples. Only complete windows were retained, and any residual segment shorter than 4 s at the end of a recording was discarded.

Seizure annotations were obtained from the subject-specific summary files. For each EDF recording, annotated seizure onset and offset times were mapped onto the corresponding 4-s windows. A window was labelled as ictal whenever its temporal interval overlapped an annotated seizure interval, and the corresponding seizure number was retained. For each non-ictal window, two temporal-distance variables were calculated when the required seizure annotations were available: the time remaining until the onset of the next seizure and the time elapsed since the end of the preceding seizure. For windows overlapping a seizure, both variables were set to zero to explicitly identify the ictal period. These temporal-distance variables were subsequently used to assign each non-ictal window to the preictal or interictal condition according to its temporal relationship with the nearest seizures.

Artifact detection was performed at the window level using EEGLAB's Joint Probability procedure. The use of a probability-based artifact detection approach was adapted from the HAPPILEE (Harvard Automated Processing Pipeline for EEG) framework [62], which was developed for automated preprocessing of pediatric EEG recordings. Joint Probability was applied to the previously defined non-overlapping 4-s windows across the 22 retained EEG derivations, using local and global thresholds of 2 standard deviations. The procedure evaluates the statistical improbability of the signal amplitude distributions within individual derivations and across the multichannel dataset, allowing windows characterized by atypical signal distributions to be identified. Two outputs were retained: a whole-window rejection flag and a derivation-by-window local rejection mask.

A seizure-aware rejection strategy was applied to distinguish annotated ictal activity from non-physiological signal contamination. Ictal windows were labelled separately and excluded from subsequent functional connectivity analysis irrespective of the Joint Probability result, since seizure-related EEG alterations represent pathological activity of interest rather than conventional recording artifacts. For non-ictal windows, the final artifact decision was based on the whole-window Joint Probability rejection flag. Accordingly, a window was considered eligible for functional connectivity

analysis only when it was both non-ictal and not rejected by Joint Probability. The derivation-by-window local rejection mask indicated, for each 4-s window, which of the 22 EEG derivations were individually flagged by the Joint Probability procedure. This derivation-level information was retained for supplementary quality-control purposes but was not used to independently exclude individual derivations or determine whether a window was eligible for functional connectivity analysis.

For each processed EDF recording, the resulting MAT file contained the filtered continuous EEG, standardized derivation labels, 4-s window timing information, seizure annotations and ictal labels, temporal distances from seizures, Joint Probability outputs, and the final window-level eligibility flag for functional connectivity analysis. These outputs constituted the input to the subsequent functional connectivity pipeline, in which connectivity estimates were computed exclusively from windows satisfying the predefined eligibility criteria.

2.3 Functional Connectivity Feature Extraction

Functional connectivity was estimated independently within each valid 4-s EEG window. The selection of connectivity measures was informed by the literature review described in the Rationale of the Thesis. Based on the methodological approaches identified in the literature, a complementary subset of measures was selected to characterize different forms of inter-derivation coupling while limiting methodological redundancy. The selected measures encompassed linear, nonlinear and information-theoretic, phase-based, and amplitude-based approaches.

To preserve a common spatial representation across recordings, connectivity was evaluated between the 22 standardized bipolar EEG derivations retained during preprocessing. Derivation pairs sharing at least one physical electrode were excluded from pairwise connectivity estimation in order to reduce trivial dependencies introduced by the bipolar montage. Specifically, seven measures were computed directly from the preprocessed broadband EEG signal without further decomposition into conventional frequency bands, whereas five additional measures were evaluated separately in the delta, theta, alpha, beta, and gamma frequency bands, resulting in 25 frequency-specific connectivity configurations. This yielded 32 functional connectivity configurations: seven broadband and 25 frequency-specific configurations. The complete set of connectivity measures implemented in the present analysis is summarized in Table 2.

Table 2. Functional connectivity measures computed in the present study.

Connectivity measure	Mathematical definition	Reference
Pearson correlation coefficient (PCC)	$r_{ij} = \frac{\sum_t [(x_i(t) - \bar{x}_i)(x_j(t) - \bar{x}_j)]}{\sqrt{\{\sum_t [x_i(t) - \bar{x}_i]^2 \sum_t [x_j(t) - \bar{x}_j]^2\}}}$	[58]
Cosine similarity (CS)	$CS_{ij} = \frac{\sum_t x_i(t) x_j(t)}{\sqrt{\{\sum_t x_i(t)^2 \sum_t x_j(t)^2\}}}$	[59]
Mutual information (MI)	$MI(X;Y) = \sum_x \sum_Y p(x,y)\, ln\, [p(x,y)/(p(x)p(y))]$	[63]
H² coefficient (H²)	$H^2(X \to Y) = 1 - \frac{Var[Y - \hat{Y}(X)]}{Var[Y]}$	[64]
Sparse precision matrix (SP)	$\hat{\Theta} = \arg\min_{\Theta > 0} \{tr(S\Theta) - \log\det(\Theta) + \lambda \|\Theta\|_{1,off}\}$	[65]
Partial correlation (PC)	$\rho_{ij} \cdot rest = -\frac{\hat{\Theta}_{ij}}{\sqrt{(\hat{\Theta}_{ii}\, \hat{\Theta}_{jj})}}$	[60]
Linear cross-correlation coefficient (LCCC)	$R_{ij}(\tau) = \frac{\sum_t [(x_i(t) - \bar{x}_i)(x_j(t+\tau) - \bar{x}_j)]}{\sqrt{\{\sum_t [x_i(t) - \bar{x}_i]^2 \sum_t [x_j(t+\tau) - \bar{x}_j]^2\}}}$ $\tau * = arg\ max\ \|R_{ij}(\tau)\|, \quad \|\tau\| \leq 0.25\ s$	[63]
Magnitude-squared coherence (MSC)	$C_{ij}(f) = \frac{\|S_{ij}(f)\|^2}{S_{ii}(f) S_{jj}(f)}$	[58]
Phase-locking value (PLV)	$PLV_{ij} = \|\frac{1}{N} \sum_t exp\{j[\varphi_i(t) - \varphi_j(t)]\}\|$	[58]
Phase lag index (PLI)	$PLI_{ij} = \|\frac{1}{N} \sum_t sign\{sin[\varphi_i(t) - \varphi_j(t)]\}\|$	[58]
Weighted phase lag index (wPLI)	$wPLI_{ij} = \frac{\|E\{Im[Z_i(t) Z_j*(t)]\}\|}{E\{\|Im[Z_i(t) Z_j*(t)]\|\}}$	[58]
Amplitude envelope correlation (AEC)	$AEC_{ij} = Corr(\|Z_i(t)\|, \|Z_j(t)\|)$	[66]

Broadband functional connectivity was first characterized using seven measures describing complementary properties of the relationships between EEG signals:

- **Pearson correlation:** quantified linear zero-lag association between pairs of EEG derivations. In the definition reported in Table 2, $x_i(t)$ and $x_j(t)$ represent the EEG signal values recorded from derivations i and j, respectively, at time sample t, while $\bar{x}_i$ and $\bar{x}_j$ represent their mean values within the analyzed 4-s window. The numerator expresses the joint variation of the two mean-centered signals, whereas the denominator normalizes this quantity according to their individual variability. The resulting coefficient r_{ij} therefore describes the strength and direction of the linear relationship between the two signals, ranging from −1 to 1. Positive values indicate a positive linear relationship, negative values indicate an inverse linear relationship, and values approaching zero indicate weak linear association.
- **Cosine similarity:** provided a complementary measure of linear similarity based on the orientation of the two signal vectors. In the definition reported in Table 2, $x_i(t)$ and $x_j(t)$ represent the EEG signal values recorded from derivations i and j, respectively, at time sample t, while CS_{ij} denotes the cosine similarity between the two signals. The numerator corresponds to the inner product of the two signal vectors, whereas the denominator is the product of their Euclidean norms. This normalization reduces the direct influence of the overall vector magnitude and quantifies how similarly the two signals are oriented. Unlike Pearson correlation, the signals were not mean-centered before this calculation; therefore, cosine similarity characterized the similarity of the original signal vectors rather than their covariance around the respective means.
- **Mutual information:** was included to quantify statistical dependence between two EEG signals without assuming a linear relationship. In the definition reported in Table 2, X and Y represent the two EEG signals considered as random variables, while x and y denote their possible discretized values. The term $p(x, y)$ represents the joint probability of observing x and y, whereas $p(x)$ and $p(y)$ represent the corresponding marginal probabilities. The logarithmic ratio compares the observed joint probability with that expected if the two variables were statistically independent. The contributions are summed over all possible combinations of x and y, with larger MI values indicating stronger statistical dependence between the signals. In the present implementation, the marginal and joint probability distributions were estimated using 16 quantile-based bins.
- **H² coefficient:** was used to assess nonlinear directed dependence between two EEG signals. In the definition reported in Table 2, X represents the predictor signal, Y the signal to be

predicted, and $\hat{Y}(X)$ the nonlinear prediction of Y obtained from X. The numerator represents the variance of the residual prediction error, whereas the denominator represents the original variance of Y. H^2 therefore quantifies the proportion of the variability of Y that can be accounted for by a nonlinear function of X. For its estimation, the predictor signal X was divided into 16 quantile-based bins, the conditional mean of Y was estimated within each bin, and the resulting values were interpolated to obtain the nonlinear prediction $\hat{Y}(X)$. Since predicting Y from X is not equivalent to predicting X from Y, H^2 was treated as directional, and both directions of each derivation pair were estimated separately.

- **Sparse precision matrix:** was used to investigate direct statistical relationships between EEG signals. Within each 4-s window, the EEG signals were standardized and their covariance matrix S was calculated. In the definition reported in Table 2, Θ denotes the precision matrix, while $\widehat{\Theta}$ represents its estimated value obtained by minimizing an objective function combining the covariance-based estimation terms with a sparsity-inducing regularization term. Specifically, $\mathrm{tr}(S\Theta)$ and $\log\det(\Theta)$ constitute the covariance-based estimation component, whereas $\| \Theta \|_{1,\mathrm{off}}$ applies an L_1 penalty to the off-diagonal elements, encouraging weak conditional relationships to become zero. The regularization parameter λ controls the strength of this sparsity constraint and was set to 0.10 in the present analysis. Optimization was performed using the Alternating Direction Method of Multipliers (ADMM).
- **Partial correlation:** was subsequently derived from the estimated precision matrix. In the definition reported in Table 2, $\rho_{ij\cdot rest}$ denotes the partial correlation coefficient between derivations i and $j$after accounting for the remaining derivations, $\widehat{\Theta}_{ij}$ is the corresponding off-diagonal element of the estimated precision matrix, and $\widehat{\Theta}_{ii}$ and $\widehat{\Theta}_{jj}$ are the corresponding diagonal elements. Normalization by the square root of the product of the diagonal elements converts the precision-matrix relationship into a partial correlation coefficient, while the negative sign follows the standard relationship between precision and partial correlation. This measure therefore quantified the linear association between two EEG derivations after accounting for the contribution of the remaining derivations in the multivariate signal set.
- **Linear cross-correlation coefficient:** was used to complement zero-lag relationships by evaluating linear similarity at different temporal offsets. In the definition reported in Table 2, $R_{ij}(\tau)$ denotes the normalized cross-correlation between EEG derivations i and j at temporal lag τ, while $x_i(t)$ and $x_j(t+\tau)$ represent the corresponding EEG signal values at time samples t and $t+\tau$, respectively. The terms $\bar{x}_i$ and $\bar{x}_j$ represent the mean values of the two signals. As in Pearson correlation, the numerator quantifies the joint variation of the mean-

centered signals, whereas the denominator normalizes this quantity according to their individual variability. Cross-correlation was evaluated over temporal lags ranging from −0.25 to +0.25 s. The optimal lag τ^* was defined as the lag producing the largest absolute value of $R_{ij}(\tau)$, and the corresponding cross-correlation coefficient was retained as LCCC while preserving its original sign. The selected lag was additionally stored in milliseconds, providing information about the temporal displacement associated with the strongest linear relationship.

Frequency-specific functional connectivity was subsequently evaluated in the delta, theta, alpha, beta, and gamma bands. For the phase- and amplitude-based measures (PLV, PLI, wPLI, and AEC), band-limited analytic signals were obtained by filtering each EEG segment using a fourth-order Butterworth band-pass filter applied in a zero-phase forward-backward configuration. The analytic signal was subsequently obtained through the Hilbert transform, allowing instantaneous phase and amplitude information to be extracted for each derivation. Five frequency-specific connectivity measures were evaluated:

- **Magnitude-squared coherence:** quantified linear coupling between two EEG signals in the frequency domain. In the definition reported in Table 2, $C_{ij}(f)$ denotes the magnitude-squared coherence between derivations i and j at frequency f, $S_{ij}(f)$ represents their cross-spectral density, and $S_{ii}(f)$ and $S_{jj}(f)$ represent the corresponding power spectral densities. The squared magnitude of the cross-spectral density is normalized by the product of the two power spectral densities, providing a frequency-dependent measure of the consistency of the linear relationship between the signals. Coherence was estimated using Welch's method with 1-second Hamming segments, 50% overlap, and an FFT length of 512 samples, and the resulting coherence spectrum was averaged within each frequency band.
- **Phase-locking value:** quantified the consistency of the instantaneous phase difference between two EEG signals within each 4-s window. In the definition reported in Table 2, PLV_{ij} denotes the phase-locking value between derivations i and j, $\varphi_i(t)$ and $\varphi_j(t)$ represent their instantaneous phases at time sample t, N is the number of samples within the window, and j denotes the imaginary unit. Each phase difference is represented as a unit complex vector, and these vectors are averaged over time. Taking the magnitude of the resulting mean vector provides the PLV, with values approaching 1 indicating highly consistent phase differences and values approaching 0 indicating greater variability in the relative phase relationship.
- **Phase lag index:** quantified phase synchronization while specifically considering the sign of the phase difference between the two EEG signals. In the definition reported in Table 2, PLI_{ij}

denotes the phase lag index between derivations i and j. The sine of the instantaneous phase difference indicates whether one signal tends to lead or lag the other, while the sign operator retains only the direction of this phase relationship. Averaging these signs over time and taking the absolute value quantifies the consistency of a non-zero phase lag. Consequently, phase relationships centered around zero lag contribute less to PLI, making the measure less sensitive than PLV to instantaneous synchronization that may arise from common-source effects.

- **Weighted phase lag index:** further refined phase-based connectivity estimation by weighting phase-lag contributions according to the magnitude of the imaginary component of the relationship between the two analytic signals. In the definition reported in Table 2, $wPLI_{ij}$ denotes the weighted phase lag index between derivations i and j, $Z_i(t)$ and $Z_j(t)$ represent their analytic signals, and $Z_j^*(t)$ denotes the complex conjugate of $Z_j(t)$. The operator $\mathrm{Im}[\cdot]$ extracts the imaginary component, while $E\{\cdot\}$ denotes averaging over the samples within the analyzed window. The numerator represents the magnitude of the average signed imaginary contribution, whereas the denominator normalizes this quantity by the average magnitude of the imaginary component. Phase relationships with larger imaginary components therefore contribute more strongly than values close to zero, reducing the influence of small and potentially noise-sensitive phase lags.
- **Amplitude envelope correlation:** provided a complementary amplitude-based measure of functional connectivity. In the definition reported in Table 2, AEC_{ij} denotes the amplitude envelope correlation between derivations i and j, while $|\,Z_i(t)\,|$ and $|\,Z_j(t)\,|$ represent the instantaneous amplitude envelopes obtained from their respective analytic signals. The operator $\mathrm{Corr}(\cdot,\cdot)$ denotes the Pearson correlation between the two amplitude envelopes. AEC therefore quantified the extent to which fluctuations in oscillatory amplitude occurred together over time, independently of the phase-based relationships characterized by PLV, PLI, and wPLI.

For each connectivity configuration, the complete pairwise connectivity matrix was retained rather than reducing connectivity to a single global value, thereby preserving the pattern of functional interactions across the 22 EEG derivations. The resulting window-level connectivity matrices were retained for the subsequent graph-theoretical feature extraction and preictal–interictal statistical analysis.

2.4 Graph-Theoretical Feature Extraction

Following functional connectivity feature extraction, graph-theoretical analysis was performed in MATLAB to further characterize the organization of the resulting functional brain networks. While functional connectivity measures quantified the relationships between individual pairs of EEG derivations, graph theory was used to characterize these interactions at the network level through global and nodal topological features. This approach allowed functional connectivity patterns to be examined in terms of network integration, segregation, and organization.

Graph-theoretical analysis was performed on a selected subset of the functional connectivity matrices previously computed for each valid 4-s window. Specifically, broadband mutual information and the band-specific coherence, PLV, PLI, and wPLI matrices were used for graph construction. These measures were selected because they could be directly represented as undirected, non-negative weighted networks. Pearson correlation, cosine similarity, H^2 coefficient, sparse precision, partial correlation, LCCC, and AEC were not included. Pearson correlation, cosine similarity, sparse precision, partial correlation, LCCC, and the implemented AEC can contain signed values, whereas H^2 is directional. Their inclusion would therefore have required additional transformations to obtain the undirected, non-negative network representation adopted in the present analysis. To maintain a consistent graph-construction criterion across connectivity estimators, these additional transformations were not applied.

For each selected connectivity matrix and each valid 4-s window, a weighted network was constructed in which the 22 bipolar EEG derivations represented the nodes and the functional connectivity value previously calculated between each pair of derivations represented the weight of the corresponding edge. Coherence, PLV, PLI, and wPLI were considered separately in the delta, theta, alpha, beta, and gamma frequency bands, while mutual information was evaluated in the broadband signal. This resulted in a total of 21 graph connectivity configurations. Each window was analyzed independently, providing a time-resolved description of network topology.

Before graph metrics were calculated, each retained connectivity matrix was transformed into a weighted adjacency matrix. Self-connections represented by the main diagonal were excluded. Connections that were unavailable in the original functional connectivity matrices, including pairs of bipolar derivations sharing a common physical electrode, remained absent from the graph. For connectivity measures that were nominally symmetric, small numerical differences between corresponding matrix entries were removed by averaging the two values. No proportional or absolute threshold was applied to remove weak connections. Each adjacency matrix was subsequently

normalized by its maximum finite connection weight, resulting in normalized weights $\widetilde{w}_{ij}$bounded between 0 and 1. The strongest connection within each matrix therefore assumed a value of 1, while the remaining connections were expressed relative to this maximum. This matrix-wise normalization reduced the influence of the different numerical scales of the connectivity estimators and allowed graph topology to be characterized in terms of the relative distribution of connection strengths within each network.

Depending on the graph measure, the normalized weighted adjacency matrix was either used directly or converted into a connection-distance representation. Measures based on connection weights were derived from the weighted network representation, whereas measures based on shortest paths required connection strengths to be converted into topological distances. For these path-based measures, each positive normalized connection weight was converted into a direct connection distance, so that stronger functional connections corresponded to shorter topological distances and weaker connections to longer distances. Connections with zero weight were treated as absent and therefore did not provide a direct path between the corresponding nodes. Shortest weighted-path distances were subsequently calculated from the resulting distance matrix. In the following definitions, d_{ij} denotes the direct distance associated with the connection between nodes $i$and j, whereas d_{ij}^{*} denotes the shortest weighted-path distance between the same nodes, which may involve one or more intermediate nodes. Shortest-path information was used for the calculation of characteristic path length, global efficiency, local efficiency, closeness centrality, and betweenness centrality.

A total of 14 graph-theoretical measures were then evaluated, comprising nine global and five nodal measures. The nine global measures were mean strength, average weighted clustering coefficient, characteristic path length, global efficiency, mean local efficiency, algebraic connectivity, link density, S-metric, and graph energy. These measures characterized complementary aspects of overall network organization, including connectivity strength, segregation, integration, connectedness, density, degree-based organization, and spectral structure. The five nodal measures were node strength, weighted clustering coefficient, local efficiency, closeness centrality, and betweenness centrality, which were calculated separately for each of the 22 EEG derivations to characterize their connectivity and topological role within the network. For local efficiency, shortest-path distances were calculated within the subgraph formed by the neighboring nodes of each individual node, as specified in Table 3. The mathematical definitions used for graph construction and graph-theoretical characterization are summarized in the following table.

Table 3. Mathematical definitions of the graph-theoretical measures used in the present study.

Graph measure	Mathematical definition	Reference
Node strength (NS)	$s_i = \sum_{j \neq i} \widetilde{w}_{ij}$	[72]
Mean strength (MS)	$\bar{S} = \frac{1}{N} \sum_{i=1}^{N} s_i$	[72]
Weighted clustering coefficient (WCC)	$C_i^w = \frac{1}{k_i(k_i-1)} \sum_{j \neq i} \sum_{\substack{k \neq i \\ k \neq j}} \left(\widetilde{w}_{ij} \widetilde{w}_{jk} \widetilde{w}_{ki}\right)^{1/3}$	[63]
Average weighted clustering coefficient (AWCC)	$\bar{C}^w = \frac{1}{N} \sum_{i=1}^{N} C_i^w$	[63]
Characteristic path length (CPL)	$L = \frac{1}{N(N-1)} \sum_{i \neq j} d^*{}_{ij}$	[73]
Global efficiency (GE)	$E_{\text{global}} = \frac{1}{N(N-1)} \sum_{i \neq j} \frac{1}{d^*{}_{ij}}$	[58]
Local efficiency (LE)	$E_{\text{local}}(i) = \frac{1}{N_i(N_i-1)} \sum_{\substack{j,k \in G_i \\ j \neq k}} \frac{1}{d^*{}_{ij}(G_i)}$	[58]
Mean local efficiency (MLE)	$\bar{E}_{\text{local}} = \frac{1}{N} \sum_{i=1}^{N} E_{\text{local}}(i)$	[58]
Closeness centrality (CC)	$CC_i = \frac{N-1}{\sum_{j \neq i} d^*{}_{ij}}$	[59]
Betweenness centrality (BC)	$BC_i = \sum_{s \neq i \neq t} \frac{\sigma_{st}(i)}{\sigma_{st}}$	[72]
Algebraic connectivity (AC)	$a(G) = \lambda_2(L_G)$	[59]
Link density (LD)	$D_{\text{link}} = \frac{2E}{N(N-1)}$	[59]
S-metric (S)	$S(G) = \sum_{(i,j) \in E} k_i k_j$	[59]
Graph energy	$\mathcal{E}(G) = \sum_i \lvert\lambda_i(A)\rvert$	[59]

Before graph-theoretical measures were interpreted, the normalized weighted adjacency matrix was explicitly defined. For each connectivity matrix, w_{ij} denotes the original connection weight between nodes i and j, whereas $\tilde{w}_{ij}$ denotes the corresponding normalized weight. Each available weight was divided by the maximum finite weight in the same matrix according to [63]:

$$\tilde{w}_{ij} = \frac{w_{ij}}{\max_{k \neq l}(w_{kl})}$$

Consequently, the strongest connection in each individual network had $\tilde{w}_{ij} = 1$, while all remaining positive connections were expressed relative to this maximum. N denotes the total number of network nodes, corresponding to the 22 bipolar EEG derivations in the present analysis.

For graph measures based on shortest paths, normalized connection strengths were converted into connection lengths because stronger functional connections should correspond to shorter topological distances. Following the inverse-weight approach for weighted network analysis [74], the direct connection length d_{ij} was defined for positive normalized weights as:

$$d_{ij} = \frac{1}{\tilde{w}_{ij}}, \quad \tilde{w}_{ij} > 0$$

Thus, a maximally normalized connection with $\tilde{w}_{ij} = 1$ had a direct length of 1, whereas progressively weaker connections produced increasingly larger lengths. Connections with zero weight were treated as absent. The symbol d_{ij}^{*} denotes the shortest weighted-path distance between nodes i and j, which may include direct or indirect routes through intermediate nodes. Based on these network representations, the 14 graph-theoretical measures reported in Table 3 were calculated. The individual measures are described below:

- **Node strength:** quantified the overall weighted connectivity of an individual EEG derivation. In the definition reported in Table 3, s_i denotes the strength of node i and was obtained by summing the normalized connection weights $\tilde{w}_{ij}$ between node i and every other node j in the network. A larger s_i therefore indicated that the corresponding EEG derivation was, overall, more strongly connected to the rest of the network.
- **Mean strength:** provided a global measure of the overall weighted connectivity of the network. It was calculated by averaging the node-strength values s_i across all N nodes. Higher values therefore indicated greater overall connection strength across the network.
- **Weighted clustering coefficient:** quantified local network segregation by measuring the extent to which the neighbors of a node formed strongly weighted triangles. In the definition reported in Table 3, k_i denotes the number of nodes directly connected to node i, while j and

$h$denote two of its neighboring nodes. The terms $\widetilde{w}_{ij}$, $\widetilde{w}_{jh}$, and $\widetilde{w}_{hi}$ represent the normalized weights of the three connections forming the triangle $i-j-h$. Their product, raised to the power of one third, represents the geometric mean of the three connection weights and therefore accounts for the intensity of each weighted triangle. These contributions were summed across the triangles involving node $i$and normalized by $k_i(k_i-1)$. Nodes with fewer than two neighbors were assigned a clustering coefficient of zero because no triangle could be formed. Higher values indicated stronger local interconnectedness around the node.

- **Average weighted clustering coefficient:** provided a global measure of network segregation. It was obtained by averaging the weighted clustering coefficients of all N nodes, with higher values indicating a greater tendency toward strongly interconnected local neighborhoods across the network.
- **Characteristic path length:** summarized weighted shortest-path organization at the global level. In the definition reported in Table 3, d_{ij}^{*} denotes the shortest weighted-path distance between distinct nodes i and j. Characteristic path length was calculated from the finite shortest-path distances between node pairs. Lower values indicated that nodes could, on average, be connected through shorter weighted routes and were therefore associated with greater global network integration, whereas larger values reflected longer routes between nodes.
- **Global efficiency:** quantified global network integration from the inverse of the shortest-path distances. For each pair of distinct nodes i and j, the contribution to global efficiency was $1/d_{ij}^{*}$, so that shorter paths contributed more strongly than longer paths. These contributions were summed and normalized by $N(N-1)$, corresponding to the number of ordered pairs of distinct nodes. Unreachable node pairs contributed zero efficiency. Higher values therefore indicated more efficient weighted communication across the network.
- **Local efficiency:** quantified the efficiency of communication among the immediate neighbors of an individual node. In the definition reported in Table 3, G_i denotes the subgraph formed by the nodes directly connected to node i, after removal of node i, while N_i denotes the number of nodes in this neighborhood. The term $d_{jh}^{*}(G_i)$ represents the shortest weighted-path distance between neighboring nodes j and h calculated within this subgraph. The inverse distances were averaged across the possible ordered pairs of neighbors. Higher local efficiency indicated that the neighbors of node i remained efficiently interconnected with one another.

- **Mean local efficiency:** provided a global measure of neighborhood-level integration and was obtained by averaging local efficiency across all N nodes. Higher values therefore indicated greater efficiency of local communication across the network.
- **Closeness centrality:** quantified how centrally a node was positioned with respect to the rest of the weighted network. For node i, the shortest-path distances d_{ij}^{*} from i to the other reachable nodes were considered. In a fully connected network, closeness corresponds to the ratio between $N-1$ and the sum of these distances, so that nodes characterized by shorter paths to the rest of the network have higher closeness values. In the implemented analysis, disconnected networks were additionally adjusted according to the fraction of nodes reachable from i. Higher closeness centrality therefore identified EEG derivations occupying more centrally accessible positions within the network.
- **Betweenness centrality:** quantified the extent to which a node acted as an intermediary along shortest paths connecting other node pairs. In the definition reported in Table 3, σ_{st} denotes the total number of shortest paths between source node $s$and target node t, while $\sigma_{st}(i)$ denotes the number of those shortest paths passing through node i. The ratio $\sigma_{st}(i)/\sigma_{st}$ therefore represents the contribution of node $i$to shortest-path communication between a specific source-target pair. These contributions were accumulated across node pairs and normalized for the undirected network. Higher values indicated nodes that more frequently occupied intermediary positions in the network.
- **Algebraic connectivity:** quantified overall network connectedness from the eigenvalues of the graph Laplacian. The Laplacian was defined as:

$$L_G = D - \widetilde{W}, \qquad D_{ii} = \sum_j \widetilde{w}_{ij}$$

where $\widetilde{W}$ is the normalized weighted adjacency matrix and D is the diagonal strength matrix, whose diagonal elements D_{ii} correspond to the sum of the normalized weights connected to node i. Algebraic connectivity was defined as $\lambda_2(L_G)$, the second-smallest eigenvalue of the graph Laplacian, as reported in Table 3. Values equal or close to zero indicated a disconnected or weakly connected topology, whereas larger values indicated stronger global cohesion of the weighted network.

- **Link density:** quantified the proportion of possible undirected connections that were present in the network. In the definition reported in Table 3, Edenotes the number of observed connections with positive weight, while $N(N-1)/2$ represents the maximum possible

number of undirected connections among N nodes. Values closer to 1 therefore indicated a more densely connected network, whereas lower values indicated that a larger proportion of possible node pairs were not directly connected.

- **S-metric:** characterized the contribution of connections between highly connected nodes. In the definition reported in Table 3, E denotes the set of observed network connections, while k_i and k_j denote the unweighted degrees, namely the numbers of present connections, of the two nodes connected by edge (i,j). For each observed connection, the product $k_i k_j$ was calculated and these products were summed over the complete connection set. Larger S-metric values therefore indicated a greater contribution of connections joining highly connected nodes.

- **Graph energy:** provided a spectral characterization of the normalized weighted network. In the definition reported in Table 3, $\lambda_r(\widetilde{W})$ denotes the r-th eigenvalue of the normalized weighted adjacency matrix $\widetilde{W}$. Graph energy was calculated as the sum of the absolute values of all N adjacency-matrix eigenvalues, thereby summarizing information about the spectral structure of the complete weighted network in a single global value. Unlike path-based measures, graph energy was derived directly from the eigenvalue spectrum of the adjacency matrix.

2.5 Preictal versus Interictal Statistical Analysis

The primary objective of the statistical analysis was to determine whether the extracted functional connectivity and graph-theoretical features differed between the preictal state and a temporally distant interictal baseline. The analysis was performed in MATLAB using the window-level features obtained from the previous processing stages. To avoid pseudoreplication, statistical inference was performed at the subject level rather than treating individual 4-s windows as independent observations. Specifically, feature values were first aggregated across windows belonging to the same temporal condition within each subject, so that each subject contributed one preictal and one interictal estimate to the subsequent group-level comparisons.

From this point onward, the term “valid window” refers to a 4-s window that was eligible for functional connectivity analysis according to the preprocessing criteria described in the previous section, namely a non-ictal window that was not rejected by the whole-window Joint Probability criterion.

For each subject, seizure timing information was extracted from the database summary files and used to determine the temporal relationship between each valid window and the annotated seizures. For subjects with available recording start times, individual EDF recordings were placed on a continuous subject-specific timeline using the reported file start times. Midnight transitions between consecutive recordings were accounted for during timeline reconstruction. The center time of each 4-s window was then used for temporal classification.

Valid windows were temporally classified as preictal, interictal, or excluded according to their relationship with the annotated seizures. Ictal periods were also identified from the seizure annotations but were not included in the preictal–interictal statistical comparison. Following the temporal criteria adopted by Zhong et al. for seizure prediction using the CHB-MIT dataset [68], the preictal interval was defined as the 30 min immediately preceding an eligible seizure onset, whereas interictal periods were required to be at least 4 h distant from seizure activity. When two consecutive seizure onsets were separated by less than 30 min, the later seizure was not used to define an additional preictal interval, since its 30-min preictal period would overlap the preceding seizure and/or the preictal period associated with the preceding seizure [68]. Windows whose center occurred between seizure onset and seizure termination were classified as ictal. The 4-h interictal criterion derived from [68] was implemented by requiring each window to occur at least 4 h after the end of the preceding seizure and at least 4 h before the onset of the subsequent seizure, whenever the corresponding preceding or subsequent seizure was available. This criterion was adopted to obtain an interictal baseline temporally distant from seizure activity and to reduce the inclusion of seizure-related transitional activity in the reference condition. Valid windows that did not satisfy the criteria for either the preictal or interictal condition were excluded from the statistical comparison. Thus, the inferential analysis was restricted to temporally well-defined preictal and interictal periods.

Specific handling was required for two CHB-MIT cases. Although the database contains 24 subject folders, chb01 and chb21 correspond to recordings of the same patient acquired at different times. To prevent the same individual from contributing twice to the group-level paired analysis, chb21 was excluded and chb01 was retained. For chb24, the summary file does not provide the recording start times needed to place the individual EDF files on a continuous subject-level timeline. Consequently, the temporal distance between a window contained in one EDF file and a seizure occurring in another EDF file could not be reliably determined. Temporal classification was therefore based only on seizure timing information that could be established within the same EDF recording, using the same preictal and interictal criteria described above. Windows whose temporal relationship with seizure

activity could not be reliably established were excluded from the statistical comparison rather than being assumed to represent interictal activity.

For each subject, feature values were grouped according to the two temporal conditions considered in the statistical comparison, namely preictal and interictal. Within each condition, values were aggregated across all available valid windows, separately for each feature configuration. A subject-condition combination was retained only when at least five valid 4-s windows were available for that condition. Only subjects for whom both a preictal and an interictal estimate were available for a given comparison were included in the paired statistical analysis. These subjects were defined as *paired subjects*, and a minimum of five paired subjects was required to perform inferential testing. This subject-level aggregation ensured that, despite the potentially large and unequal number of EEG windows available across subjects, each participant contributed a single aggregated estimate per feature and temporal condition to the group-level statistical analysis.

Because normality of the paired differences was not assumed, the Wilcoxon signed-rank test [69] was used to compare preictal and interictal values across subjects. For each comparison, the null hypothesis was that the paired distribution of the considered feature did not systematically differ between the two temporal conditions. Statistical significance was initially evaluated at $p < 0.05$. Since multiple statistical tests were performed within each analysis, the Benjamini–Hochberg false discovery rate (FDR) procedure [70] was subsequently applied. Performing multiple tests increases the probability of obtaining statistically significant results by chance; the FDR procedure was therefore used to control the expected proportion of false discoveries among the results declared significant. FDR-adjusted q-values were obtained, and results with $q < 0.05$ were considered statistically significant after correction. Both uncorrected p-values and FDR-adjusted q-values were retained to distinguish nominally significant results from those remaining significant after correction for multiple comparisons.

In addition to statistical significance, the magnitude and direction of preictal–interictal differences were quantified using paired Cohen's d_z[71]. For subject i, the paired difference was defined as:

$$D_i = P_i - I_i$$

where P_i and I_i denote the preictal and interictal feature estimates, respectively. The paired effect size was then calculated as:

$$d_z = \frac{\overline{D}}{s_D}$$

where $\overline{D}$ is the mean paired difference and s_D is the standard deviation of the paired differences across subjects. Positive d_z values therefore indicated higher feature values during the preictal condition, whereas negative values indicated higher values during the interictal condition. Effect sizes were evaluated alongside the Wilcoxon and FDR results, since statistical significance alone does not quantify the magnitude of the observed difference.

For functional connectivity features, the statistical procedure was independently applied to all 32 connectivity configurations generated during functional connectivity feature extraction. For sparse precision, partial correlation, and LCCC, absolute values were used in the statistical comparison so that the analysis reflected the magnitude rather than the sign of the corresponding connectivity relationship. Within each subject and temporal condition, connectivity matrices were averaged across all available valid windows, producing one representative preictal matrix and one representative interictal matrix for each connectivity configuration. Statistical testing was then performed independently for each usable connection. For symmetric connectivity measures, each derivation pair was considered only once, whereas the directional structure of H^2 was preserved and the two directions between a pair of derivations were treated as distinct connections. Derivation pairs previously excluded because the two bipolar derivations shared a common electrode remained unavailable for statistical testing. FDR correction was applied separately to the connection-wise p-values within each connectivity configuration.

For global graph-theoretical features, statistical comparisons were performed separately for each of the 21 graph connectivity configurations. Within each subject and temporal condition, each of the nine global graph metrics was averaged across the available valid windows. Preictal and interictal subject-level values were then compared using the Wilcoxon signed-rank test. Because nine global graph metrics were evaluated within each graph connectivity configuration, the resulting p-values were corrected across the nine metrics using the Benjamini–Hochberg FDR procedure separately for each connectivity configuration. Paired Cohen's d_z was calculated for each comparison to quantify the magnitude and direction of the preictal–interictal difference.

For nodal graph-theoretical features, the five nodal graph metrics were analyzed separately at each of the 22 EEG derivations. For every graph connectivity configuration and nodal metric, window-level values were averaged within each subject and temporal condition, and preictal and interictal estimates were subsequently compared at each node using the Wilcoxon signed-rank test. The resulting p-values were corrected across the 22 nodes using the Benjamini–Hochberg FDR procedure separately

within each connectivity-configuration and graph-metric combination. Paired Cohen's d_z was also calculated for each node to characterize the magnitude and direction of the observed differences.

Graphical representations were generated as descriptive complements to the formal statistical analyses. For functional connectivity, preictal and interictal connectivity distributions were summarized at the subject level for each of the 32 connectivity configurations. For each subject and temporal condition, the median across the evaluated connections was calculated from the corresponding subject-level connectivity values. The resulting distributions across subjects were then graphically represented for the seven broadband connectivity measures and for the five frequency-specific measures in the delta, theta, alpha, beta, and gamma bands. These visualizations provided a descriptive overview of the differences and overlap between the preictal and interictal conditions, while statistical inference remained based on the connection-wise paired analyses.

For graph-theoretical features, the distribution of paired Cohen's d_z values across the 21 network configurations was visualized for each of the nine global graph metrics. For the nodal analysis, the numbers of nominally significant ($p < 0.05$) and FDR-significant ($q < 0.05$) comparisons were summarized for each of the five nodal graph metrics. Finally, subject-level paired preictal and interictal values were graphically represented for the comparisons that remained statistically significant after FDR correction. These graphical representations were used to illustrate the magnitude, direction, and inter-subject variability of the observed preictal–interictal differences.

2.6 Classification Analysis

A supervised machine-learning analysis was performed to investigate whether the quantitative EEG features extracted in the present study could discriminate between preictal and interictal states. Classification was conceived as a complementary analysis to the conventional statistical comparison, with the aim of evaluating whether multivariate patterns of functional connectivity and graph-theoretical features contained sufficient information to distinguish the two conditions. Two parallel classification analyses were therefore performed: one based on functional connectivity features and one based on global graph-theoretical features.

The classification procedure consisted of two main computational stages. First, dedicated MATLAB scripts were used to construct the classification datasets and aggregate the features obtained from the valid 4-s EEG windows into 5-min observations. Second, preliminary model comparison was performed using the MATLAB Classification Learner application, after which the selected classifier

for each feature set was evaluated using subject-independent leave-one-subject-out (LOSO) cross-validation.

The same definitions of valid windows and the same seizure-based temporal criteria adopted for the preictal–interictal statistical analysis were retained for classification. Therefore, only valid 4-s windows satisfying either the preictal or interictal definition described in Section 2.5 were considered, while valid windows not belonging to either condition were excluded. The same handling of closely spaced seizures and subject-specific cases was also retained.

To obtain more stable observations and reduce the temporal dependence among consecutive 4-s windows, the selected features were aggregated into 5-min blocks. A complete 5-min interval could contain up to 75 non-overlapping 4-s windows, and a block was retained when at least 10 valid windows contributed to its estimate. For preictal periods, the 30 min preceding each eligible seizure were divided into six consecutive 5-min intervals, corresponding to −30 to −25 min, −25 to −20 min, −20 to −15 min, −15 to −10 min, −10 to −5 min, and −5 to 0 min relative to seizure onset. These intervals were defined independently for each seizure, so that the temporal position of each preictal block was always expressed relative to the onset of the specific seizure to which it belonged. Interictal periods satisfying the predefined temporal criteria were divided into consecutive 5-min intervals using the same block duration and minimum-window requirement.

For the functional connectivity classification, each valid 4-s window was represented by one global value for each of the 32 connectivity configurations described in Section 2.3. For each configuration, the finite off-diagonal elements of the corresponding connectivity matrix were averaged to obtain a single window-level connectivity value. Sparse precision, partial correlation, and LCCC values were converted to their absolute magnitude before aggregation, consistently with the functional connectivity statistical analysis. The resulting values were subsequently averaged across the valid 4-s windows contributing to each retained 5-min block. Each block was therefore represented by 32 functional connectivity predictors: seven broadband predictors, comprising Pearson correlation, cosine similarity, mutual information, H^2 coefficient, sparse precision, partial correlation, and LCCC, together with coherence, PLV, PLI, wPLI, and AEC evaluated separately in the delta, theta, alpha, beta, and gamma frequency bands.

A separate classification dataset was constructed using the global graph-theoretical features described in Section 2.4. For each valid 4-s window, nine global graph measures were available for each of the 21 graph connectivity configurations: broadband mutual information and coherence, PLV, PLI, and wPLI evaluated separately in the five frequency bands. The global measures comprised mean strength, average weighted clustering coefficient, characteristic path length, global efficiency, mean

local efficiency, algebraic connectivity, link density, S-metric, and graph energy. Each graph feature was averaged across the valid 4-s windows contributing to the corresponding 5-min block. Consequently, each block was represented by 189 graph-theoretical predictors, corresponding to 21 graph connectivity configurations, with nine global graph measures extracted from each configuration. Nodal graph measures were not included in the classification analysis. The classification analysis was restricted to global graph-theoretical measures to limit feature dimensionality and reduce the risk of overfitting, particularly given the relatively limited number of independent subjects.

For both classification datasets, each row represented one retained 5-min block. Additional variables were stored to identify and characterize each observation, including the subject identifier, block identifier, representative EDF file, class label, temporal position when applicable, and number of contributing 4-s windows. These variables were retained as metadata and were not used as predictors. The binary response variable consisted of the Preictal and Interictal classes.

Because prolonged EEG monitoring naturally provided substantially more interictal than preictal observations, two versions of each classification dataset were generated. The full datasets retained all eligible 5-min blocks, whereas balanced datasets were generated independently within each subject by randomly subsampling the more represented class until equal numbers of preictal and interictal observations were obtained. The random procedure was made reproducible by fixing the MATLAB random-number generator seed. The balanced datasets were used exclusively for preliminary classifier comparison, whereas the corresponding full datasets were retained for the final subject-independent evaluation.

Preliminary model comparison was performed separately for the functional connectivity and graph-theoretical datasets using the MATLAB Classification Learner application from the Statistics and Machine Learning Toolbox. Five-fold cross-validation was used during this stage. Principal component analysis and feature selection were not applied; therefore, all 32 functional connectivity predictors and all 189 global graph-theoretical predictors, respectively, were retained. Subject identifiers, block identifiers, recording information, temporal coordinates, and the number of contributing windows were excluded from the predictor sets. For each feature set, the classifier showing the highest validation performance during this preliminary comparison was selected for the subsequent subject-independent evaluation. The preliminary cross-validation analyses were used exclusively for model selection and were not considered estimates of subject-independent generalization performance.

Since multiple 5-min observations originated from the same patient, conventional row-wise cross-validation could place observations from the same subject in both training and validation folds. Such a partition does not guarantee subject independence and may provide an optimistic estimate of performance on previously unseen patients. Therefore, the classifier selected for each feature set during the preliminary model-comparison stage was subsequently evaluated using a separate MATLAB implementation of LOSO cross-validation.

For the final LOSO evaluation, the corresponding full classification dataset was used rather than the balanced dataset. In each iteration, one independent subject was designated as the held-out test subject, and all 5-min blocks belonging to that subject were completely excluded from model training. The remaining subjects constituted the training dataset. Class balancing was then performed exclusively within the training data of each LOSO fold by randomly subsampling the majority class to match the number of observations in the minority class. The held-out subject was not involved in this procedure, and all eligible observations from that subject were retained for testing. Consequently, no information from the test subject contributed to training-set construction or classifier fitting.

For each feature set, the classifier selected during the preliminary model-comparison stage was applied within the LOSO framework. This procedure was repeated until every independent subject had served once as the held-out test set, providing separate subject-independent evaluations of the discriminative information contained in functional connectivity and global graph-theoretical features.

Classification performance was quantified from the pooled LOSO predictions using overall accuracy, sensitivity for the Preictal class, specificity for the Interictal class, balanced accuracy, and the area under the receiver operating characteristic curve (ROC-AUC). Confusion matrices and ROC curves were generated for both feature sets. Performance was additionally calculated separately for each held-out subject to characterize inter-subject variability. Subject-specific accuracy, Preictal sensitivity, Interictal specificity, balanced accuracy, and ROC-AUC were calculated whenever the corresponding metric could be meaningfully determined from the classes available for that subject. The preliminary five-fold cross-validation results were retained for comparison with the stricter LOSO evaluation in order to assess the effect of enforcing subject independence on classification performance.

3. Results

This chapter presents the results obtained from the complete EEG analysis pipeline. The effect of the preprocessing procedure is first illustrated in representative recordings in order to verify the preservation of the EEG signal within the frequency range of interest and the attenuation produced by the applied filters. Functional connectivity results are then presented, first through descriptive regional and temporal representations and subsequently through the statistical comparison between preictal and interictal conditions. The graph-theoretical results are subsequently reported, including the statistical comparison of global and nodal network measures between preictal and interictal states. Finally, the ability of the extracted functional connectivity and graph-theoretical features to discriminate between preictal and interictal EEG is evaluated through the classification analysis.

3.1 Pre-processing Results

The effect of the preprocessing procedure was examined in both the time and frequency domains. A representative 30-s EEG segment from subject chb01 (chb01_01.edf) was visually inspected before and after preprocessing, using the same temporal interval and four representative bipolar derivations (FP1-F7, F3-C3, T7-P7, and P7-O1), selected across different scalp regions to provide a concise visualization of the preprocessing outcome. As shown in Figure 13, the morphology and temporal organization of the EEG traces remained comparable after preprocessing, with the main electrophysiological patterns visible in the raw recording being preserved in the filtered signals. At the same time, the preprocessing procedure reduced signal components outside the frequency range retained for the subsequent analyses. The close correspondence between the raw and preprocessed traces therefore indicated that filtering did not substantially alter the temporal structure of the recorded EEG activity.

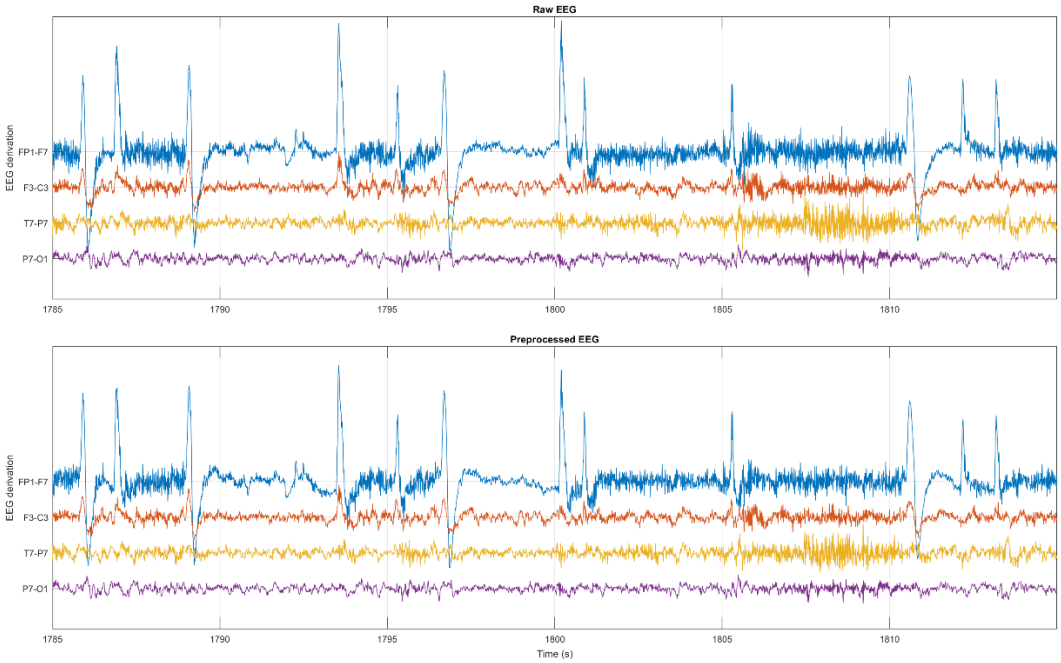


Figure 13. Representative 30-s EEG segment from subject chb01 (chb01_01.edf) before and after preprocessing.

The frequency-domain effect of preprocessing was further evaluated by comparing the power spectral density of the raw and preprocessed EEG. Figure 14 shows the representative PSD obtained from subject chb01 (chb01_01.edf). The PSD was estimated separately for the same four bipolar derivations used for the time-domain visualization (FP1-F7, F3-C3, T7-P7, and P7-O1) and subsequently summarized by computing the median across derivations at each frequency. The raw and preprocessed spectra remained closely comparable over the retained frequency range, indicating preservation of the main spectral characteristics of the EEG signal. A clear attenuation was observed around 60 Hz, corresponding to the 59–61 Hz band-stop filter, while higher-frequency components were attenuated by the 60 Hz low-pass filter. The vertical reference lines indicate the boundaries of the band-stop filter at 59 and 61 Hz and the 60 Hz low-pass cutoff. The comparison illustrates the frequency-selective effect of the applied filtering procedure while showing preservation of the spectral content within the frequency range retained for subsequent analyses.

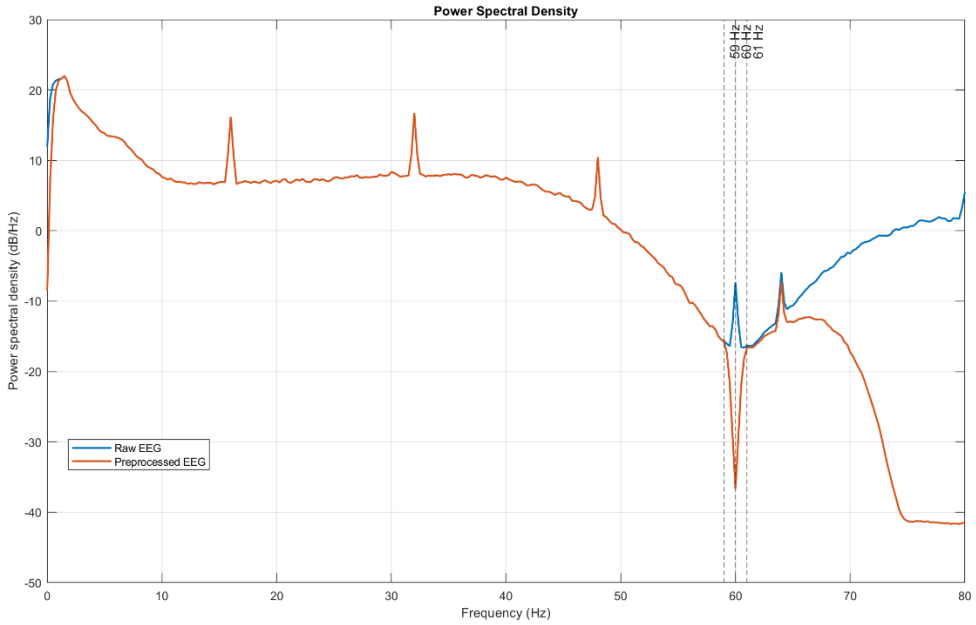


Figure 14. Representative PSD of raw and preprocessed EEG from the first recording of subject chb01.

Across the 686 EDF recordings available in the local CHB-MIT dataset, 654 were successfully preprocessed and produced valid MAT outputs. Thirty-one recordings were excluded because the complete predefined 22-derivation bipolar montage was not available, while one additional recording (chb17b_69.edf) could not be successfully processed. The 654 successfully preprocessed recordings were included in the window-level analysis. Segmentation yielded a total of 855,801 complete non-overlapping 4-s windows. Among these, 2,896 windows (0.34%) overlapped annotated seizure intervals and were therefore labelled as ictal. Joint Probability identified 200,551 windows (23.43%) through the global whole-window rejection criterion. Because ictal windows were treated separately from recording artifacts, the final artifact count was restricted to non-ictal windows rejected by Joint Probability, corresponding to 198,174 windows (23.16% of all windows). After excluding both ictal and artifact-contaminated windows, 654,731 windows (76.51%) remained eligible for functional connectivity analysis.

The Joint Probability procedure also generated 838,212 local derivation-by-window flags. These local flags represent individual derivation–window combinations identified as improbable and therefore should not be interpreted as a number of rejected windows. They were retained as supplementary quality information, whereas eligibility for functional connectivity analysis was determined by the global whole-window rejection decision. The final partition was internally consistent: the 2,896 ictal windows, 198,174 non-ictal artifact windows, and 654,731 usable windows together accounted for all 855,801 segmented windows.

3.2 Functional Connectivity Results

Functional connectivity was evaluated across the complete set of 32 connectivity configurations, including seven broadband measures and five frequency-specific measures computed in the delta, theta, alpha, beta, and gamma bands. Results were examined using complementary descriptive and inferential approaches. Temporal analyses were used to characterize the evolution of connectivity during the 30-min period preceding seizure onset, whereas preictal and interictal conditions were subsequently compared at the subject level. Connection-wise statistical analyses were performed on the complete pairwise connectivity matrices and are presented in Section 3.2.2.

3.2.1 Temporal evolution of functional connectivity during the preictal period

To characterize the temporal evolution of functional connectivity preceding seizure onset, the 30-min preictal period was divided into six consecutive 5-min intervals. Connectivity values were first summarized at the subject level within each interval and subsequently aggregated across subjects. Regional patterns were examined separately within the frontal, central, temporal, parietal, and occipital regions.

Figures 15–20 show the temporal evolution of functional connectivity across the six preictal intervals, separately for the five anatomical regions. Figure 15 reports the seven broadband connectivity measures, whereas Figures 16–20 show the five frequency-specific measures in the delta, theta, alpha, beta, and gamma bands, respectively. In all figures, lines represent the median across subjects, while shaded areas indicate the corresponding interquartile range.

As shown in Figure 15, the seven broadband connectivity measures were characterized by markedly different connectivity magnitudes across the five regions, whereas their temporal profiles were generally stable across the six preictal intervals. Linear cross-correlation and mutual information showed the highest regional connectivity values, while partial correlation remained consistently lower. Although small fluctuations were observed across successive intervals, their direction differed between regions and connectivity measures, and no common monotonic increase or decrease toward seizure onset was evident. Regional differences in connectivity magnitude were also present, but the overall temporal behavior of each measure was broadly comparable across the five regions.

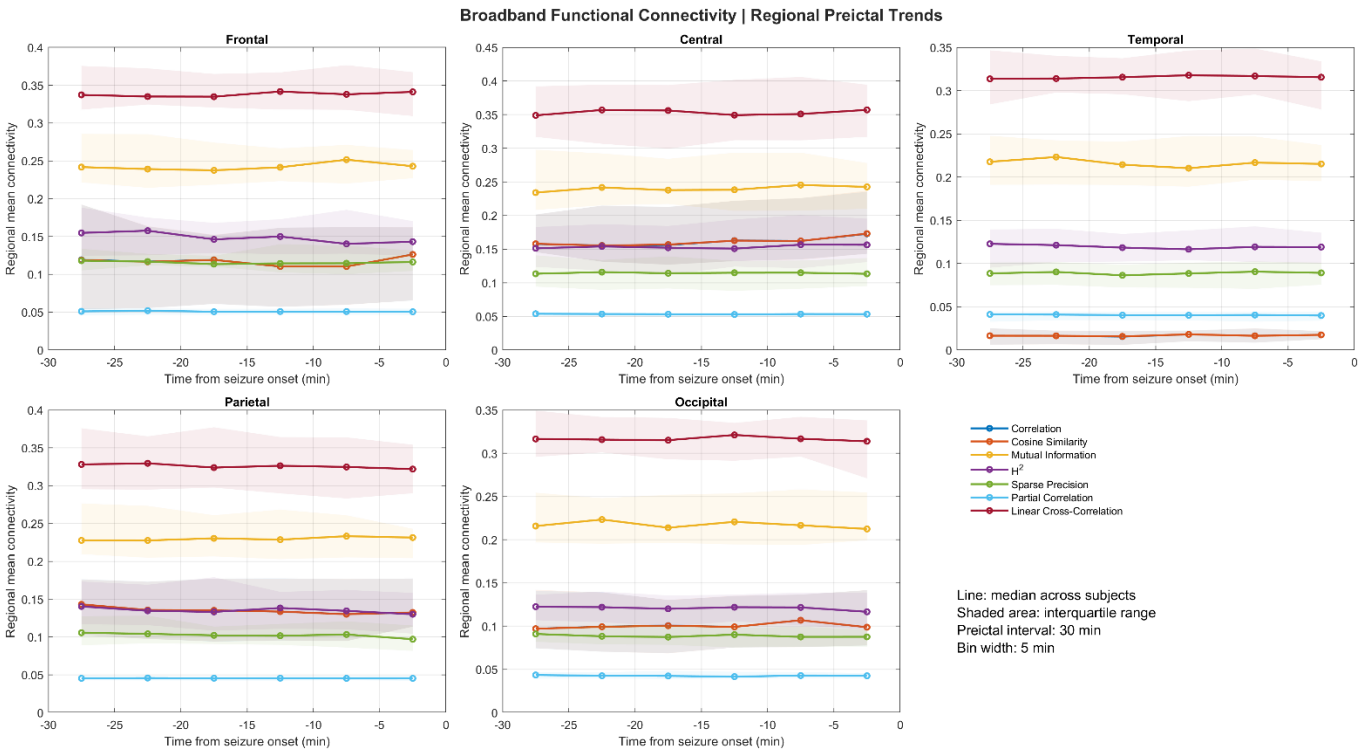


Figure 15. Regional preictal trajectories of broadband functional connectivity.

In the delta band (Figure 16), wPLI and PLV generally exhibited the highest connectivity values across regions, whereas PLI showed lower values. The trajectories remained relatively stable throughout the preictal period. Coherence showed only modest fluctuations, while AEC displayed greater region-dependent variability, with changes occurring in different directions across frontal, central, temporal, parietal, and occipital regions. Therefore, no consistent trend toward seizure onset emerged across regions.

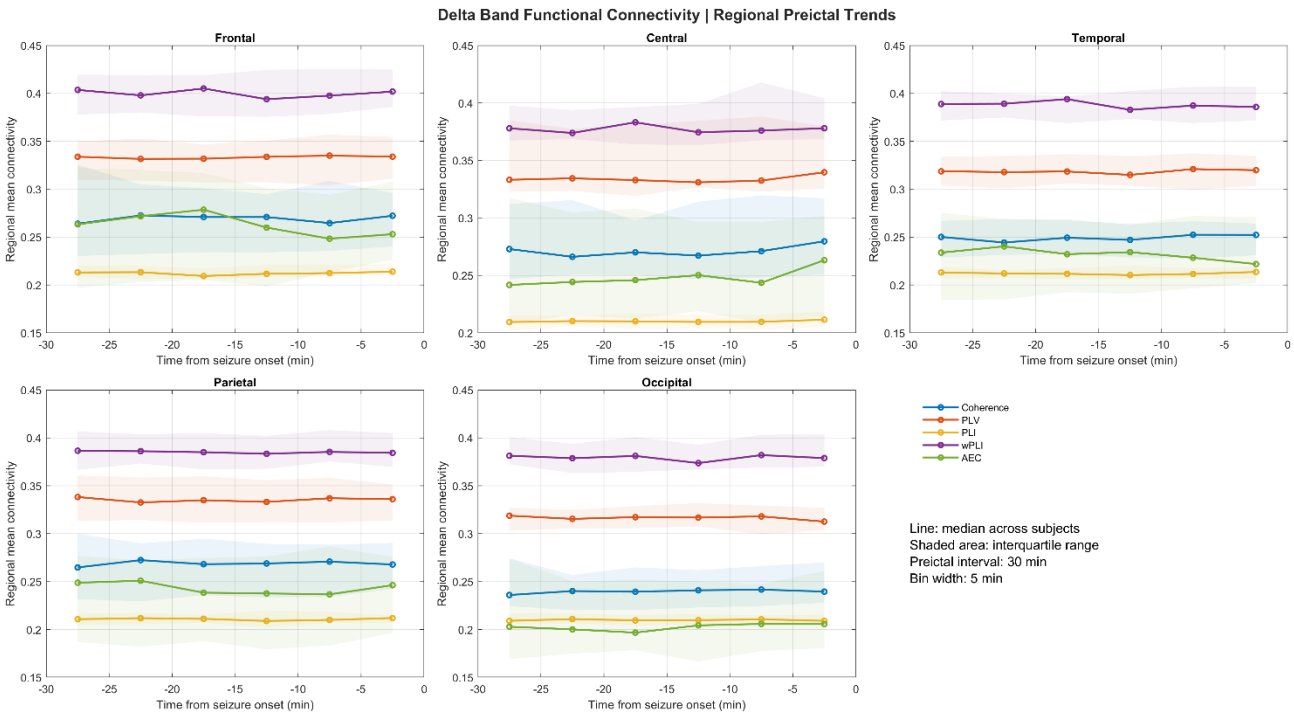


Figure 16. Regional preictal functional connectivity trajectories in the delta band.

A similar pattern was observed in the theta band (Figure 17). wPLI and PLV remained comparatively higher than the other measures, while PLI showed the lowest values across the five regions. Most trajectories showed limited temporal variation. AEC exhibited a gradual increase in the frontal region across the preictal interval, whereas its trajectories in the other regions were more variable and did not show the same progression. Thus, the temporal behavior remained region dependent rather than reflecting a common theta-band trend.

In the alpha band (Figure 18), most connectivity trajectories were again relatively stable across the preictal period. wPLI and PLV generally showed higher connectivity values, whereas PLI and AEC remained lower. AEC exhibited the clearest temporal variability, including increases over part of the preictal interval in the frontal, central, and parietal regions, but these changes differed in timing and magnitude across regions. No consistent temporal progression toward seizure onset was therefore shared across regions or connectivity measures.

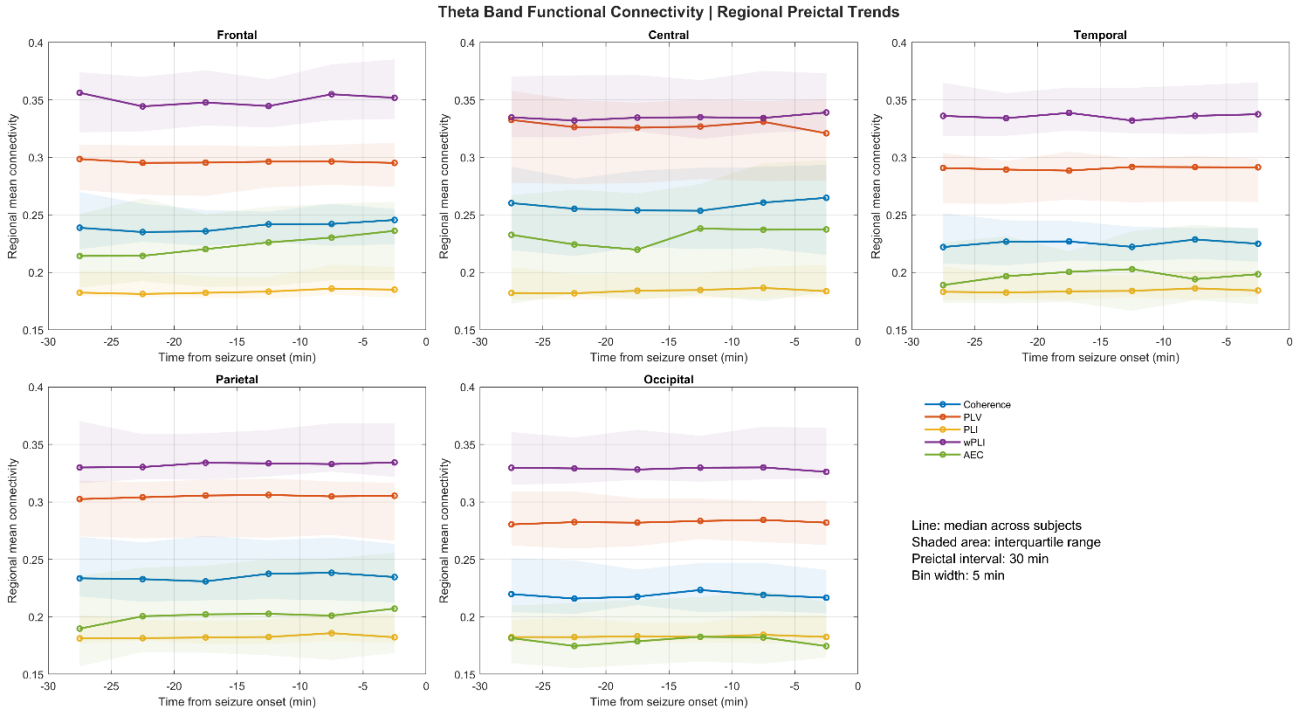


Figure 17. Regional preictal functional connectivity trajectories in the theta band.

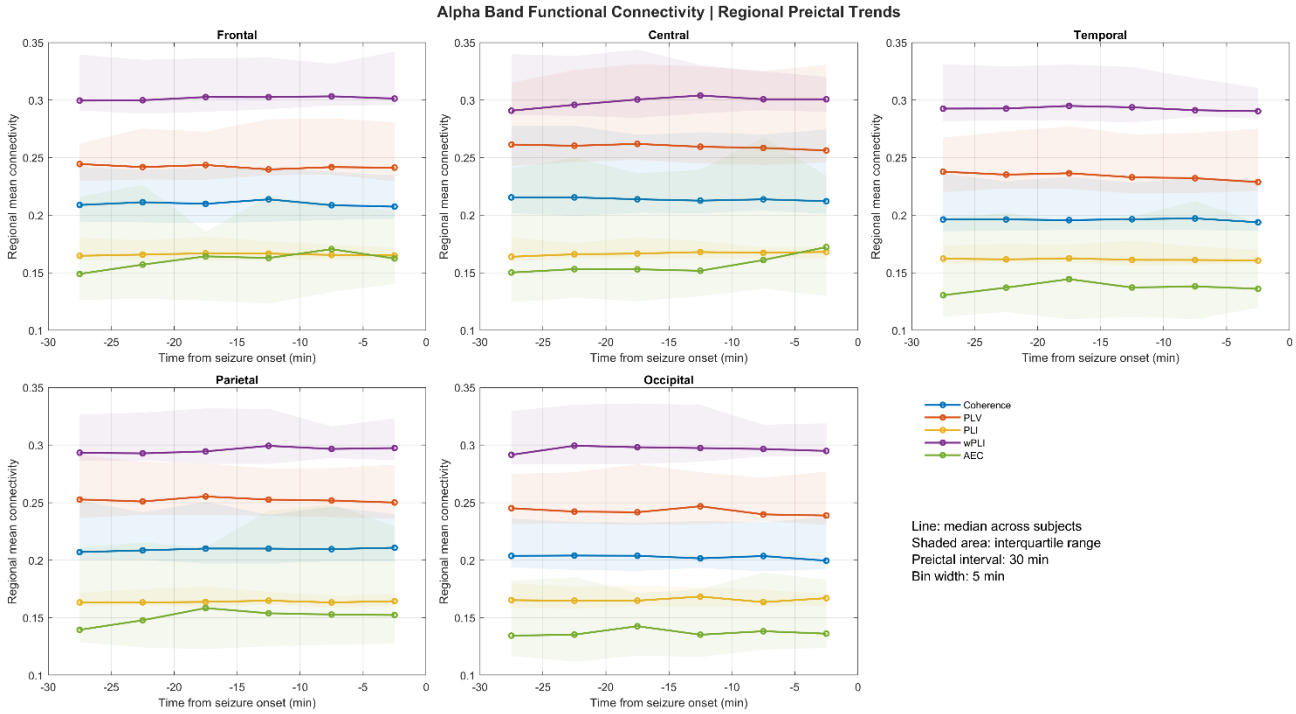


Figure 18. Regional preictal functional connectivity trajectories in the alpha band.

In the beta band (Figure 19), the separation between connectivity measures was reduced compared with the lower-frequency bands. Coherence and wPLI showed similar values in several regions,

whereas PLI and AEC generally remained lower. Some region-specific temporal changes were visible, including modest decreases toward seizure onset for PLV, wPLI, and AEC in the temporal region, while different or non-monotonic trajectories were observed elsewhere. Consequently, no common beta-band temporal pattern was evident across the five regions.

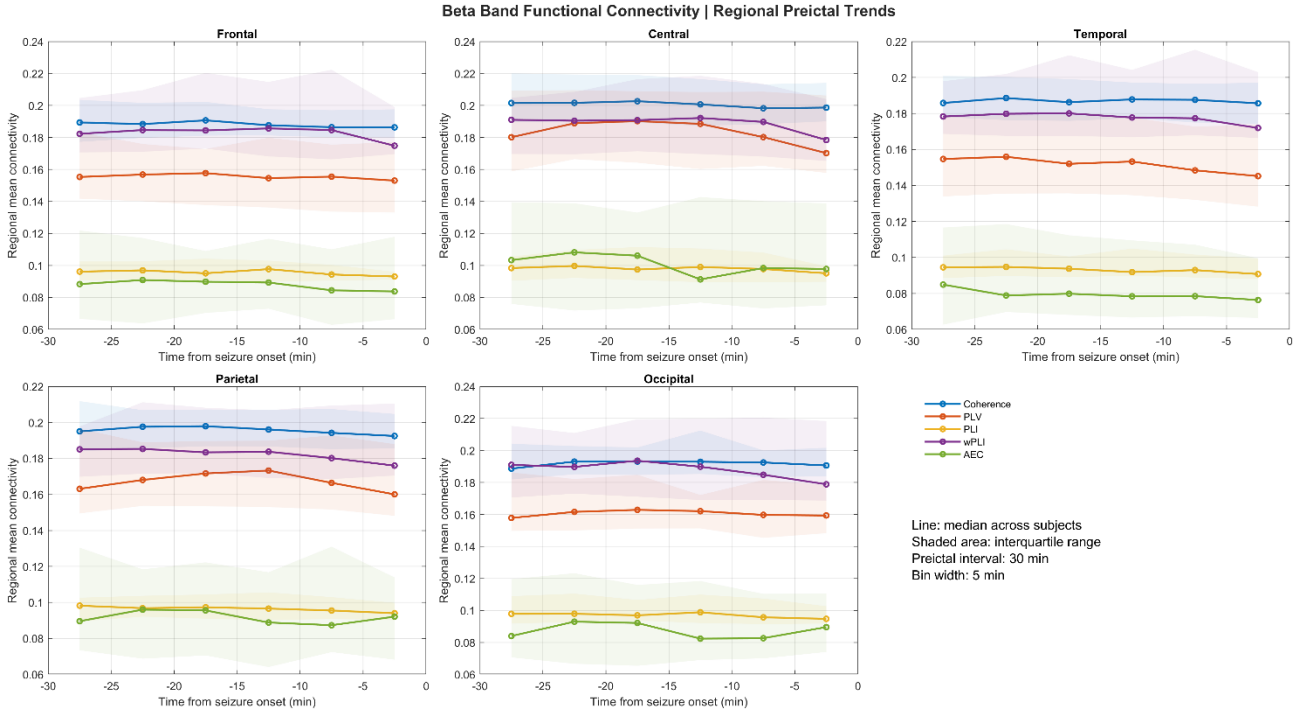


Figure 19. Regional preictal functional connectivity trajectories in the beta band.

Finally, gamma-band connectivity (Figure 20) showed relatively similar trajectories for coherence and wPLI, which remained among the higher connectivity measures across regions, whereas PLI and AEC generally showed lower values. Most trajectories remained stable or displayed only modest fluctuations across the six preictal intervals. AEC showed greater variability in some regions, but these changes were not consistent in direction across the scalp. No common temporal progression toward seizure onset was therefore apparent in the gamma band.

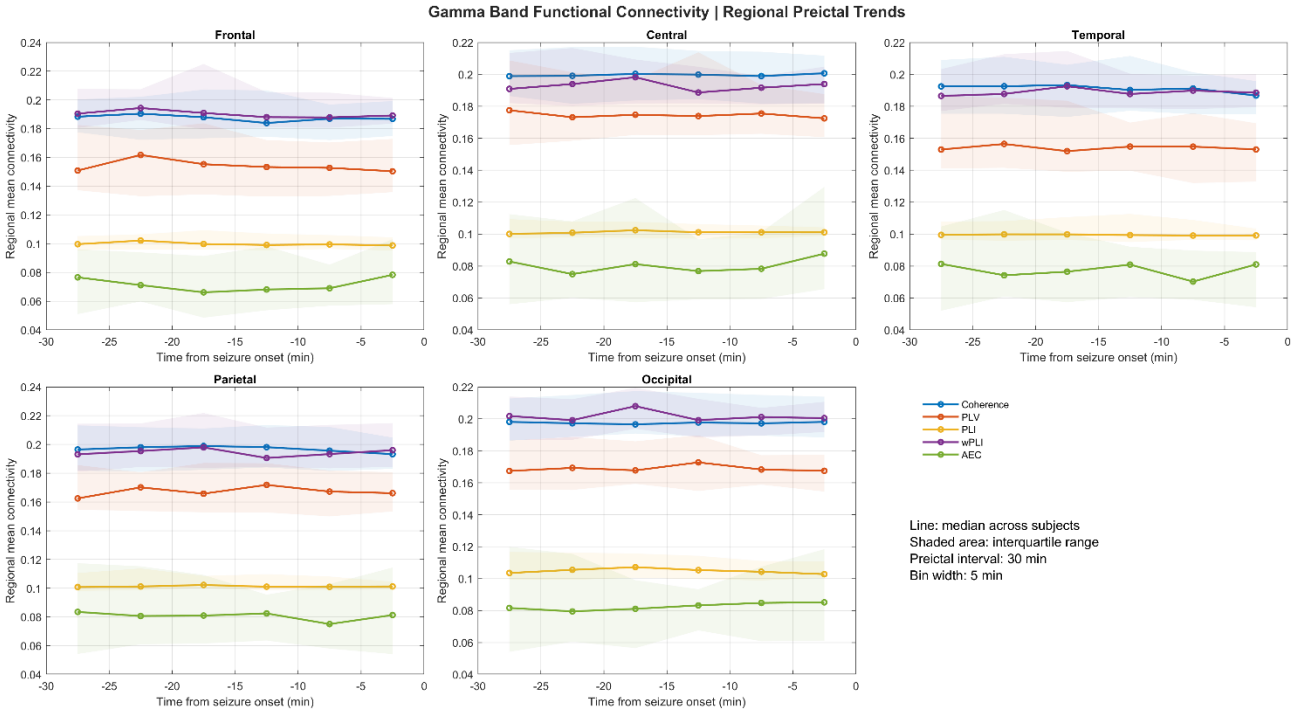


Figure 20. Regional preictal functional connectivity trajectories in the gamma band.

The regional and temporal analysis therefore showed that functional connectivity during the 30-min preictal period was characterized predominantly by relatively stable group-level trajectories, superimposed on differences associated with connectivity measure, frequency band, and anatomical region. Although selected measures showed local temporal fluctuations, these changes varied in direction and magnitude across regions. No uniform temporal pattern approaching seizure onset was visually apparent across the complete set of connectivity configurations. These descriptive findings were complemented by the preictal–interictal statistical analysis reported in the following section.

3.2.2 Preictal versus interictal functional connectivity statistics

The statistical analysis compared preictal and interictal functional connectivity at the level of individual pairs of EEG derivations. For each connectivity configuration and derivation pair, connectivity values were first averaged separately across all valid preictal and interictal windows within each subject, resulting in one preictal and one interictal value per subject. The paired Wilcoxon signed-rank test was then applied across subjects to compare the two conditions. Twenty-one independent subjects had sufficient valid data in both temporal conditions and therefore contributed to the paired analysis. For the symmetric connectivity measures, 204 derivation pairs were evaluated per configuration, whereas the directional H^2 analysis included 408 directed pairs.

Across all connectivity configurations, 254 pairwise comparisons showed nominal p-values below 0.05. However, none of the individual connections remained statistically significant after Benjamini–Hochberg false discovery rate correction at $q < 0.05$. The lowest adjusted value was observed for delta-band PLV, with a minimum q-value of 0.2403. Therefore, these findings were considered nominally significant only at the uncorrected level and were not interpreted as statistically significant evidence of preictal–interictal differences after accounting for multiple comparisons.

The complete statistical results are summarized across all 32 functional connectivity configurations, comprising seven broadband measures and 25 frequency-specific configurations obtained from five connectivity measures evaluated in the delta, theta, alpha, beta, and gamma bands. For each configuration, the summary reports the number of subjects and tested connections, the number of comparisons with uncorrected $p < 0.05$ and FDR-adjusted $q < 0.05$, the minimum p-value and minimum FDR-adjusted q-value, and the maximum absolute paired Cohen's d_z. Broadband results are reported in Table 4, whereas frequency-specific results are presented in Table 5.

Table 4. Pairwise statistical results for the seven broadband functional connectivity measures.

Measure	N	Connections	p < .05	q < .05	Min p	Min q	Max $\|d_z\|$
Correlation	21	204	14	0	0.002961	0.5822	0.759
Cosine Similarity	21	204	14	0	0.003314	0.5822	0.759
Mutual Information	21	204	14	0	0.018969	0.3061	0.539
H^2	21	408	17	0	0.005723	0.6071	0.651
Sparse Precision	21	204	18	0	0.003314	0.4230	0.622
Partial Correlation	21	204	18	0	0.003314	0.5254	0.659
LCCC	21	204	0	0	0.053725	0.9825	0.520

Among the broadband measures, nominal p-values below 0.05 were observed for all configurations except LCCC. Sparse Precision and Partial Correlation showed the largest numbers of nominal comparisons, with 18 connections each, followed by H^2 with 17 directed connections. Correlation, Cosine Similarity, and Mutual Information each showed 14 nominal comparisons. The largest maximum absolute paired effect size among the broadband measures was observed for Correlation ($|d_z| = 0.759$), closely followed by Cosine Similarity ($|d_z| = 0.759$). Nevertheless, no broadband connection remained significant after FDR correction, with the lowest configuration-level minimum q-value observed for Mutual Information ($q = 0.3061$).

Table 5. Pairwise statistical results for the 25 frequency-band-specific connectivity configurations.

Measure	Band	N	Connections	p < .05	q < .05	Min p	Min q	Max $\|d_z\|$
Coherence	Delta	21	204	22	0	0.002642	0.2695	0.683
Coherence	Theta	21	204	12	0	0.009613	0.7761	0.633
Coherence	Alpha	21	204	3	0	0.004615	0.9415	0.537
Coherence	Beta	21	204	1	0	0.045655	0.9816	0.397
Coherence	Gamma	21	204	25	0	0.004137	0.3391	0.669
PLV	Delta	21	204	19	0	0.002356	0.2403	0.771
PLV	Theta	21	204	9	0	0.004615	0.8505	0.720
PLV	Alpha	21	204	3	0	0.002642	0.5391	0.488
PLV	Beta	21	204	0	0	0.062951	0.9861	0.447
PLV	Gamma	21	204	3	0	0.020812	0.7775	0.539
PLI	Delta	21	204	4	0	0.020812	0.9861	0.546
PLI	Theta	21	204	2	0	0.032550	0.9697	0.454
PLI	Alpha	21	204	1	0	0.022809	0.9861	0.299
PLI	Beta	21	204	0	0	0.121932	0.9861	0.385
PLI	Gamma	21	204	2	0	0.009613	0.7801	0.485
wPLI	Delta	21	204	5	0	0.015707	0.9838	0.612
wPLI	Theta	21	204	0	0	0.079215	0.9861	0.444
wPLI	Alpha	21	204	3	0	0.029829	0.9861	0.446
wPLI	Beta	21	204	0	0	0.079215	0.9838	0.402
wPLI	Gamma	21	204	6	0	0.018969	0.5363	0.490
AEC	Delta	21	204	2	0	0.001658	0.3382	0.800
AEC	Theta	21	204	5	0	0.005142	0.9727	0.710
AEC	Alpha	21	204	27	0	0.001658	0.2519	0.881
AEC	Beta	21	204	5	0	0.017270	0.7073	0.514
AEC	Gamma	21	204	0	0	0.053725	0.9629	0.472

The frequency-specific analyses similarly showed nominal preictal–interictal differences across several connectivity measures and frequency bands, but no individual connection survived FDR correction. Alpha-band AEC showed the largest number of nominal comparisons, with 27 of 204 connections presenting uncorrected $p < 0.05$, followed by gamma-band Coherence with 25 and delta-band Coherence with 22. Delta-band PLV showed 19 nominal comparisons and yielded the lowest minimum FDR-adjusted q-value across all 32 connectivity configurations ($q = 0.2403$). The largest absolute paired effect size in the complete connectivity analysis was observed for alpha-band AEC ($|d_z| = 0.881$).

Nominal preictal–interictal differences were distributed across multiple connectivity measures, frequency bands, and derivation pairs. However, none of these differences remained statistically significant after correction for multiple comparisons. The preictal and interictal connectivity distributions were therefore further examined through summary visualizations, while statistical inference remained based on the connection-wise paired analyses reported in Tables 4 and 5.

To provide a complementary descriptive overview of the two conditions, connectivity was additionally summarized at the subject level. For each connectivity configuration, the median across the evaluated connections was calculated separately from each subject's preictal and interictal connectivity matrices, yielding one summary value per subject for each condition. Figures 21–26 show the distributions of these subject-level summary values across subjects. In each boxplot, the central line represents the median across subjects, while the box and whiskers describe the variability of the subject-level values.

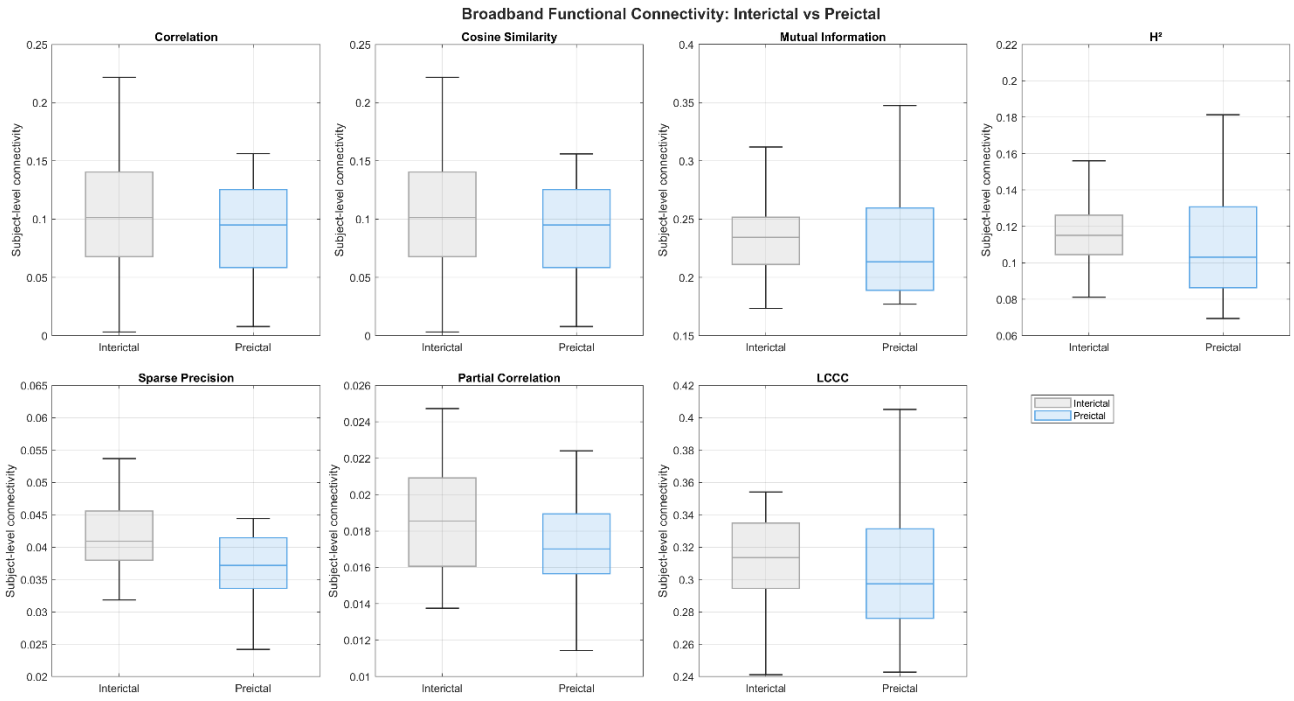


Figure 21. Broadband functional connectivity distributions in the interictal and preictal conditions.

As shown in Figure 21, the distributions of the subject-level summary values showed substantial overlap between the interictal and preictal conditions. The median across subjects was slightly lower in the preictal condition for several broadband measures, including Correlation, Cosine Similarity, Mutual Information, H^2, Sparse Precision, and Partial Correlation, although the magnitude of this

descriptive difference varied across estimators. LCCC showed particularly broad and overlapping distributions.

In the delta band (Figure 22), the interictal and preictal distributions showed substantial overlap across all five connectivity measures, without a consistent directional shift across estimators.

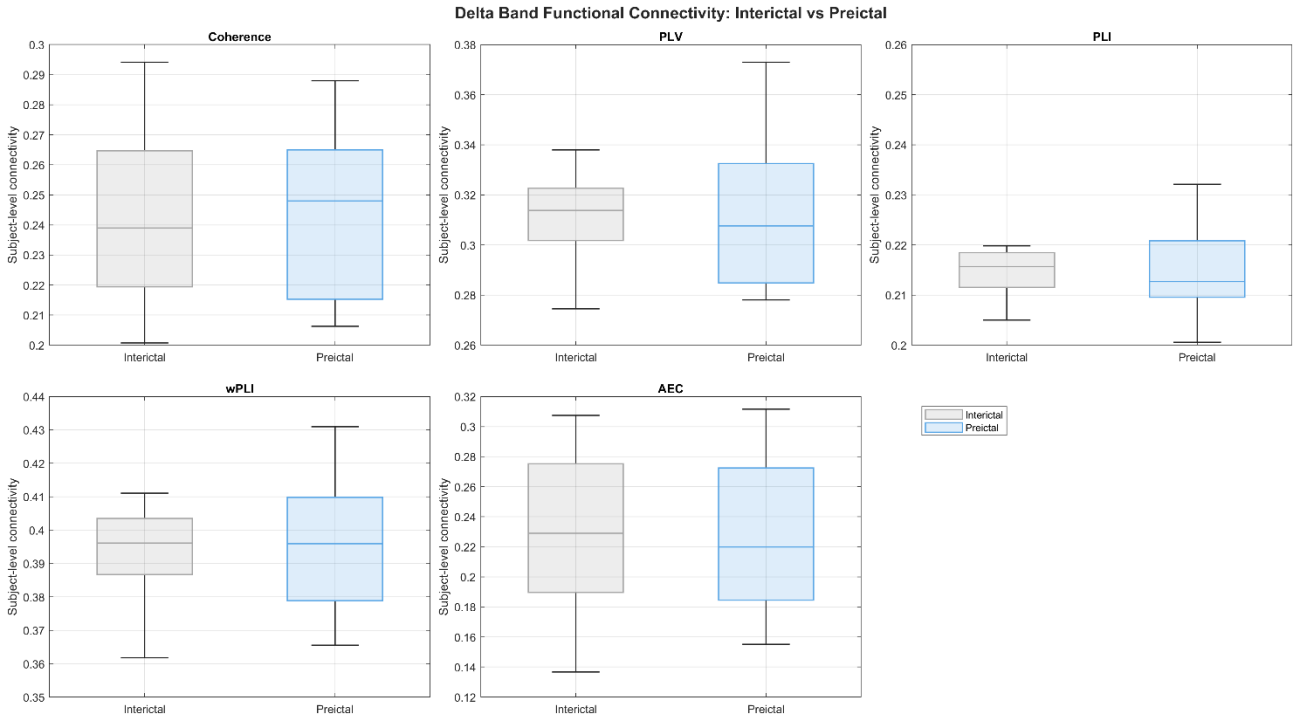


Figure 22. Delta-band functional connectivity distributions in the interictal and preictal conditions.

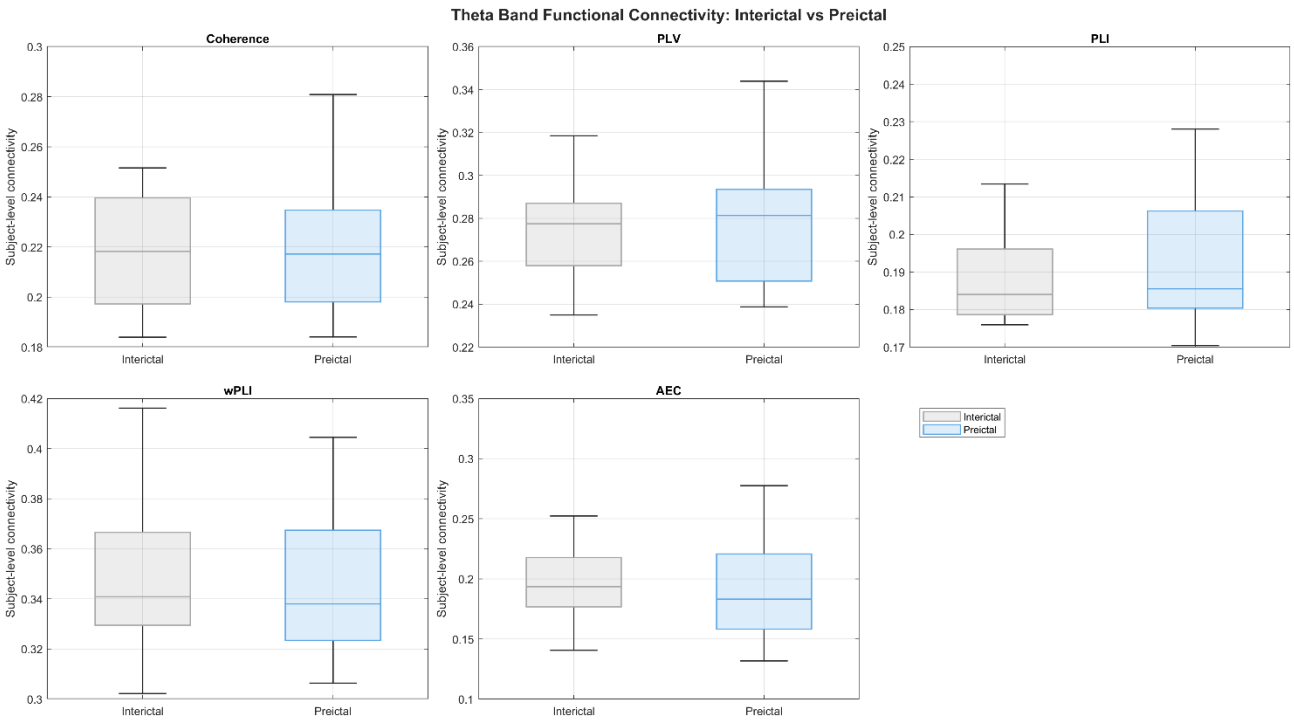


Figure 23. Theta-band functional connectivity distributions in the interictal and preictal conditions.

Theta-band connectivity (Figure 23) similarly showed strongly overlapping interictal and preictal distributions, with only small descriptive shifts in median values and no consistent direction across the five connectivity measures.

In the alpha band (Figure 24), the subject-level distributions remained substantially overlapping across all five connectivity measures. Notably, the edge-specific findings observed for alpha-band AEC were not accompanied by a clear separation of the corresponding subject-level distributions.

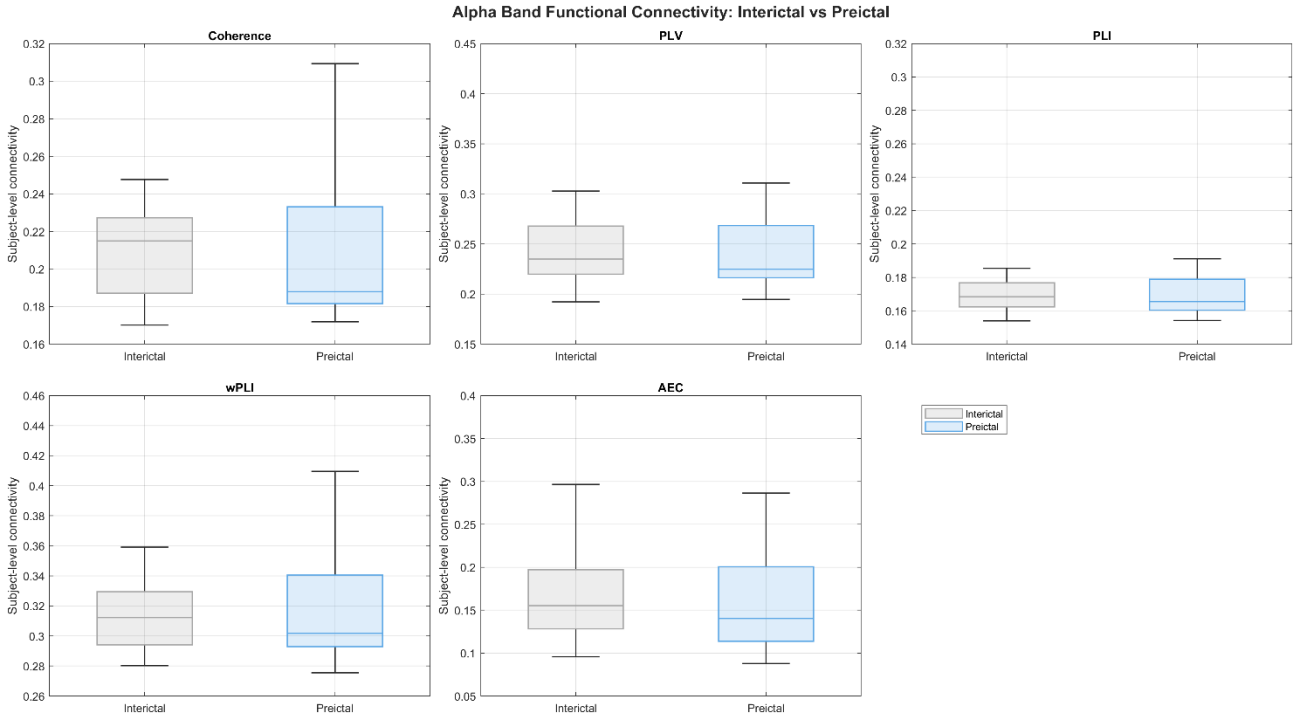


Figure 24. Alpha-band functional connectivity distributions in the interictal and preictal conditions.

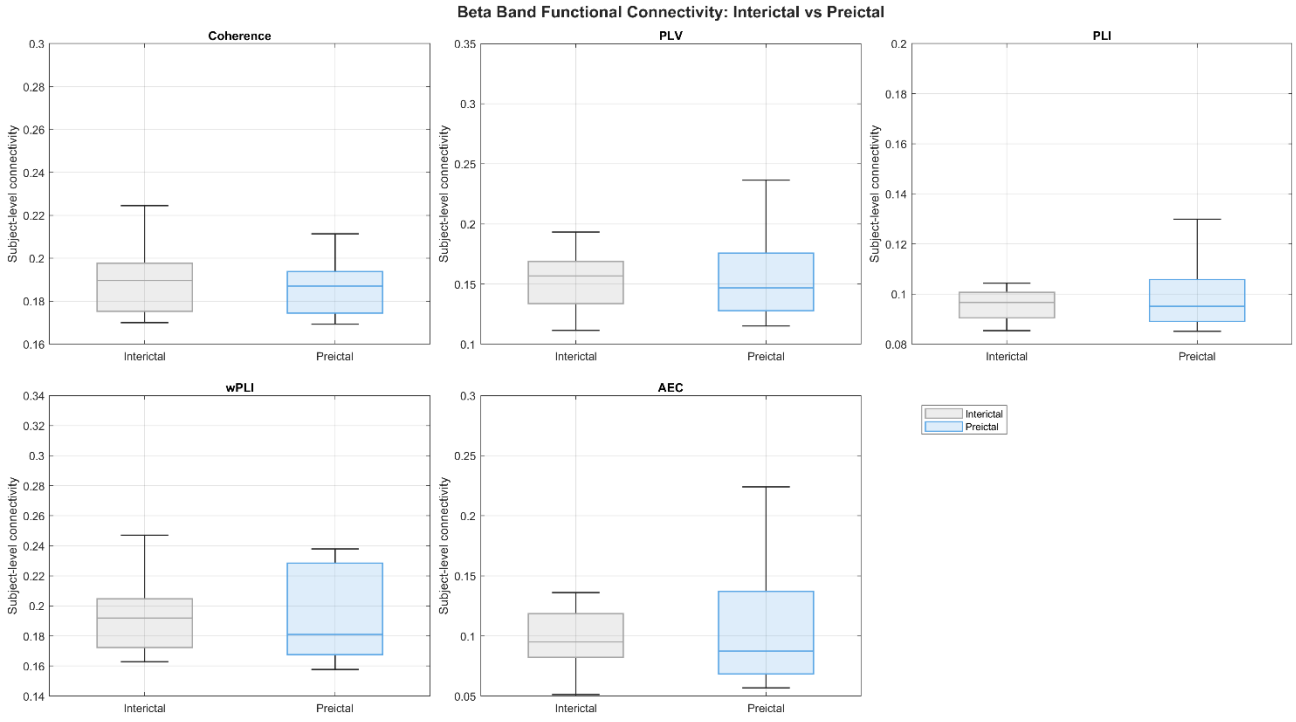


Figure 25. Beta-band functional connectivity distributions in the interictal and preictal conditions.

Beta-band connectivity (Figure 25) also showed substantial overlap between conditions. Median values were similar for Coherence and PLI, whereas PLV, wPLI, and AEC showed modest descriptive reductions in the preictal condition.

In the gamma band (Figure 26), no uniform shift between conditions was apparent across connectivity measures. Coherence and PLV showed similar median values, whereas PLI and wPLI displayed broader preictal distributions. AEC showed a higher preictal median at the descriptive level.

Taken together, the subject-level summary distributions showed substantial overlap between the preictal and interictal conditions, with no consistent direction of change across connectivity measures or frequency bands. Although selected configurations showed descriptive shifts in median connectivity or differences in dispersion, these patterns were not uniform across estimators. At the individual-connection level, nominal differences and moderate-to-large paired effect sizes were observed for selected configurations and derivation pairs, but no connection remained statistically significant after FDR correction.

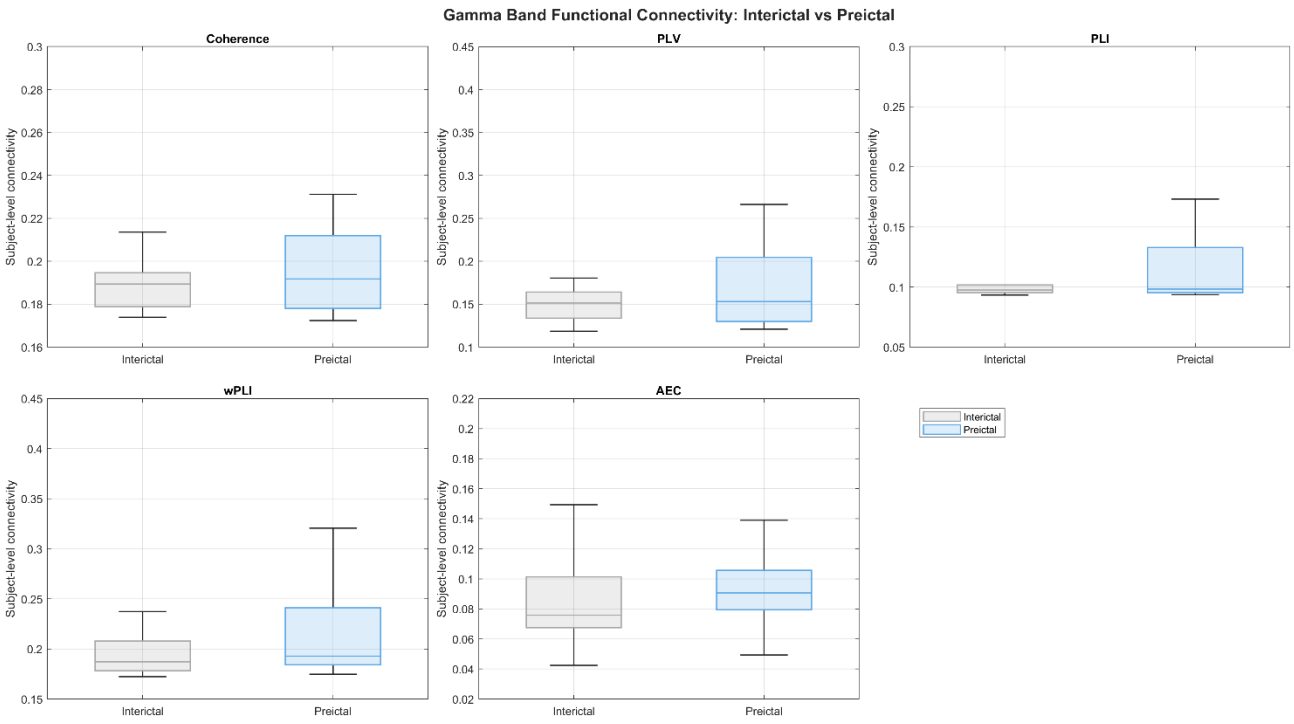


Figure 26. Gamma-band functional connectivity distributions in the interictal and preictal conditions.

3.3 Graph-Theoretical Results

Graph-theoretical analysis was performed on 21 network configurations, comprising broadband mutual information and the band-specific coherence, PLV, PLI, and wPLI measures in the delta, theta, alpha, beta, and gamma bands. For each network configuration, nine global and five nodal graph metrics were evaluated to characterize network organization at the whole-network and node levels, respectively. Preictal and interictal conditions were compared at the subject level using the paired Wilcoxon signed-rank test, with Benjamini–Hochberg false discovery rate correction and paired Cohen's d_z for effect-size estimation. The results are presented in two separate subsections: global graph metrics, describing changes in overall network organization, and nodal graph metrics, examining node-specific differences across the EEG derivations.

3.3.1 Global Graph Metrics

At the global level, nine graph-theoretical metrics were evaluated across 21 network configurations, resulting in 189 comparisons overall. Twenty-one subjects had sufficient valid preictal and interictal data and were included in the paired analysis. For each combination of network configuration and global graph metric, preictal and interictal subject-level values were compared using the paired Wilcoxon signed-rank test. Within each network configuration, the resulting nine p-values were adjusted for multiple comparisons using the Benjamini–Hochberg FDR procedure. Paired Cohen's d_z was also calculated to quantify the magnitude and direction of the differences.

Figure 27 shows the distribution of effect sizes across all 189 global graph-metric comparisons. Each point represents the paired Cohen's d_z obtained for one network configuration. Negative values indicate lower graph-metric values in the preictal condition relative to the interictal condition, whereas positive values indicate higher preictal values. Effect sizes varied in both magnitude and direction across graph metrics and network configurations, without showing a uniform shift toward either higher or lower values during the preictal condition.

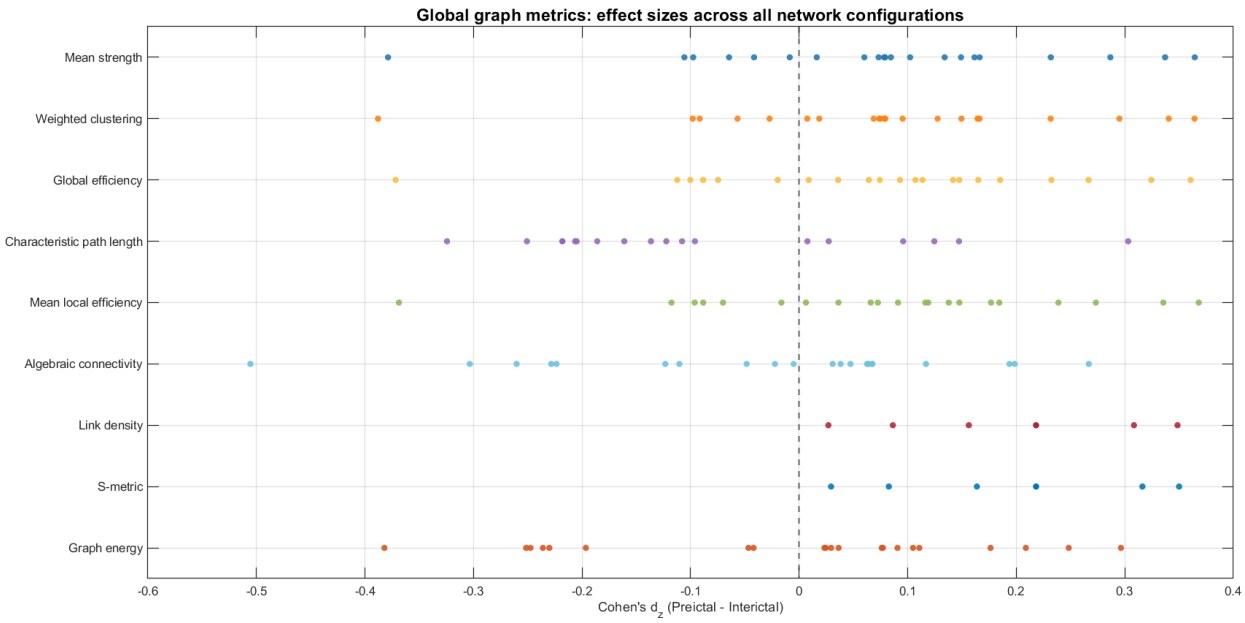


Figure 27. Effect sizes of global graph metrics across the 21 network configurations.

The statistical results are summarized in Table 6. Among the nine global metrics, mean strength, weighted clustering, global efficiency, characteristic path length, mean local efficiency, link density, S-metric, and graph energy showed no nominally significant comparisons across the 21 network configurations. Algebraic connectivity was the only global metric showing nominally significant differences, with two of its 21 comparisons reaching $p < 0.05$.

Specifically, algebraic connectivity derived from broadband mutual information was lower during the preictal condition than during the interictal condition, with mean values of 4.743 and 5.050, respectively. The corresponding effect size was negative ($d_z = -0.506$), with $p = 0.0325$. However, this difference did not remain statistically significant after FDR correction ($q = 0.1958$).

A second nominally significant difference was observed for algebraic connectivity derived from alpha-band coherence, with mean preictal and interictal values of 4.131 and 4.192, respectively ($d_z = -0.260$, $p = 0.0496$). This comparison also did not survive FDR correction ($q = 0.3392$).

Across the complete global analysis, none of the 189 comparisons survived FDR correction at $q < 0.05$. The minimum FDR-adjusted q-value was 0.1958, while the maximum absolute effect size across the nine global metrics was 0.506, observed for algebraic connectivity derived from broadband mutual information. Therefore, no statistically significant preictal–interictal differences were identified at the whole-network level after correction for multiple comparisons.

Table 6. Statistical results for the nine global graph metrics across the 21 functional-connectivity configurations.

Global graph metric	N	Tests	p < .05	q < .05	Min p	Min q	Max $\|d_z\|$
Mean Strength	21	21	0	0	0.113770	0.1958	0.379
Weighted Clustering	21	21	0	0	0.106044	0.1958	0.388
Global Efficiency	21	21	0	0	0.106044	0.1958	0.372
Characteristic Path Length	21	21	0	0	0.169775	0.2183	0.324
Mean Local Efficiency	21	21	0	0	0.130545	0.1958	0.369
Algebraic Connectivity	21	21	2	0	0.032550	0.1958	0.506
Link Density	21	21	0	0	0.113770	0.2910	0.348
S-metric	21	21	0	0	0.113770	0.2910	0.350
Graph Energy	21	21	0	0	0.085341	0.1958	0.382

3.3.2 Nodal Graph Metrics

At the nodal level, five graph metrics were evaluated across the 21 network configurations and 22 EEG derivations, resulting in 462 comparisons for each nodal metric and 2,310 comparisons overall. Twenty-one subjects had sufficient valid preictal and interictal data and were included in the paired analysis. For each combination of network configuration, nodal metric, and EEG derivation, preictal and interictal subject-level values were compared using the paired Wilcoxon signed-rank test, and the resulting p-values were adjusted for multiple comparisons using the Benjamini–Hochberg FDR procedure.

Nominally significant differences before FDR correction were observed for all five nodal metrics, although their number varied considerably across metrics. Node strength showed 10 comparisons with $p < 0.05$, weighted clustering 9, local efficiency 2, and closeness centrality 9. Betweenness centrality showed the largest number of nominal differences, with 38 comparisons reaching $p < 0.05$. Figure 28 summarizes the number of nominally significant and FDR-significant comparisons for each nodal graph metric.

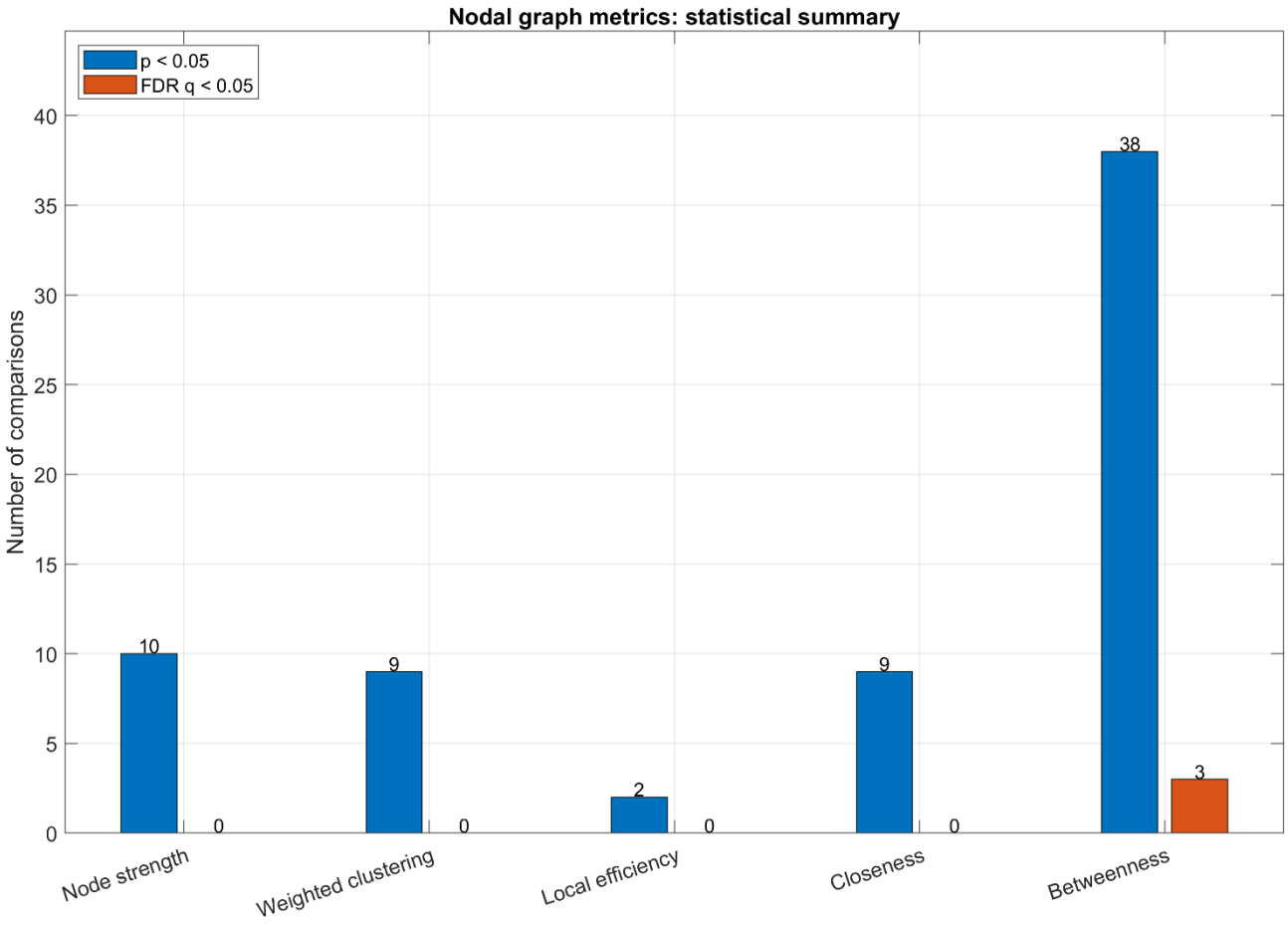


Figure 28. Statistical summary of the five nodal graph metrics.

After FDR correction, none of the comparisons involving node strength, weighted clustering, local efficiency, or closeness centrality remained statistically significant. In contrast, three comparisons involving betweenness centrality remained significant at $q < 0.05$. As reported in Table 7, the minimum FDR-adjusted q-value for betweenness centrality was 0.0120, and its maximum absolute effect size was 0.825. The maximum absolute effect sizes for node strength, weighted clustering, local efficiency, and closeness centrality were 0.712, 0.619, 0.413, and 0.676, respectively.

Table 7. Statistical results for the five nodal graph metrics across the 21 functional-connectivity configurations.

Nodal graph metric	N	Tests	p < .05	q < .05	Min p	Min q	Max |d_z|
Node Strength	21	462	10	0	0.006363	0.1400	0.712
Weighted Clustering	21	462	9	0	0.009613	0.1925	0.619
Local Efficiency	21	462	2	0	0.014269	0.1915	0.413
Closeness Centrality	21	462	9	0	0.011738	0.2172	0.676
Betweenness Centrality	21	462	38	3	0.000543	0.0120	0.825

The three betweenness-centrality comparisons that remained statistically significant after FDR correction are detailed in Table 8, including the corresponding functional-connectivity configuration, EEG derivation, preictal and interictal values, effect size, uncorrected p-value, and FDR-adjusted q-value. Two of the three comparisons showed lower mean betweenness centrality during the preictal condition.

For delta-band PLV at T7–FT9, mean betweenness centrality decreased from 0.0132 in the interictal condition to 0.0119 in the preictal condition ($d_z = -0.825$, $p = 0.0005$, $q = 0.0120$). This comparison showed the largest absolute effect size among the FDR-significant nodal findings and the lowest FDR-adjusted q-value. A reduction was also observed for gamma-band wPLI at F8–T8, with mean values decreasing from 0.0292 interictally to 0.0260 preictally ($d_z = -0.685$, $p = 0.0012$, $q = 0.0254$).

In contrast, beta-band wPLI at FP2–F8 showed an increase in mean betweenness centrality from 0.0343 in the interictal condition to 0.0383 in the preictal condition ($d_z = 0.733$, $p = 0.0019$, $q = 0.0410$). The direction of these significant changes varied across connectivity configurations and EEG derivations, suggesting a spatially and frequency-dependent pattern rather than a uniform preictal alteration.

Table 8. FDR-significant nodal betweenness centrality results.

FC Configuration	Node	Preictal	Interictal	d_z	p	q
PLV delta	T7-FT9	0.0119	0.0132	−0.825	0.0005	0.0120
wPLI beta	FP2-F8	0.0383	0.0343	+0.733	0.0019	0.0410
wPLI gamma	F8-T8	0.0260	0.0292	−0.685	0.0012	0.0254

The subject-level paired values corresponding to these three significant comparisons are shown in Figure 29. Delta-band PLV at T7–FT9 and gamma-band wPLI at F8–T8 predominantly showed a

decrease in betweenness centrality from the interictal to the preictal condition, whereas beta-band wPLI at FP2–F8 showed the opposite direction. Inter-subject variability was nevertheless present across all three comparisons.

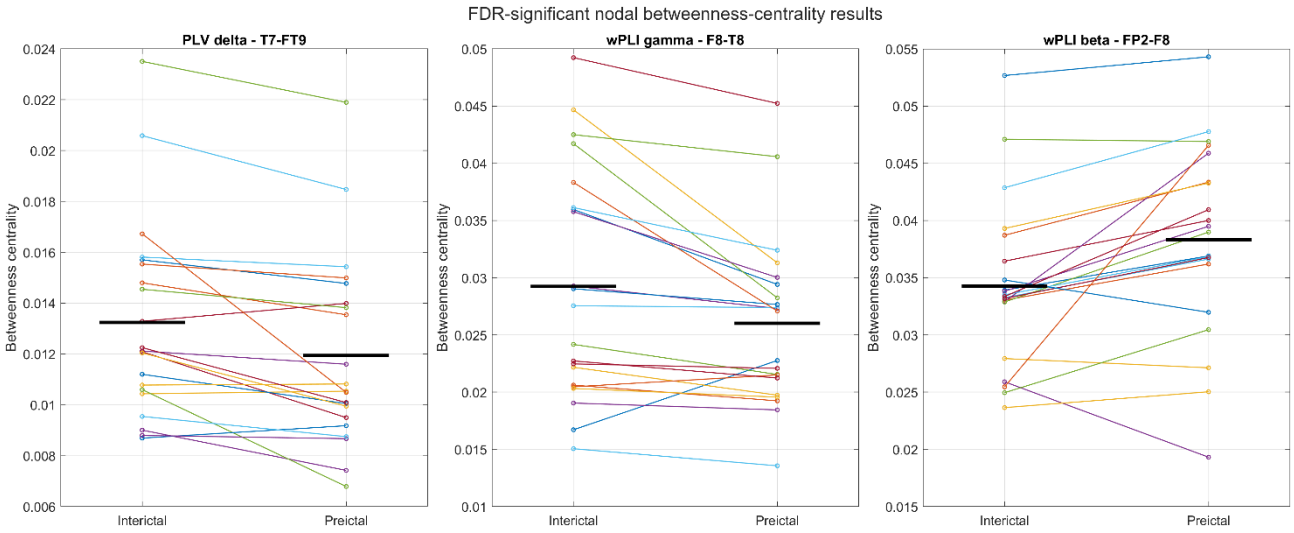


Figure 29. FDR-significant preictal–interictal differences in betweenness centrality.

The nodal analysis revealed a spatially specific pattern of preictal–interictal differences across EEG derivations. Significant differences after correction for multiple comparisons were restricted to betweenness centrality and involved specific combinations of frequency band, functional-connectivity measure, and EEG derivation. Since betweenness centrality reflects how frequently a node lies along the shortest paths connecting other nodes, these findings suggest that the relative network role of specific EEG derivations may change during the preictal state. No FDR-significant differences were identified for the remaining four nodal graph metrics.

3.4 Classification Results

Two parallel classification analyses were performed to evaluate the discrimination between preictal and interictal EEG states using functional connectivity and global graph-theoretical features, respectively. For both feature sets, preliminary model selection was first performed using five-fold cross-validation on the balanced dataset, followed by subject-independent evaluation using leave-one-subject-out (LOSO) cross-validation on the full dataset.

3.4.1 Functional Connectivity-Based Classification

For the functional connectivity analysis, preliminary model selection was performed in MATLAB Classification Learner using five-fold cross-validation and all 32 functional connectivity predictors. The best-performing model was a Fine Gaussian Support Vector Machine (SVM), which achieved a validation accuracy of 84.0%. The selected configuration used a Gaussian kernel with a kernel scale of 1.4, a box constraint of 1, predictor standardization, and no principal component analysis.

The selected Fine Gaussian SVM was subsequently evaluated under the stricter LOSO procedure using the full classification dataset. The dataset contained 6,751 eligible 5-min blocks from 23 independent subjects, including 757 preictal and 5,994 interictal observations. Pooling the predictions obtained across all LOSO folds, the classifier correctly identified 5,186 of 5,994 interictal blocks and 166 of 757 preictal blocks. Based on these pooled predictions, the overall accuracy was 79.28%, with a preictal sensitivity of 21.93%, an interictal specificity of 86.52%, a balanced accuracy of 54.22%, and a ROC-AUC of 0.533.

The pooled LOSO predictions are summarized by the confusion matrix shown in Figure 30.

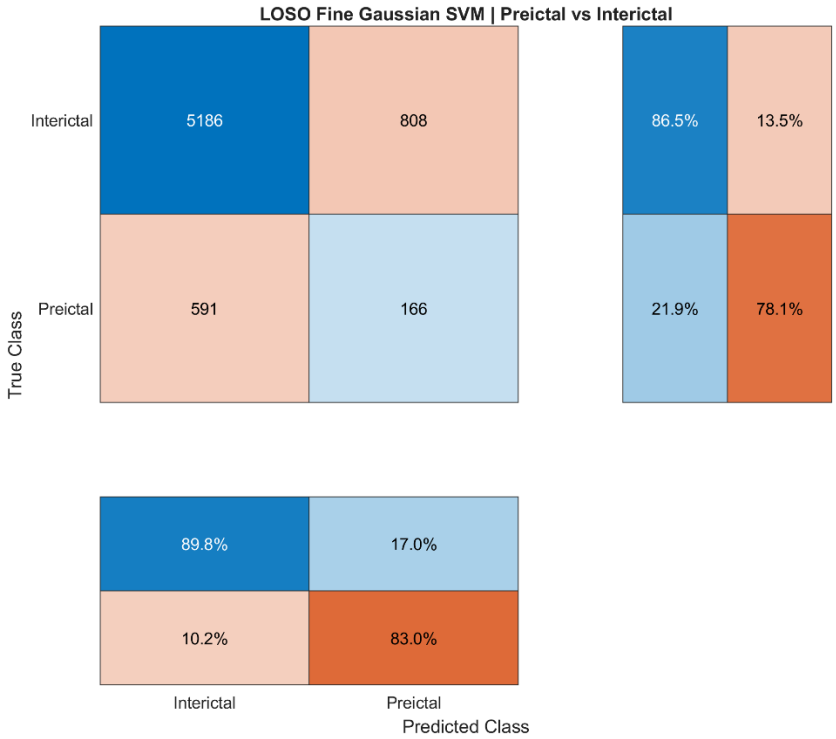


Figure 30. Pooled LOSO confusion matrix for the Fine Gaussian SVM.

The confusion matrix showed a marked asymmetry between the two classes. Interictal blocks were correctly classified with high specificity, whereas only a limited proportion of preictal blocks was correctly identified. Consequently, although the overall accuracy was relatively high, this value was strongly influenced by the predominance of interictal observations in the full dataset. Balanced accuracy therefore provided a more informative summary of performance across the two classes and reached 54.22%.

The corresponding pooled receiver operating characteristic curve is shown in Figure 31. The ROC-AUC obtained under LOSO evaluation was 0.533, indicating limited discrimination between preictal and interictal blocks when predictions were performed on previously unseen subjects.

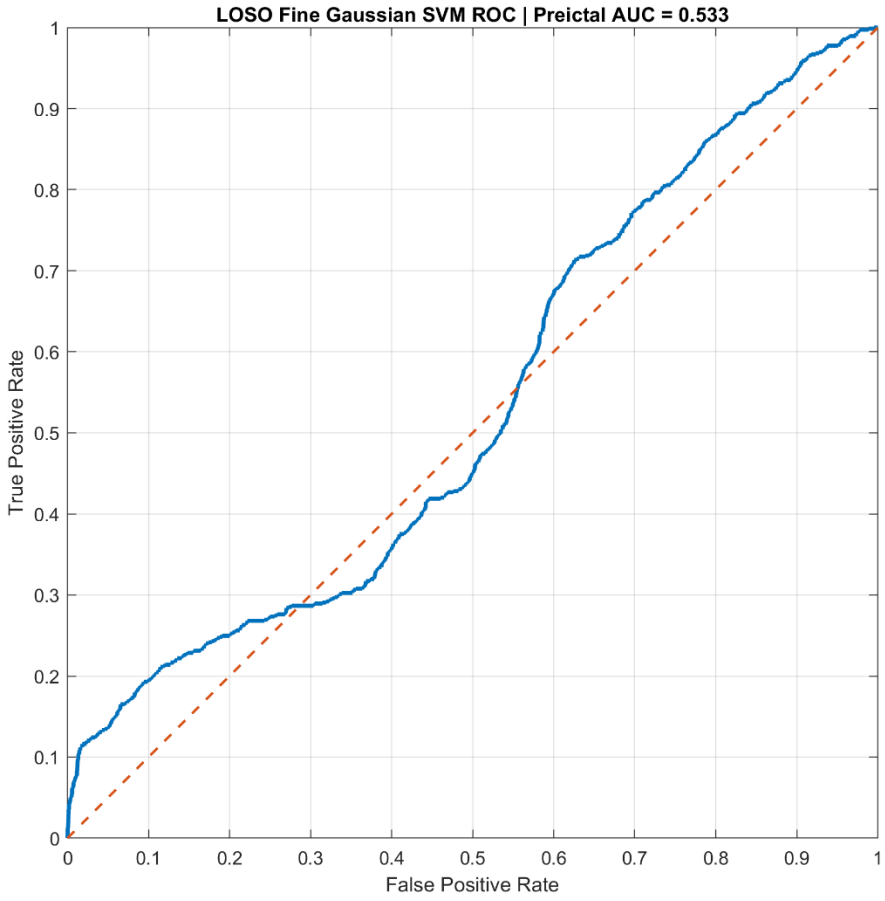


Figure 31. Pooled LOSO ROC curve for preictal–interictal classification.

The ROC curve remained close to the chance diagonal over a substantial portion of the operating range. The marked reduction in performance relative to the preliminary five-fold cross-validation indicates that the discrimination observed during model selection did not generalize with comparable strength to previously unseen subjects.

Subject-wise performance was also examined to characterize inter-subject variability. Balanced accuracy for each held-out subject is reported in Figure 32.

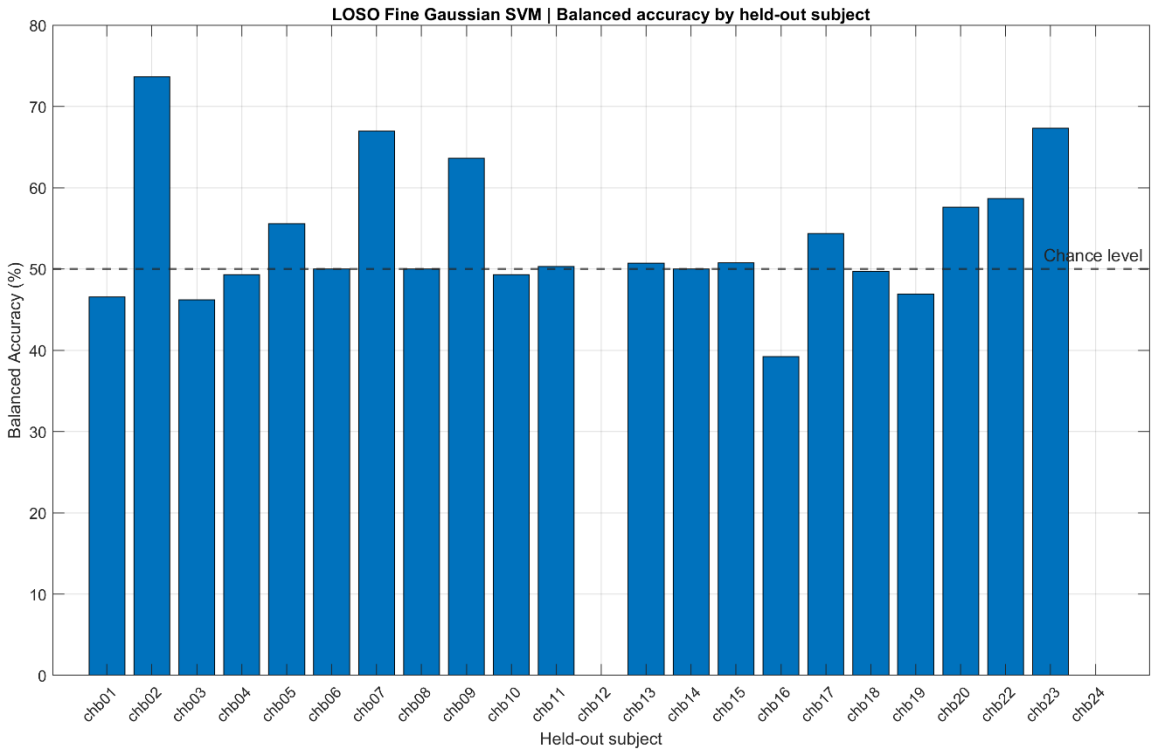


Figure 32. LOSO balanced accuracy across held-out subjects.

Subject-wise balanced accuracy was calculated for the 21 subjects contributing both preictal and interictal blocks, with a mean value of 53.65 ± 8.33%. Subjects chb12 and chb24 contributed only preictal blocks under the adopted temporal criteria; therefore, subject-specific balanced accuracy and ROC-AUC could not be calculated for these subjects, although their observations were retained in the pooled LOSO evaluation. Across all subjects, mean accuracy was 67.67 ± 23.07% and mean preictal sensitivity was 25.99 ± 30.05%, while mean interictal specificity was 81.37 ± 24.72% among subjects for whom it could be calculated. Considerable inter-subject variability was observed, with several subjects showing balanced accuracy close to the 50% chance level.

3.4.2 Graph-Theory-Based Classification

For the graph-theoretical analysis, preliminary model selection was performed using five-fold cross-validation on the balanced dataset and all 189 global graph-theoretical predictors. The best-performing model was a Fine k-Nearest Neighbors (KNN) classifier, which achieved a validation

accuracy of 77.5%. The selected configuration used one nearest neighbor, Euclidean distance, equal distance weighting, predictor standardization, and no principal component analysis.

The selected Fine KNN classifier was subsequently evaluated using the same subject-independent LOSO framework. The full dataset contained 6,751 eligible 5-min blocks from 23 independent subjects, comprising 757 preictal and 5,994 interictal observations. Pooling predictions across all LOSO folds, the classifier correctly identified 3,398 of 5,994 interictal blocks and 346 of 757 preictal blocks. This corresponded to an overall accuracy of 55.46%, a preictal sensitivity of 45.71%, an interictal specificity of 56.69%, and a balanced accuracy of 51.20%.

The corresponding pooled confusion matrix is shown in Figure 33.

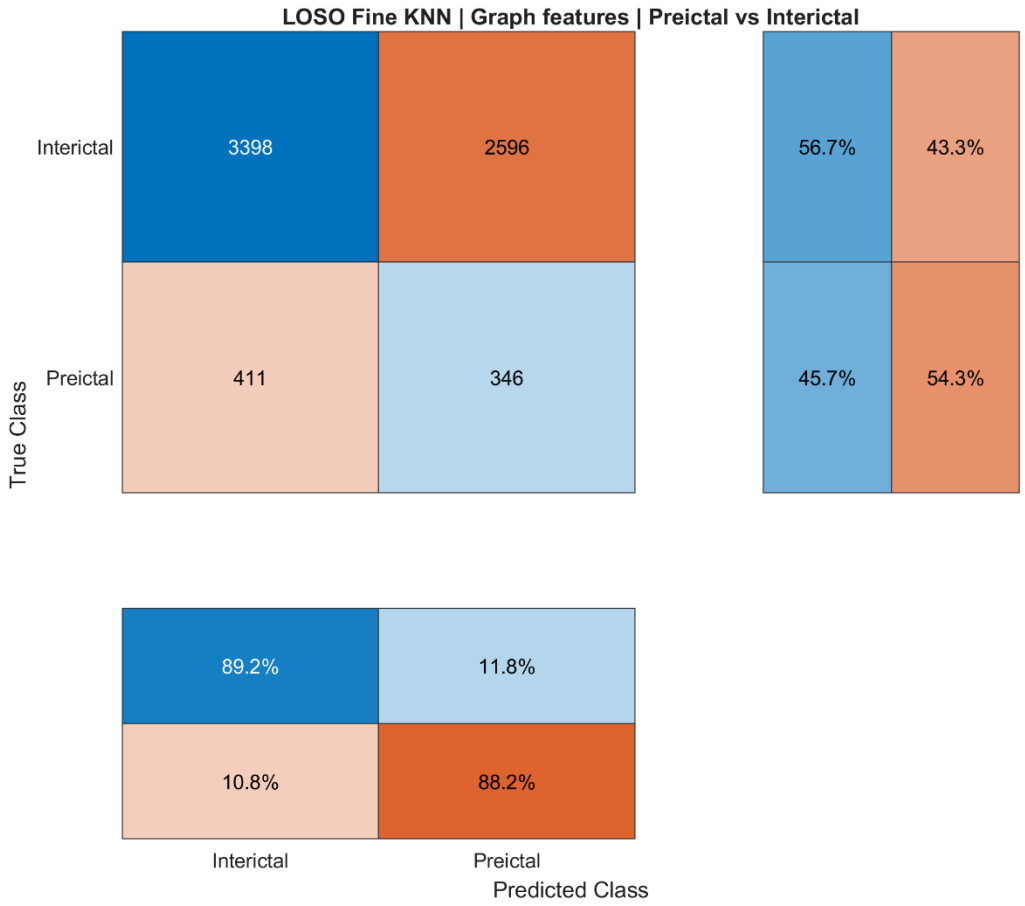


Figure 33. Pooled LOSO confusion matrix for the Fine KNN classifier.

Compared with the functional connectivity classifier, the graph-based classifier showed a more balanced distribution of correct classifications between the two classes. Preictal sensitivity increased

to 45.71%, while interictal specificity decreased to 56.69%. However, the resulting balanced accuracy remained close to the 50% chance level, reaching 51.20%.

The pooled ROC curve for the graph-theoretical classifier is shown in Figure 34. The corresponding ROC-AUC was 0.512, indicating discrimination close to chance level.

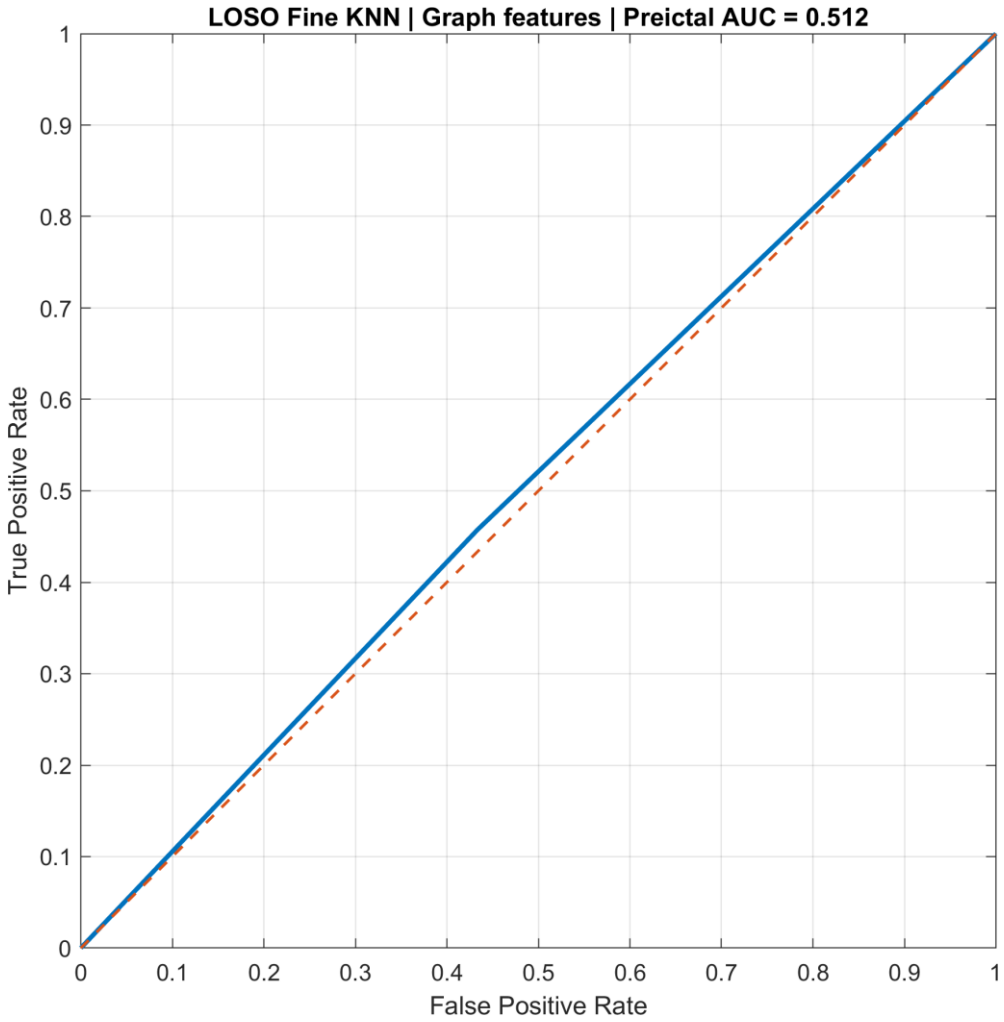


Figure 34. Pooled LOSO ROC curve for the Fine KNN classifier.

The ROC curve remained close to the chance diagonal, consistent with the pooled ROC-AUC of 0.512. As observed for the functional connectivity analysis, performance decreased substantially when moving from preliminary five-fold cross-validation to subject-independent LOSO evaluation, indicating limited generalization of the graph-theoretical feature patterns to previously unseen subjects.

Finally, subject-wise balanced accuracy for the graph-theoretical classifier is reported in Figure 35.

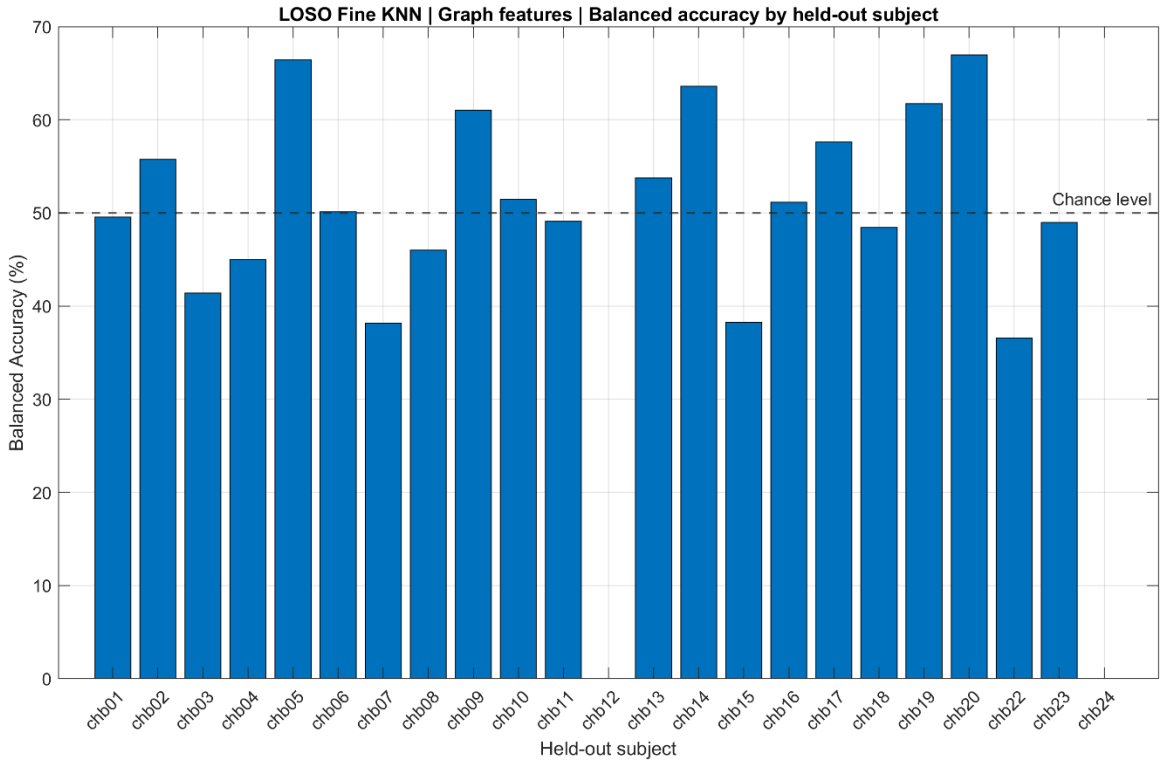


Figure 35. LOSO balanced accuracy across held-out subjects.

Subject-wise balanced accuracy was calculated for the 21 subjects contributing both preictal and interictal blocks, with a mean value of 51.48 ± 9.06%. Subjects chb12 and chb24 contributed only preictal blocks under the adopted temporal criteria; therefore, subject-specific balanced accuracy and ROC-AUC could not be calculated for these subjects, although their observations were retained in the pooled LOSO evaluation. Across all subjects, mean accuracy was 55.95 ± 14.34% and mean preictal sensitivity was 47.90 ± 26.40%, while mean interictal specificity was 55.30 ± 21.84% among subjects for whom it could be calculated. Considerable inter-subject variability was observed, with balanced accuracy ranging from below the 50% chance level to higher values in individual subjects.

4. Discussion

The present study investigated functional brain connectivity and network organization during the transition from interictal to preictal activity in long-term scalp EEG recordings from pediatric patients with drug-resistant epilepsy. A broad set of functional connectivity measures and graph-theoretical metrics was evaluated to determine whether reproducible alterations could be identified during the 30 min preceding seizure onset and whether the extracted features could discriminate preictal from

interictal EEG states. The findings indicate that the preictal period was not characterized by a single, homogeneous pattern of functional connectivity or global network reorganization across subjects. Instead, the most robust differences were localized at the nodal level, while subject-independent classification showed limited generalization to previously unseen patients.

The temporal analysis of functional connectivity did not reveal a consistent progressive trend across the six consecutive 5-min intervals preceding seizure onset. Although fluctuations were observed for individual connectivity measures, frequency bands, and anatomical regions, their direction and magnitude varied across configurations. Some frequency-specific measures, particularly amplitude envelope correlation, showed more evident temporal variability in selected regions; however, these changes did not form a common pattern approaching seizure onset. This suggests that the transition toward the ictal state may not be associated with a uniform increase or decrease in scalp-level functional connectivity. Moreover, connectivity changes preceding seizure onset may not necessarily develop gradually throughout the preictal period. Given the paroxysmal nature of epileptic seizures, relevant functional-connectivity alterations may emerge abruptly or only shortly before seizure onset, making progressive changes difficult to detect over a 30-min preictal interval divided into 5-min segments.

This interpretation was further supported by the direct statistical comparison between preictal and interictal functional connectivity. Across the 32 connectivity configurations, 254 individual connections reached nominal significance before correction for multiple comparisons. However, none remained statistically significant after Benjamini–Hochberg FDR correction. The lowest adjusted q-value was obtained for delta-band PLV, while relatively large effect sizes were observed for selected configurations, including alpha-band AEC. Nevertheless, the absence of FDR-significant connections indicates that these effects were not sufficiently consistent across subjects and derivation pairs to provide robust evidence of a common preictal connectivity alteration. The substantial overlap between the subject-level preictal and interictal distributions further supports this interpretation.

The lack of a uniform functional-connectivity pattern should be interpreted in the context of previous EEG connectivity studies in pediatric epilepsy. Zheng et al. [58], studying infants with West syndrome, reported state-dependent alterations in scalp-EEG functional connectivity across pre-seizure, seizure, and post-seizure periods, with connectivity patterns varying according to frequency band and connectivity estimator. In particular, changes involving beta- and gamma-band networks derived from correlation and wPLI were considered potentially informative of seizure-cycle evolution. Similarly, Davis et al. [61] reported increased EEG connectivity preceding the onset of epileptic spasms in infants with tuberous sclerosis complex. These findings support the existence of

connectivity alterations associated with seizure development, but they do not necessarily imply that a common connectivity pattern should be detectable across a heterogeneous pediatric drug-resistant epilepsy population. The present study included patients with different epilepsy characteristics and analyzed several connectivity estimators and frequency bands, and no individual connection remained significant after FDR correction. Differences in epilepsy type, seizure onset zone, age, medication, underlying pathology, methodological approach, and definition of the preictal period may therefore contribute to the discrepancy between studies. Rather than indicating an absence of preictal network changes, the present findings suggest that such alterations may be strongly dependent on the individual patient, frequency range, and connectivity measure and may consequently be difficult to identify as a single group-level pattern.

Graph-theoretical analysis provided a complementary perspective by examining whether the observed functional interactions were accompanied by changes in network topology. At the global level, none of the 189 comparisons remained significant after FDR correction. Two nominally significant differences were observed for algebraic connectivity, one derived from broadband mutual information and the other from alpha-band coherence, both showing lower values during the preictal condition. However, neither difference survived correction for multiple comparisons. The remaining global measures, including mean strength, weighted clustering, global efficiency, characteristic path length, mean local efficiency, link density, S-metric, and graph energy, showed no statistically significant differences after FDR correction. These results suggest that the preictal state was not associated with a robust and widespread reorganization of whole-network topology detectable with the global measures considered in this study.

A different pattern emerged from the nodal analysis. Three comparisons involving betweenness centrality remained significant after FDR correction, whereas no FDR-significant differences were observed for node strength, weighted clustering, local efficiency, or closeness centrality. Betweenness centrality reflects the extent to which a node lies along shortest communication paths within a network and therefore provides information about its potential role in mediating network-wide interactions. The selective involvement of this metric suggests that preictal alterations may affect the relative network role of specific EEG derivations without producing a corresponding global reorganization of the network.

Two of the three significant betweenness-centrality comparisons showed lower values during the preictal condition. The strongest effect was observed for delta-band PLV at T7–FT9, followed by a significant reduction for gamma-band wPLI at F8–T8. In contrast, beta-band wPLI at FP2–F8 showed increased preictal betweenness centrality. The coexistence of both decreases and increases indicates

that the preictal transition cannot be described simply as a generalized loss or gain of network integration. Rather, the findings point toward node-specific and frequency-dependent modifications in the relative contribution of specific EEG derivations to network communication. Importantly, these effects were restricted to particular combinations of connectivity measure, frequency band, and EEG derivation and should therefore not be interpreted as evidence of a generalized topological biomarker.

The contrast between the global and nodal findings is particularly relevant. While global metrics did not identify significant differences after multiple-comparison correction, selected nodal betweenness-centrality measures did. This suggests that node-specific changes in network topology may occur without being sufficiently extensive or consistent across the network to alter whole-network summary measures. Such a result is compatible with the concept of epilepsy as a network disorder in which specific regions or pathways may change their functional role during the transition toward seizure onset. At the same time, scalp EEG provides an indirect and spatially limited representation of the underlying cortical networks, and each bipolar derivation reflects electrical activity generated by multiple neural sources. The nodal findings should therefore be interpreted as changes in EEG-derived network organization rather than direct localization of specific cortical structures.

The distinction between global and more spatially restricted network alterations is also relevant when the present findings are compared with previous graph-theoretical studies in pediatric epilepsy. Sargolzaei et al. [59] demonstrated that graph-theoretical properties derived from scalp-EEG functional connectivity networks can distinguish pediatric patients with epilepsy from healthy controls, supporting the sensitivity of network topology to epilepsy-related alterations. Zheng et al. [58] similarly reported changes in graph-theoretical measures across different phases of the seizure cycle in infants with West syndrome. More recently, Liu et al. [63] examined both global and multi-partition local networks in West syndrome, highlighting the potential relevance of local network alterations in characterizing epilepsy-related changes. These observations are compatible with the present finding that significant effects emerged at the nodal rather than global level. However, direct comparison remains limited because previous studies investigated different clinical populations and experimental contrasts, including epilepsy versus healthy controls, different phases of the seizure cycle, or treatment-related changes, whereas the present analysis specifically compared preictal and interictal activity within pediatric patients with drug-resistant epilepsy.

The classification analyses further demonstrated the importance of evaluating whether the identified quantitative patterns generalize across subjects. During preliminary model selection using conventional five-fold cross-validation on balanced datasets, functional connectivity features produced a validation accuracy of 84.0% with a Fine Gaussian SVM, whereas global graph-

theoretical features produced an accuracy of 77.5% with a Fine KNN classifier. These results initially suggested that both feature sets contained information capable of separating preictal and interictal blocks within the available dataset.

However, performance decreased markedly when the selected models were evaluated using subject-independent LOSO cross-validation. For functional connectivity, the Fine Gaussian SVM achieved a pooled balanced accuracy of 54.22% and a ROC-AUC of 0.533. Although the overall accuracy remained relatively high at 79.28%, this value was strongly influenced by the class imbalance in the full dataset. The classifier correctly identified 86.52% of interictal blocks but only 21.93% of preictal blocks. Therefore, the high overall accuracy did not correspond to effective discrimination of the clinically relevant preictal state.

The graph-theoretical classifier showed a different balance between the two classes but similarly limited overall discrimination. Under LOSO evaluation, the Fine KNN classifier achieved a preictal sensitivity of 45.71%, an interictal specificity of 56.69%, a balanced accuracy of 51.20%, and a ROC-AUC of 0.512. Thus, although preictal sensitivity was higher than that obtained with the functional-connectivity classifier, overall discrimination remained close to chance level. The subject-wise analyses also demonstrated substantial variability in classification performance for both feature sets.

The marked difference between preliminary five-fold cross-validation and LOSO performance is an important finding of the present study. Conventional random cross-validation allows blocks originating from the same subject to be distributed between training and validation folds. Because EEG characteristics and connectivity patterns can be strongly subject-specific, a classifier may partially exploit individual characteristics rather than features that generalize across patients. In contrast, LOSO evaluation requires the model to classify data from a subject that was completely absent during training and therefore provides a more stringent assessment of inter-subject generalization. The reduction in balanced accuracy and ROC-AUC under LOSO suggests that a substantial component of the discrimination observed during preliminary model selection was subject-dependent.

The limited subject-independent performance observed in the present study is particularly relevant when compared with previous seizure-prediction studies based on EEG connectivity and network features. Chen et al. [66] reported high predictive performance on the CHB-MIT dataset using a seizure-prediction framework based on functional connectivity, while Zhong et al. [68], also using CHB-MIT recordings, obtained high classification performance by combining temporal, spectral, entropy, and brain-network features. These findings demonstrate that EEG connectivity and network-derived information can contribute to the discrimination of preictal activity. However, direct

numerical comparison with the present results is difficult because the studies differ in feature construction, preictal definitions, data selection, classification algorithms, and validation procedures. In the present study, the marked reduction in performance from conventional five-fold cross-validation to LOSO evaluation indicates that the ability of the selected features to generalize to completely unseen subjects was limited. This observation highlights the importance of subject-independent validation when assessing the potential generalizability of EEG-based preictal biomarkers.

More broadly, the clinical relevance of EEG functional connectivity has also been demonstrated in pediatric pharmacoresistant epilepsy for predicting response to vagus nerve stimulation [60] and in drug-resistant epilepsy for machine-learning-based localization of the epileptogenic zone using source-level connectivity [67]. Although these studies addressed clinical objectives different from preictal–interictal discrimination, they further support the potential value of connectivity-derived features while also illustrating the diversity of applications, methodological approaches, and prediction targets found in the literature.

These classification findings are also consistent with the statistical analyses. Pairwise functional connectivity did not show FDR-significant group-level differences, and global graph metrics likewise showed no significant differences after correction. Although the nodal analysis identified three FDR-significant differences in betweenness centrality, nodal metrics were not included among the predictors used for graph-based classification, which consisted exclusively of the 189 global graph features. Global graph metrics summarize properties of the network as a whole and therefore do not retain the node-specific information captured by nodal measures. Consequently, the classifier did not directly exploit the specific betweenness-centrality features that showed significant preictal–interictal differences in the statistical analysis. The limited performance of the graph-based classifier therefore does not contradict the nodal findings, as the two analyses evaluated different levels of network organization: classification assessed whether whole-network characteristics generalized to unseen subjects, whereas the nodal statistical analysis identified condition-related differences restricted to specific EEG derivations and connectivity configurations.

Several methodological factors should be considered when interpreting these findings. First, the CHB-MIT database includes a heterogeneous pediatric population with differences in age, epilepsy characteristics, seizure frequency, and recording duration. Such variability is clinically representative but can reduce the consistency of group-level electrophysiological patterns. Second, the amount of available preictal and interictal data was inherently unbalanced. Although balancing was used during preliminary classifier selection and training-set undersampling was performed within the LOSO

procedure, the held-out test subjects retained their natural class distribution, resulting in substantially more interictal than preictal observations in the pooled evaluation.

Third, functional connectivity was estimated from 4-s scalp EEG windows. This window duration provides temporal resolution for tracking dynamic changes but may limit the stability of some connectivity estimators, particularly at lower frequencies. Moreover, scalp EEG is affected by volume conduction, field spread, reference configuration, and limited spatial resolution [7]. The use of multiple complementary connectivity estimators partly addresses these limitations, particularly through phase-lag-based measures such as PLI and wPLI, but these factors cannot be completely eliminated.

Fourth, network construction influences graph-theoretical results. The present analysis used weighted networks without arbitrary proportional thresholding, thereby preserving the available connectivity information. However, the resulting network topology depends on the underlying connectivity estimator and normalization procedure, as these methodological choices determine the weights assigned to the network edges and can consequently affect the derived graph metrics. Therefore, the observed graph-theoretical findings should be interpreted in relation to the specific network-construction procedures adopted in this study rather than as invariant properties of the underlying brain networks. In addition, only a selected subset of non-negative, undirected connectivity configurations was considered suitable for graph construction. Consequently, the graph results characterize specific representations of functional networks rather than all possible network formulations.

Finally, the present analysis investigated a fixed 30-min preictal interval and defined interictal activity as occurring at least 4 h from any seizure. These definitions provided consistent temporal criteria across subjects, but the duration and electrophysiological expression of the preictal state may vary between patients and seizures. A fixed group-level definition may therefore combine periods with different physiological relevance. Future studies could investigate patient-specific preictal horizons, seizure-specific analyses, and models explicitly designed to account for inter-subject variability.

Collectively, the results suggest that the transition toward seizure onset in pediatric drug-resistant epilepsy is characterized more clearly by selected nodal alterations in network topology than by a uniform change in pairwise functional connectivity or whole-network organization. The three FDR-significant betweenness-centrality findings provide evidence that the functional role of specific EEG derivations may change during the preictal period. However, the absence of significant pairwise functional-connectivity and global graph-theoretical effects, together with the near-chance subject-independent classification performance, indicates that these alterations are not sufficiently

homogeneous across patients to constitute a robust generalized preictal biomarker based on the present analysis. Future work should therefore focus on patient-specific or adaptive approaches, larger pediatric cohorts, and independent validation to determine whether individualized connectivity and network patterns can provide more reliable characterization of the transition toward seizure onset.

Conclusion

The aim of this thesis was to investigate whether functional brain connectivity and network organization derived from long-term scalp EEG could reveal changes preceding seizure onset in pediatric patients with drug-resistant epilepsy. To address this objective, preictal and interictal EEG activity from the CHB-MIT database was analyzed using multiple functional-connectivity estimators, graph-theoretical measures, statistical comparisons, and machine-learning classification.

The results showed that the transition toward seizure onset was not characterized by a single, consistent pattern of functional connectivity across the analyzed population. Although several individual connections showed nominal preictal–interictal differences, none remained significant after correction for multiple comparisons. Furthermore, the temporal analysis of the 30-min preictal period did not reveal a consistent pattern of connectivity changes across the intervals approaching seizure onset.

At the network level, global graph-theoretical measures similarly showed no significant differences after correction, suggesting that the preictal state was not associated with a robust whole-network reorganization shared across subjects. Nevertheless, the nodal analysis identified three FDR-significant differences in betweenness centrality. Two comparisons showed reduced preictal betweenness centrality, while one showed an increase. These findings suggest that alterations preceding seizure onset may preferentially involve the network role of specific EEG derivations rather than widespread changes in global topology. The presence of effects across different frequency bands and connectivity measures further suggests that these alterations are frequency- and measure-dependent.

The classification analysis provided an additional assessment of the generalizability of the extracted features. Although preliminary five-fold cross-validation produced relatively high classification accuracies, performance decreased substantially under the more stringent LOSO evaluation. Functional-connectivity features achieved a balanced accuracy of 54.22% and a ROC-AUC of 0.533, while global graph-theoretical features achieved a balanced accuracy of 51.20% and a ROC-AUC of 0.512. These findings indicate that patterns capable of distinguishing preictal and interictal activity within the available dataset did not generalize effectively to previously unseen subjects.

Therefore, the results of this thesis highlight the complexity and heterogeneity of preictal brain dynamics in pediatric drug-resistant epilepsy. The absence of consistent group-level functional-connectivity and global network alterations, together with the localized nodal findings and limited

LOSO performance, suggests that a universal preictal network signature may be difficult to identify from scalp EEG using a population-level approach. At the same time, the significant nodal alterations indicate that network-based analysis can capture localized modifications that are not apparent from global measures alone.

Future studies could extend this work by including larger and more homogeneous pediatric populations, investigating patient- and seizure-specific preictal intervals, and integrating functional connectivity with additional quantitative EEG features. In particular, individualized or adaptive models may be better suited to account for the substantial inter-subject variability observed in the present analysis. Further validation on independent datasets will be necessary to determine whether these approaches can contribute to a more reliable characterization of the electrophysiological transition toward seizure onset.

Appendix

A structured literature search was conducted to identify scientific studies related to long-term EEG monitoring in pediatric patients with drug-resistant epilepsy. The search was performed using two major biomedical and multidisciplinary databases: PubMed and Scopus. The query used for the systematic review was: "*(pediatric OR children) AND epilep* AND (long-term EEG monitoring) AND (drug-resistant OR intractable)",* designed to retrieve specific studies from the scientific literature. To ensure the relevance and quality of the selected studies, the following filters were applied:

- Studies involving pediatric populations
- Articles published in the last 10 years
- Articles written in English
- Studies involving human subjects

The search yielded a total of 55 records. Only studies involving pediatric patients with drug-resistant or intractable epilepsy and using long-term EEG monitoring were retained.

The study selection process was carried out in multiple steps:

1. The query was applied to PubMed and Scopus, resulting in 55 records.
2. After duplicate removal, articles were screened to assess their relevance to the review topic.

3. Potentially eligible studies were reviewed in full text. Only the ones involving pediatric patients with drug-resistant or intractable epilepsy and using long-term EEG monitoring were retained.

Following the screening and eligibility assessment, 14 studies met all inclusion criteria and were included in the final review. For each selected study, relevant information including patient characteristics, EEG methodology, study objectives, and main findings was systematically extracted and organized into a structured table (Table 9) to facilitate comparison across studies and identify common patterns in the clinical application of long-term EEG monitoring.

Table 9. Summary of the reviewed studies.

Reference	Database	Authors & year	Title	N. patients	EEG type	N. of channels	Aim	Main findings
[46]	PubMed	Wiegand et al., 2022	EEG-Findings during long-term treatment with everolimus in TSC-associated and therapy-resistant epilepsies in children	13	72h video-EEG	≥32 channels, 10–10 system	To investigate longitudinal EEG changes during everolimus treatment in children with TSC-associated drug-resistant epilepsy.	Reduction of seizures and interictal discharges, especially during sleep
[45]	PubMed	Wang et al., 2023	Safety and efficacy of rapid withdrawal of antiseizure medications during long-term video-EEG monitoring in children with drug-resistant epilepsy	80	Long-term video-EEG monitoring	32-channel EEG system; 19 standard 10–20 electrodes	To evaluate the safety and efficacy of rapid antiseizure-medication withdrawal during long-term video-EEG monitoring in children with drug-resistant epilepsy.	Seizures successfully induced in 90% of patients; useful for obtaining ictal EEG
[47]	PubMed	Sierra-Marcos et al., 2017	Functional surgery in pediatric drug-resistant posterior cortex epilepsy: electro-clinical findings and outcomes	55	Long-term video-EEG (EMU)	10–20 system (+ 10–10 if necessary)	To characterize electroclinical and imaging findings in pediatric posterior cortex epilepsy and identify factors associated with surgical and cognitive outcomes.	EEG contributes to localization of epileptogenic zone and surgical outcome prediction
[54]	PubMed	Zavala-Yoe et al., 2016	Entropy measures to study and model long term simultaneous evolution of children in Doose and Lennox–Gastaut syndromes	5 subjects: 4 patients with DR-MF-EE and 1 normal control	Long-term scalp EEG records accumulated over years; sleep-deprived EEG in affected patients	19 scalp EEG channels, 10–20 system; 200 Hz sampling frequency	To develop entropy-based measures for objectively assessing the long-term EEG evolution of children with Doose and Lennox–Gastaut syndromes.	Entropy-based measures (MSE, BMSE, DBMSE) allowed objective comparison of long-term EEG, identification of the most affected year and brain region/channel, with results consistent with neurologists' conclusions
[48]	PubMed	Menderes et al., 2025	Evaluation of lateralization and localization value of hand postures in Pediatric Epilepsy	56 patients (91 seizures analyzed)	Long-term video-EEG monitoring (VEMU)	Not reported	To evaluate the localization and lateralization value of ictal hand postures in children with epilepsy.	Specific ictal hand postures were associated with seizure localization and lateralization; fist posture was linked to frontal lobe seizures, TUF to temporal lobe seizures, supporting presurgical evaluation.
[49]	PubMed	Liu et al., 2025	Surgical outcomes and motor function in pediatric peri-Rolandic epilepsy: A single center's	152	Long-term video-EEG (VEEG); invasive EEG monitoring	Not reported	To investigate lesion distribution, surgical outcomes, and the relationship between lesion location and postoperative	Surgery achieved seizure freedom in 80% of patients; lesion location influenced postoperative motor deficits but not seizure outcome.

			experience with 152 cases		in selected cases		motor function in pediatric peri-Rolandic epilepsy.	
[50]	PubMed	Erdemir et al., 2021	Surgical candidates in children with epileptic spasms can be selected without invasive monitoring: A report of 70 cases	70	Long-term video-EEG monitoring (presurgical evaluation)	Not reported	To evaluate surgical outcomes and prognostic factors in children with drug-resistant epileptic spasms selected for surgery without intracranial EEG monitoring.	Favorable surgical outcomes were achieved without invasive EEG monitoring; 60% of patients were seizure-free at long-term follow-up.
[51]	PubMed	Benifla et al., 2017	Temporal lobe surgery for intractable epilepsy in children: What to do with the hippocampus?	22	Prolonged video-EEG monitoring + invasive EEG monitoring (when required)	64-channel subdural grid + depth electrodes (in invasive monitoring cases)	To investigate methods for determining hippocampal involvement in the epileptogenic zone and outcomes of hippocampal-sparing surgery in children with temporal lobe epilepsy.	Hippocampal sparing achieved excellent seizure outcomes; 94% of patients without hippocampectomy were seizure-free
[53]	PubMed	Di Micco et al., 2024	Seizure and movement disorder in CACNA1E developmental and epileptic encephalopathy: Two sides of the same coin or same side of two different coins?	1	48-h long-term video-EEG monitoring	Not reported	To characterize seizures and movement disorders in a child with CACNA1E developmental and epileptic encephalopathy using prolonged video-EEG monitoring.	Long-term video-EEG revealed that subtle dyskinetic episodes previously considered a movement disorder were actually focal seizures, supporting its role in the differential diagnosis between epileptic and non-epileptic manifestations.
[52]	Scopus	Tsai et al., 2026	Seizure recurrences after temporal lobe epilepsy surgery in childhood and adolescence: predictive factors, patterns of recurrence, and long-term outcomes	61	Scalp video-EEG monitoring; invasive EEG in selected patients	Not reported	To identify predictors of seizure recurrence and characterize recurrence patterns, treatment responses, and long-term outcomes after temporal lobe epilepsy surgery in children and adolescents.	Seizure recurrence occurred in 55.7% of patients. Acute postoperative seizures were an independent predictor of early recurrence, while late recurrences showed a greater response to medical treatment. At the last follow-up, 68% of patients were seizure-free.
[56]	Scopus	Irandoost et al., 2023	Non-invasive Electrical Source Imaging for Localizing Epileptiform Discharges in Children with Focal Epilepsy Based on Developing Country's Limitations	7	Long-term video-EEG monitoring (≥24 h)	19 scalp electrodes (10–20 system)	To evaluate non-invasive electrical source imaging for localization of epileptiform activity in children with focal epilepsy.	ESI localized the seizure onset zone in 71% of cases and improved presurgical localization
[57]	Scopus	Hartnett et al., 2022	Responsive neurostimulation device therapy in pediatric patients with complex medically refractory epilepsy	8	Long-term video-EEG + invasive monitoring (SEEG/SDG) for presurgical evaluation	Stereo-Electroencephalography (SEEG): 44–192 contacts; Subdural Grid (SDG): 64–92 contacts	To describe the initial clinical experience with responsive neurostimulation in pediatric patients with drug-resistant epilepsy.	RNS therapy achieved >50% seizure reduction in all patients after EEG-guided target localization
[55]	Scopus	Rukhsar et al., 2019	Patient-Specific Epileptic Seizure Prediction in Long-Term Scalp EEG Signal Using Multivariate Statistical Process Control	10 (selected from CHB-MIT; dataset originally includes 24 patients)	Long-term scalp EEG (CHB-MIT database)	18 channels (selected consistent bipolar montage channels)	To develop a patient-specific method for predicting epileptic seizures from long-term scalp EEG using multivariate statistical process control.	The proposed MSPC-based method predicts seizures from long-term EEG with high sensitivity (~88.9%) and reduced false positive rate (~0.39/h).
[44]	Scopus	Ghazavi et al., 2017	Long-term video-EEG monitoring findings in children and adolescents with intractable epilepsy	43 patients	Long-term video-EEG monitoring (LTM)	Not reported	To evaluate the clinical contribution of long-term video-EEG monitoring in children and adolescents with intractable epilepsy,	Identified surgical candidates and treatment changes

							particularly for presurgical assessment.	

References

[1] Saladin KS. Anatomia umana. 2nd Italian ed. Padova: Piccin Nuova Libraria S.p.A.; 2017.

[2] Kandel ER, Koester JD, Mack SH, Siegelbaum SA. Principles of Neural Science. 6th ed. New York: McGraw-Hill; 2021.

[3] Purves D, Augustine GJ, Fitzpatrick D, et al. Neuroscience. 6th ed. New York: Oxford University Press; 2018.

[4] Parent A, Carpenter MB. Carpenter's Human Neuroanatomy. Baltimore: Williams & Wilkins; 1995.

[5] Martini FH, Tallitsch RB, Nath JL. Anatomia umana. 7a ed. Napoli: EdiSES; 2019.

[6] Niedermeyer E, da Silva FL. Electroencephalography: Basic Principles, Clinical Applications, and Related Fields. 6th ed. Philadelphia: Lippincott Williams & Wilkins; 2011.

[7] Nunez PL, Srinivasan R. Electric Fields of the Brain: The Neurophysics of EEG. 2nd ed. Oxford: Oxford University Press; 2006.

[8] American Electroencephalographic Society. Guideline seven: A proposal for standard montages to be used in clinical EEG. Journal of Clinical Neurophysiology. 1994;11(1):30–36. doi:10.1097/00004691-199401000-00008.

[9] Sanei S, Chambers JA. EEG Signal Processing. Chichester: Wiley; 2007.

[10] Jasper HH. Report of the committee on methods of clinical examination in electroencephalography. Electroencephalography and Clinical Neurophysiology. 1958;10(2):370–375. doi:10.1016/0013-4694(58)90053-1.

[11] Acharya JN, Hani A, Cheek J, Thirumala P, Tsuchida TN. American Clinical Neurophysiology Society guideline 2: Guidelines for standard electrode position nomenclature. Journal of Clinical Neurophysiology. 2016;33(4):308–311. doi:10.1097/WNP.0000000000000316.

[12] Chatterjee R, Datta A, Sanyal DK. Ensemble learning approach to motor-imagery EEG signal classification. In: Machine Learning in Bio-Signal Analysis and Diagnostic Imaging. Preprint; 2019.

[13] Buzsáki G. Rhythms of the Brain. New York: Oxford University Press; 2006.

[14] Tatum WO. Handbook of EEG Interpretation. 2nd ed. New York: Demos Medical Publishing; 2014.

[15] Jiang X, Bian GB, Tian Z. Removal of artifacts from EEG signals: A review. Sensors. 2019;19(5):987. doi:10.3390/s19050987.

[16] Chen X, Xu X, Liu A, Lee S, Chen X, Zhang X, et al. Removal of muscle artifacts from the EEG: A review and recommendations. IEEE Sensors Journal. 2019;19(14):5353–5368. doi:10.1109/JSEN.2019.2906572.

[17] Dora M, Holcman D. Adaptive single-channel EEG artifact removal with applications to clinical monitoring. IEEE Transactions on Neural Systems and Rehabilitation Engineering. 2022;30:286–295. doi:10.1109/TNSRE.2022.3147072.

[18] Singh AK, Krishnan S. Trends in EEG signal feature extraction applications. Front Artif Intell. 2023 Jan 25;5:1072801. doi:10.3389/frai.2022.1072801. PMID: 36760718; PMCID: PMC9905640.

[19] Savadi S. A comprehensive review of feature extraction and classification techniques in EEG signal analysis. International Journal of Computational Engineering Research. 2025;15(6):1–8.

[20] Fisher RS, Acevedo C, Arzimanoglou A, Bogacz A, Cross JH, Elger CE, et al. ILAE official report: a practical clinical definition of epilepsy. Epilepsia. 2014;55(4):475–482. doi:10.1111/epi.12550.

[21] World Health Organization. Epilepsy fact sheet [Internet]. 2024 [cited 2024 Sep 28]. Available from: https://www.who.int/news-room/fact-sheets/detail/epilepsy.

[22] Neligan A, Adan G, Nevitt SJ, Pullen A, Sander JW, Bonnett L, et al. Prognosis of adults and children following a first unprovoked seizure. Cochrane Database of Systematic Reviews. 2023;1(1):CD013847. doi:10.1002/14651858.CD013847.pub2.

[23] Newton CR, Garcia HH. Epilepsy in poor regions of the world. The Lancet. 2012;380(9848):1193–1201. doi:10.1016/S0140-6736(12)61381-6.

[24] Scheffer IE, Berkovic S, Capovilla G, Connolly MB, French J, Guilhoto L, et al. ILAE classification of the epilepsies: Position paper of the ILAE Commission for Classification and Terminology. Epilepsia. 2017;58(4):512–521. doi:10.1111/epi.13709.

[25] Pandolfo M. Genetics of epilepsy. Seminars in Neurology. 2011;31(5):506–518. doi:10.1055/s-0031-1299789.

[26] Bhalla D, Godet B, Druet-Cabanac M, Preux PM. Etiologies of epilepsy: a comprehensive review. Expert Review of Neurotherapeutics. 2011;11(6):861–876. doi:10.1586/ern.11.51.

[27] Fisher RS, Cross JH, French JA, et al. Operational classification of seizure types by the International League Against Epilepsy. Epilepsia. 2017;58(4):522–530.

[28] Blumenfeld H. Cellular and network mechanisms of spike-wave seizures. Epilepsia. 2005;46(Suppl 9):21–33. doi:10.1111/j.1528-1167.2005.00311.x.

[29] Le Van Quyen M, Navarro V, Martinerie J, Baulac M, Varela FJ. Toward a neurodynamical understanding of ictogenesis. Epilepsia. 2003;44(Suppl 12):30–43. doi:10.1111/j.0013-9580.2003.12007.x.

[30] Pitkänen A, Engel J. Past and present definitions of epileptogenesis and its biomarkers. Neurotherapeutics. 2014;11(2):231–241. doi:10.1007/s13311-014-0257-2.

[31] Engel J, Pedley TA, eds. Epilepsy: A Comprehensive Textbook. 2nd ed. Philadelphia: Wolters Kluwer Health/Lippincott Williams & Wilkins; 2008.

[32] Ropper AH, Samuels MA, Klein JP, Prasad S. Epilepsy and other seizure disorders. In: Adams and Victor's Principles of Neurology. 12th ed. New York: McGraw Hill; 2023. Chapter 15.

[33] National Institute for Health and Care Excellence. Epilepsies in children, young people and adults. London: NICE; 2022.

[34] Pillai J, Sperling MR. Interictal EEG and the diagnosis of epilepsy. Epilepsia. 2006;47(Suppl 1):14–22. doi:10.1111/j.1528-1167.2006.00654.x.

[35] Holmes GL, Lombroso CT. Prognostic value of background patterns in the neonatal EEG. Journal of Clinical Neurophysiology. 1993;10(3):323–352.

[36] Kuratani J, Pearl PL, Sullivan L, Riel-Romero RMS, Cheek J, Stecker M, et al. American Clinical Neurophysiology Society guideline 5: Minimum technical standards for pediatric electroencephalography. Journal of Clinical Neurophysiology. 2016;33(4):320–325. doi:10.1097/WNP.0000000000000317.

[37] Minardi C, Minacapelli R, Valastro P, Vasile F, Pitino S, Pavone P, et al. Epilepsy in children: From diagnosis to treatment with focus on emergency. Children (Basel). 2019;6(5):70. doi:10.3390/children6050070.

[38] Saad K, Eldaly EH, Abdelall HM, Abdelgabaar NM, Zaki DM, Dailah HG, et al. Contemporary insights into intractable epilepsy in children. Children (Basel). 2023;10(3):510. doi:10.3390/children10030510.

[39] Chiarion G, Sparacino L, Antonacci Y, Faes L, Mesin L. Connectivity analysis in EEG data: A tutorial review of the state of the art and emerging trends. Bioengineering (Basel). 2023;10(3):372. doi:10.3390/bioengineering10030372.

[40] Khaleghi N, Hashemi S, Peivandi M, Zafarmandi Ardabili S, Behjati M, Sheykhivand S, et al. EEG-based functional connectivity analysis of brain abnormalities: A systematic review study. Inform Med Unlocked. 2024;47:101476. doi:10.1016/j.imu.2024.101476.

[41] Ismail LE, Karwowski W. A graph theory-based modeling of functional brain connectivity based on EEG: A systematic review in the context of neuroergonomics. IEEE Access. 2020;8:155103–155135. doi:10.1109/ACCESS.2020.3018995.

[42] De Vico Fallani F, da Fontoura Costa L, Rodriguez FA, Astolfi L, Vecchiato G, Toppi J, et al. A graph-theoretical approach in brain functional networks: Possible implications in EEG studies. Nonlinear Biomed Phys. 2010;4(Suppl 1):S8. doi:10.1186/1753-4631-4-S1-S8.

[43] Hatlestad-Hall C, Bruña R, Liljeström M, Renvall H, Heuser K, Taubøll E, et al. Reliable evaluation of functional connectivity and graph theory measures in source-level EEG: How many electrodes are enough? Clin Neurophysiol. 2023;150:1–16. doi:10.1016/j.clinph.2023.03.002.

[44] Ghazavi Y, Asayesh Zarchi E, Taheri T, Safiabadi M, Rahimian E, Amirsalari S. Long-term video-EEG monitoring findings in children and adolescents with intractable epilepsy. Iran J Child Neurol. 2017;11(4):23–31.

[45] Wang S, Wang W, Yu G, Wan L, Fan Y, Wang H, et al. Safety and efficacy of rapid withdrawal of antiseizure medications during long-term video-electroencephalogram monitoring in children with drug-resistant epilepsy: A retrospective study. Epilepsia Open. 2023;8(2):313–319. doi:10.1002/epi4.12680.

[46] Wiegand G, Japaridze N, Gröning K, Stephani U, Kadish NE. EEG-findings during long-term treatment with everolimus in TSC-associated and therapy-resistant epilepsies in children. Seizure. 2022;103:101–107. doi:10.1016/j.seizure.2022.10.022.

[47] Sierra-Marcos A, Fournier-del Castillo MC, Álvarez-Linera J, Budke M, García-Fernández M, Pérez-Jiménez MA. Functional surgery in pediatric drug-resistant posterior cortex epilepsy: Electro-

clinical findings, cognitive and seizure outcome. Seizure. 2017;52:46–52. doi:10.1016/j.seizure.2017.09.013.

[48] Menderes D, Hirfanoğlu T, Serdaroğlu E, Serdaroğlu A, Arhan E. Evaluation of lateralization and localization value of hand postures in pediatric epilepsy. Seizure. 2025;127:71–76. doi:10.1016/j.seizure.2025.03.005.

[49] Liu Q, Zhu R, Wang Y, Yu H, Liu C, Sun Y, et al. Surgical outcomes and motor function in pediatric peri-Rolandic epilepsy: A single center's experience with 152 cases. Epilepsia. 2025;66(7):2190–2197. doi:10.1111/epi.18368.

[50] Erdemir G, Pestana-Knight E, Honomichl R, Thompson NR, Lachhwani D, Kotagal P, et al. Surgical candidates in children with epileptic spasms can be selected without invasive monitoring: A report of 70 cases. Epilepsy Res. 2021;176:106731. doi:10.1016/j.eplepsyres.2021.106731.

[51] Benifla M, Bennet-Back O, Shorer Z, Noyman I, Bar-Yosef R, Ekstein D. Temporal lobe surgery for intractable epilepsy in children: What to do with the hippocampus? Seizure. 2017;52:81–88. doi:10.1016/j.seizure.2017.09.020.

[52] Tsai MC, Starnes K, Fine AL, Nickels KC, Wirrell EC, Van Gompel JJ, et al. Seizure recurrences after temporal lobe epilepsy surgery in childhood and adolescence: Predictive factors, patterns of recurrence, and long-term outcomes. Epilepsy Res. 2026;221:107732. doi:10.1016/j.eplepsyres.2026.107732.

[53] Di Micco V, Affronte L, Khinchi MS, Rønde G, Miranda MJ, Hammer TB, et al. Seizure and movement disorder in CACNA1E developmental and epileptic encephalopathy: Two sides of the same coin or same side of two different coins? Epileptic Disord. 2024;26(4):520–526. doi:10.1002/epd2.20242.

[54] Zavala-Yoe R, Ramirez-Mendoza RA, Cordero LM. Entropy measures to study and model long term simultaneous evolution of children in Doose and Lennox-Gastaut syndromes. J Integr Neurosci. 2016;15(2):205–221. doi:10.1142/S0219635216500138.

[55] Rukhsar S, Khan YU, Farooq O, Sarfraz M, Khan AT. Patient-specific epileptic seizure prediction in long-term scalp EEG signal using multivariate statistical process control. IRBM. 2019;40(6):320–331. doi:10.1016/j.irbm.2019.08.004.

[56] Ahmadzadeh Irandoost S, Badv RS, Oghabian MA, Yarali B, Azizi Malamiri R, Hashemi H, et al. Non-invasive electrical source imaging for localizing epileptiform discharges in children with

focal epilepsy based on developing country's limitations. Iran J Pediatr. 2023;33(2):e121981. doi:10.5812/ijp-121981.

[57] Hartnett SM, Greiner HM, Arya R, Tenney JR, Aungaroon G, Holland K, et al. Responsive neurostimulation device therapy in pediatric patients with complex medically refractory epilepsy. J Neurosurg Pediatr. 2022;30(5):499–506. doi:10.3171/2022.7.PEDS2281.

[58] Zheng R, Feng Y, Wang T, Cao J, Wu D, Jiang T, et al. Scalp EEG functional connection and brain network in infants with West syndrome. Neural Netw. 2022;153:76–86. doi:10.1016/j.neunet.2022.05.029.

[59] Sargolzaei S, Cabrerizo M, Goryawala M, Salah Eddin A, Adjouadi M. Scalp EEG brain functional connectivity networks in pediatric epilepsy. Comput Biol Med. 2015;56:158–166. doi:10.1016/j.compbiomed.2014.10.018.

[60] Chen H, Wang Y, Ji T, Jiang Y, Zhou XH. Brain functional connectivity-based prediction of vagus nerve stimulation efficacy in pediatric pharmacoresistant epilepsy. CNS Neurosci Ther. 2023;29(11):3259–3268. doi:10.1111/cns.14257.

[61] Davis PE, Kapur K, Filip-Dhima R, Trowbridge SK, Little E, Wilson A, et al. Increased electroencephalography connectivity precedes epileptic spasm onset in infants with tuberous sclerosis complex. Epilepsia. 2019;60(8):1721–1732. doi:10.1111/epi.16284.

[62] Lopez KL, Monachino AD, Morales S, Leach SC, Bowers ME, Gabard-Durnam LJ. HAPPILEE: HAPPE in low electrode electroencephalography, a standardized pre-processing software for lower density recordings. NeuroImage. 2022;260:119390. doi:10.1016/j.neuroimage.2022.119390.

[63] Liu L, Zheng R, Wu D, Yuan Y, Lin Y, Wang D, et al. Global and multi-partition local network analysis of scalp EEG in West syndrome before and after treatment. Neural Netw. 2024;179:106540. doi:10.1016/j.neunet.2024.106540.

[64] Hassan M, Merlet I, Mheich A, Kabbara A, Biraben A, Nica A, et al. Identification of interictal epileptic networks from dense-EEG. Brain Topogr. 2017;30(1):60–76. doi:10.1007/s10548-016-0517-z.

[65] Hassan M, Mheich A, Biraben A, Merlet I, Wendling F. Identification of epileptogenic networks from dense EEG: A model-based study. Annu Int Conf IEEE Eng Med Biol Soc. 2015;2015:5610–5613. doi:10.1109/EMBC.2015.7319664.

[66] Chen H, Ji T, Zhan X, Liu X, Yu G, Wang W, et al. An explainable statistical method for seizure prediction using brain functional connectivity from EEG. Comput Intell Neurosci. 2022;2022:2183562. doi:10.1155/2022/2183562.

[67] Ntolkeras G, Makaram N, Bernabei M, De La Vega AC, Bolton J, Madsen JR, et al. Interictal EEG source connectivity to localize the epileptogenic zone in patients with drug-resistant epilepsy: A machine learning approach. Epilepsia. 2024;65(4):944–960. doi:10.1111/epi.17898.

[68] Zhong L, Wan J, Yi F, He S, Wu J, Huang Z, et al. Epileptic prediction using spatiotemporal information combined with optimal features strategy on EEG. Front Neurosci. 2023;17:1174005. doi:10.3389/fnins.2023.1174005.

[69] Wilcoxon F. Individual comparisons by ranking methods. Biometrics Bull. 1945;1(6):80–83.

[70] Benjamini Y, Hochberg Y. Controlling the false discovery rate: A practical and powerful approach to multiple testing. J R Stat Soc Series B Methodol. 1995;57(1):289–300.

[71] Lakens D. Calculating and reporting effect sizes to facilitate cumulative science: A practical primer for t-tests and ANOVAs. Front Psychol. 2013;4:863. doi:10.3389/fpsyg.2013.00863.

[72] Hsieh TY, Hung PL, Su TY, Peng SJ. Graph theory-based electroencephalographic connectivity via phase-locking value and its association with ketogenic diet responsiveness in patients with focal onset seizures. Nutrients. 2022;14(21):4457. doi:10.3390/nu14214457.

[73] Liang Y, Chen C, Li F, Yao D, Xu P, Yu L. Altered functional connectivity after epileptic seizure revealed by scalp EEG. Neural Plast. 2020;2020:8851415. doi:10.1155/2020/8851415.

[74] Rubinov M, Sporns O. Complex network measures of brain connectivity: Uses and interpretations. NeuroImage. 2010;52(3):1059–1069. doi:10.1016/j.neuroimage.2009.10.003.